SOURCE DYNAMICS FROM DEUTERONS AND ANTI-DEUTERONS IN $\sqrt{s_{NN}}$ = 200 GeV Au+Au COLLISIONS

By

Hugo E. Valle

Dissertation

Submitted to the Faculty of the

Graduate School of Vanderbilt University

in partial fulfillment of the requirements

for the degree of

DOCTOR OF PHILOSOPHY

in

PHYSICS

December, 2008

Nashville, Tennessee

Approved:

Professor Julia Velkovska

Professor Charles F. Maguire

Professor Will Johns

Professor Volker Oberacker

Professor Franz Baudenbacher

PHYSICS

ABSTRACT

SOURCE DYNAMICS FROM DEUTERONS AND ANTI-DEUTERONS IN $\sqrt{s_{NN}}$ = 200 GeV Au+Au COLLISIONS

HUGO E. VALLE

Dissertation under the direction of Professor Julia Velkovska

We have studied the source dynamics of the matter in ultrarelativistic $Au+Au$ collisions at $\sqrt{s_{NN}}$ =200 GeV by analyzing the production of the simplest nuclei: deuterons and anti-deuterons. In relativistic heavy ion collision the system expands and cools, and when the interactions among the particles finally cease during the "freeze-out", light nuclei like d and $\bar{d}$ can be formed.

The transverse momentum (p_T) spectra of d and $\bar{d}$ in the range $1.1 < p_T < 5.0$ GeV/c have been measured at mid-rapidity. The slopes of the hadron spectra are directly related to the temperature of the source at freeze-out and the flow velocity of the collectively expanding system. The radial flow has the effect of flattening the spectra of heavier particles, thus the d and $\bar{d}$ spectra are less steeply falling than the (anti-)proton spectra.

Measurements of radial flow velocity and freeze-out temperature using the blast-wave hydrodynamic model for deuterons was attempted. Our results indicate that within this

model the deuterons do not freeze-out contemporaneously with the produced hadrons. The deuteron spectra require a lower flow velocity than the proton spectra. Due to their unique sensitivity to the dynamics of the emission process, these results can constrain full hydrodynamics calculations.

The coalescence probability, B_2, of neutrons and protons into deuterons as a function of transverse momentum and centrality has been studied. We observed a decrease in B_2 for more central collisions where the volume of the system is larger. The ratio of the hadron spectra in central and peripheral collisions (R_{CP}) is used to study the effects of the quark-gluon plasma medium on the propagation of fast partons through it. For deuterons, we observe a significant enhancement in R_{CP} compared to other hadrons. This behavior indicates that both proton and neutron production are enhanced contrary to the suppression of pions.

Approved _____ Date _____

This dissertation is dedicated to
the memory of my grandmother Elvia Elizondo,
and to my parents

. . .

Esta disertación está dedicada
a la memoria de mi abuela Elvia Elizondo,
y a mis padres

ACKNOWLEDGEMENTS

This dissertation would not have been possible without the financial support of the relativistic heavy ion physics group from the Department of Physics and Astronomy at Vanderbilt University. I am indebted to Dr. Julia Velkovska who, as my mentor, advisor, and dissertation director, has been supportive of my career goals and has actively encouraged me to pursue them.

I am thankful for the opportunity of having had her as my dissertation director. Working with Julia has been a rewarding experience and has made me grow as a scientist. Julia has always believed in my ability to do research in this field, and always found time in her busy schedule to help me. Whether stressed, burned out, or lost in the physics we were trying to study, she would always be available for good conversation and to bring me back on track. As a mentor, Julia has showed me the importance of fundamental physics research and has given me the insight to find the simplest approach to complex problem solving. Above all, Julia has been a good friend.

Several other people have also helped me in a significant way during my Ph.D. journey. First, I would like to thank Dr. Charles Maguire and Dr. Victoria Greene. I would not have joined the Vanderbilt team without them. Thank you, Charlie, for making my life easier by always answering my computational and experimental questions simply and straightforwardly. Second, I want to thank the post-docs in the group, Michael Isaah and Shengli Huang, who have taught me a great deal of things related to my research, and with whom I have had many valuable discussions. Finally, I want to say thank you to my lab colleagues, Dillon Roach, Ron Belmont, and Brian Love, for helping me deal with daily tasks and

issues in the lab, and for making life through graduate school much more pleasant.

Away from the lab, Nashville offered lots of good things, especially my friends, who brought personal balance to my professional life. Everyone in the Galaxy and Soccettes soccer teams made a terrific group of friends inside and outside the field. But those who really inspired me were my mates in the Corn Bread Mafia basketball team who, despite not winning a single game in four years, kept playing just for the heck of having fun. I have made a lot of friends in Nashville, but I would like to make a special mention to Mayra Fortes, Sarynna Lopez, Chase Boulware, and Eric Chancellor for being there and for sharing important dates in my life: you all are terrific friends. I want to give special thanks to my roommate Manoj Sridhar, with whom I shared the last two years of my life and, with that, my ups and downs both at the professional and personal levels. For that, "gracias amigo."

I also want to express gratitude to my parents, Baldomero and Leticia; brothers, Baldo and Edgar; and my extended family for their unconditional support. They have always been there for me, and have shared my sacrifices and achievements. I know they are enjoying the end of my student years as much as I am. I thank my grandmother Elvia Elizondo, to whom I dedicate this dissertation. I know she watches me from heaven, and is happy for this moment as well.

Last but not least, I am really thankful to my best friend and wife, Isabel. I thank her for bearing with me all these years of hard research, especially the last few months of writing this dissertation. Graduate school is long and challenging and, without her, it would have not been possible or even worth it. I love you.

AGRADECIMIENTOS

Esta disertación no habría sido posible sin el apoyo financiero del equipo de iones pesados relativísticos del Departamento de Física y Astronomía de Vanderbilt University. Estoy sinceramente agradecido a la Doctora Julia Velkovska quien, en su labor de mentora, consejera y directora de tesis, me ha apoyado en mis objetivos profesionales y me ha animado activamente a realizarlos. Estoy agradecido por la oportunidad de haberla tenido como directora de tesis. Trabajar con Julia ha sido una experiencia gratificante y me ha permitido crecer como científico. Julia siempre me ha apoyado a investigar sobre este campo de la física, y siempre encontraba tiempo en su apretada agenda para ayudarme. En momentos de estrés, de fatiga o de estar totalmente perdido en los análisis, ella siempre estaba disponible para conversar y ponerme otra vez en el camino correcto. Como mentora, Julia me ha mostrado la importancia de la investigación de la físca como disciplina, y me ha enseñado la destreza necesaria para encontrar el acercamiento más simple a la resolución de problemas complejos. Sobre todo, Julia ha sido una buena amiga.

Otras personas también me han ayudado de una manera significativa a lo largo de este viaje. Primero, me gustaría dar las gracias al Doctor Charles Maguire y a la Doctora Victoria Greene. Sin su ayuda no habría sido posible unirme al equipo de Vanderbilt. Gracias, Charlie, por hacer mi vida más fácil al responder mis incontables preguntas de de una manera sencilla y directa. Segundo, quiero dar las gracias a los asistentes postdoctorales del grupo, Michael Isaah y Shengli Huang, quienes me han enseñado infinidad de conceptos relacionados con mi investigación, y con quienes he tenido valiosas conversaciones. Finalmente, quiero dar las gracias a mis colegas del laboratorio, Dillon Roach, Ron Belmont y

Brian Love, por ayudarme con las tediosas labores y los problemas diarios del laboratorio, y por hacer mi vida de estudiante de posgrado mucho más llevadera.

Fuera del laboratorio, Nashville me ha ofrecido un montón de buenas cosas, en especial mi amigos, quienes dieron equilibrio personal a mi vida profesional. Todos los componentes de los equipos de fútbol Galaxy y Soccettes fueron estupendos amigos dentro y fuera del campo de juego. Pero los que realmente me inspiraron fueron los compañeros del equipo de baloncesto Corn Bread Mafia porque, a pesar de no ganar ni un sólo partido en cuatro años, siguieron jugando a todo dar simplemente para pasarla bien. He hecho muchos amigos en Nashville pero me gustaría hacer una mención especial a Mayra Fortes, Sarynna Lopez, Chase Boulware y Eric Chancellor por compartir buenos ratos y por haber estado presente en importantes fechas de mi vida: ustedes son unos amigos fabulosos. Quiero agradecer en especial a mi compañero de apartamento, Manoj Sridhar, con quien he compartido los dos últimos años de mi vida y, con eso, mis bajones y mis alegrías a nivel profesional y personal. Gracias, amigo, por todo.

También quiero expresar gracias a mis padres, Baldomero y Leticia; a mis hermanos, Baldo y Edgar; y a mi familia extendida, por su apoyo incondicional. Siempre han estado ahí para compartir mis sacrificios y mis logros. Sé que se alegran del fin de mis años de estudiante tanto como yo. Doy gracias a mi abuela, Elvia Elizondo, a quien dedico esta disertación. Sé que me ve desde el cielo, y se alegra de este momento también.

Por último, estoy realmente agradecido a mi mejor amiga y esposa, Isabel. Le agradezco por haber aguantado conmigo todos estos años de investigación y trabajo intensos, sobre todo, estos últimos meses. La Escuela de Posgrado es larga y dura y, sin ella, no habría sido posible ni hubiera merecido la pena. Te quiero.

TABLE OF CONTENTS

LIST OF TABLES

LIST OF FIGURES

CHAPTER I

INTRODUCTION

1.1 Relativistic Heavy-Ion Collisions

The goal of the Relativistic Heavy Ion Collider (RHIC) is to create, identify, and study quark gluon plasma (QGP), the state of matter hypothesized to exist when nuclear matter reaches high enough temperatures and/or energy densities [2]. The QGP is a state of nuclear matter in which the degrees of freedom are colored objects called partons (quarks and gluons), instead of the color-neutral hadronic states which can be directly observed. This form of matter, is the quantum chromodynamics [a] (QCD) analogue of the plasma phase of ordinary atomic matter.

According to lattice QCD calculations [3, 4], it is predicted that the phase transition from a hadronic phase to the QGP phase takes place at a temperature of approximately 170 MeV ($\approx 10^{12} K$), known as the critical temperature (T_c). At the transition temperature the corresponding energy density is $\epsilon \approx 1\ GeV/fm^3$, nearly an order of magnitude larger than that of normal nuclear matter. The calculations also indicate that this drastic change in the behavior of the system occurs over a small range in temperature ($\sim$20 MeV). Another prediction from lattice calculations indicates that the phase change includes the restoration of approximate chiral symmetry coming from greatly reduced or vanishing quark constituent masses. Figure 1.1 shows the variation of the energy density normalized to T^4 (ϵ/T^4) as a

[a] The theory of the strong interactions describing the quarks and gluons as the fundamental constituents of the hadrons and the forces between them, which are governed by the exchange of "color".

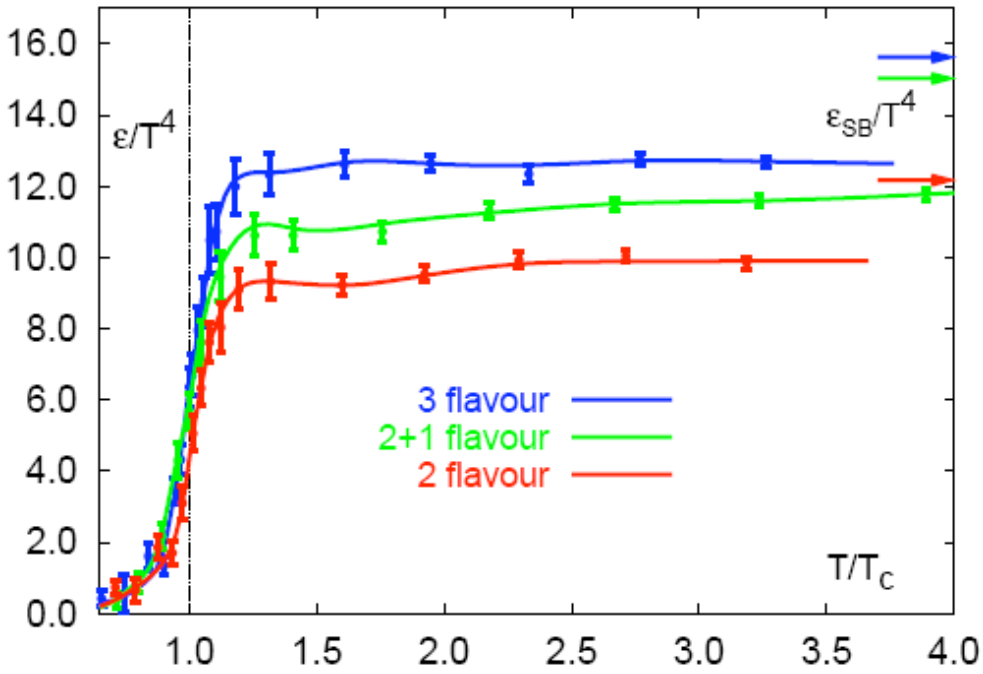

Figure 1.1: Lattice QCD results for the energy density/T^4 as a function of the temperature scaled by the critical temperature T_c. Note the arrows on the right side indicating the values for the Stefan-Boltzmann limit for ideal gas [3, 4].

function of temperature as obtained from lattice QCD. The sharp rise of the energy density at T/T_c = 1.0 for different combinations of light (up and down) and strange quarks indicates a big increase in the effective number of degrees of freedom in the system [b]. In QCD, the interaction between the quarks are described in terms of a running coupling constant, which gets smaller as the distances between the quarks get smaller (asymptotic freedom). We also expect that when the temperature increases and approaches infinity, the interactions between the quarks will become vanishingly small and the system will be described by the Stefan-Boltzmann law for ideal gas. As shown in Figure 1.1, the lattice QCD calculations appears to be really close (20%) to the Stefan-Boltzmann limit calculated for a system of

[b] Stefan-Boltzmann law: energy density is proportional to the number of degrees of freedom times T^4. The higher the value of ϵ/T^4 above T_c indicates new degrees of freedom have been liberated.

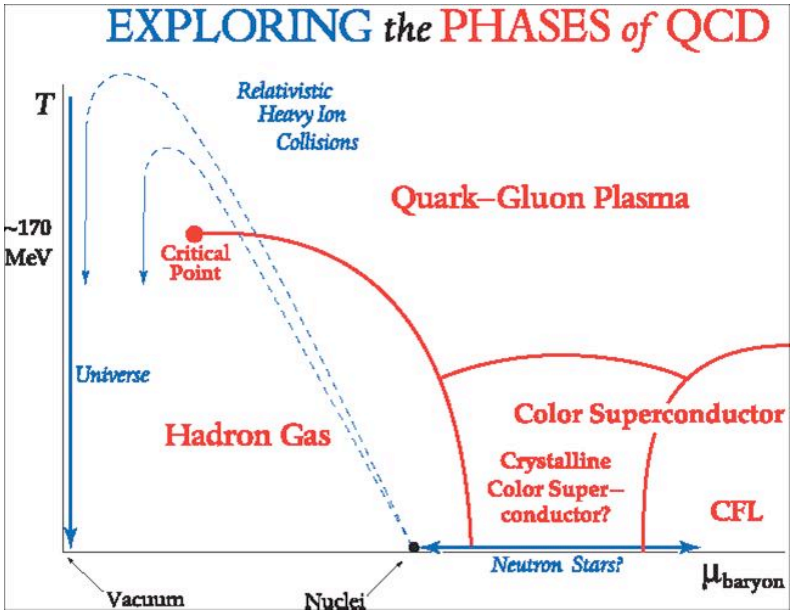

Figure 1.2: Conjectured QCD phase diagram as a function of Temperature T and baryon chemical potential, μ_{baryon}. The early universe is thought to have been filled with quark-gluon plasma (QGP) during the first microseconds after the Big Bang. The QGP is also thought to be created in heavy-ion collisions at RHIC. A first order phase transition may occur for μ_{baryon} above the possible critical point [5, 6].

non-interacting quarks and gluons. From this information, we can indirectly argue that indeed the degrees of freedom in this new phase are quarks and gluons. From Figure 1.1 all we can also conclude that at infinite temperature the system is not quite ideal gas and there are still significant interactions between its constituents.

A schematic version of a phase diagram for idealized nuclear matter with two massless quarks and one infinitely heavy quark is shown in Figure 1.2 [5, 6]. In Figure 1.2, the red line between the hadron gas and QGP phases corresponds to the first order phase transition. This transition ends at a critical point at which there is a second order transition. It is also observed that at low μ_b, the transition is a cross over between the two phases, meaning that there is no latent heat involved as in a first order transition, or there are no large fluctuations and discontinuities in the thermodynamical quantities as in a second order phase transition.

Continuing on the red line and after the second order phase transition point is reached, a smooth change is observed as the line approaches zero chemical potential. Theoretical arguments and experimental data [7] suggest that nucleus-nucleus collisions at RHIC are characterized by low net baryon density, depicted in the left half of the phase diagram. In this region, and at low temperatures, strongly interacting mater is thought to exist as a hadron gas.

1.1.1 Collision Dynamics

Static properties of QGP are evaluated and predicted by lattice QCD. However the dynamical properties of QGP are still less known because the lattice gauge theory does not permit a direct calculation of quantities related to the "real-time" evolution.

A phenomenological picture of a heavy-ion collision is presented in Figure 1.3. After an impact of the incoming nuclei, the kinetic energy of both nuclei is partially dissipated in the overlapping region of colliding nuclei. The system heats up and subsequently undergoes in a phase transition from normal nuclear matter to QGP. The QGP is a deconfined state in a chemical and thermal equilibrium, which lasts over a brief time ($\tau \sim 10$ fm/c). Then, QGP evolves, expanding and cooling hydrodynamically until it reaches the critical temperature. At this point, the system hadronizes into a gas of hadrons. The hadrons could interact inelasticaly (*i.e.* change identities) and establish chemical equilibrium. Since the system expands, at some point the inelastic collisions cease. The final hadron abundancies reflect the time at which the system freezes out chemically. Next, there can still be elastic interactions between the hadrons, where the momentum spectra of the hadrons, but not the

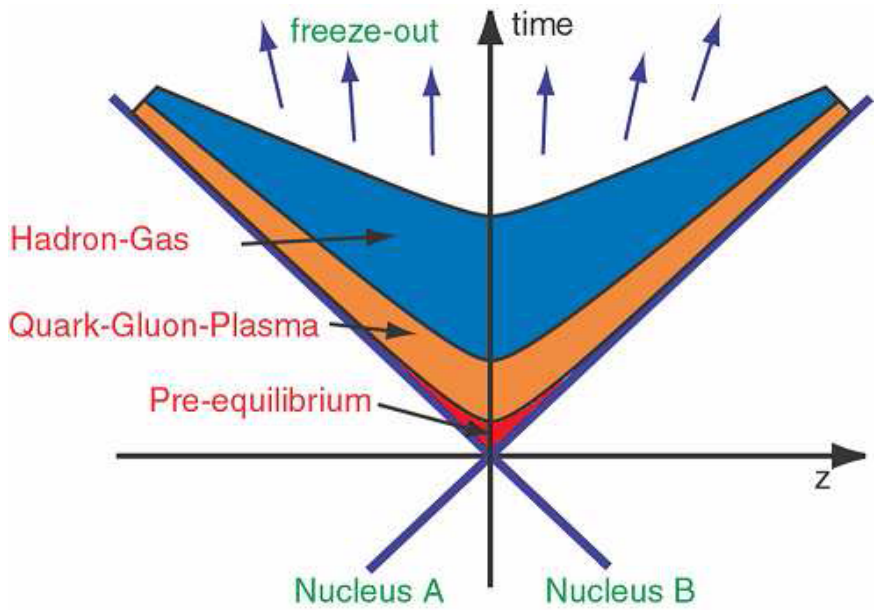

Figure 1.3: Space-time picture of a nucleus-nucleus collision.

particle type can still change. The so called kinetic freeze-out marks the end of elastic interactions between particles, at which point the system is too dilute for hadrons to interact with each other and therefore we can detect them. Since produced hadrons carry information about the collisions dynamics and the entire space-time evolution of the system from the initial to the final stage of collisions, a precise measurement of the transverse momentum (p_T) distribution and yields of identified hadrons as a function of collision geometry are essential for the understanding of the collision dynamics and properties of the created matter.

1.2 Probes of Quark-Gluon Plasma

In order to infer the information of a QGP, a variety of probes have been proposed. When a QGP is produced in a heavy-ion collision, it subsequently hadronizes. Since the QGP cannot be directly measured, the only way to study it is to measure the physical ob-

servables or signatures of the produced particles. These signatures include the observables of simple particle number N, the transverse energy E_T [8], the observation of hydrodynamic flow within the constraints of models which we include a phase transition to QGP (*e.g.* [9]), or observations of hadronic freeze-out in "chemical" equilibrium consistent with a thermalized system freezing out at the critical temperature [10].

1.2.1 Hard Probes

Perhaps the most sensitive types of probes of the QGP medium properties are so-called penetrating probes. Particles created from QCD hard-scattering are produced at the very early stage of the collision [c]. Since they are produced in the initial interaction, hard probes propagate through, and can be modified by the medium. High p_T particles from jets and particles containing heavy quarks (*i.g.* J/Ψ) from hard scattering are called hard probes.

The suppression of high p_T hadrons compared to $p+p$ collisions due to the energy loss of a fast parton (quark or gluon) is a sensitive way of probing the formed QCD medium. The mechanism is similar to that responsible for the electromagnetic energy loss of a fast charged particle traveling through matter, *i.e.* energy may be lost either by excitation of the penetrated medium or by radiation. The fast parton may produce the high-p_T hadron, so the measurement of high-p_T hadron production is a good probe for studying the parton energy loss [11–13]. At RHIC, measurements of high transverse momentum hadrons such as π^0 and inclusive charged hadrons, have found that their particle yields in central $Au+Au$ collisions is suppressed by a factor of $\approx$5 relative to the production in proton-proton ($p+p$).

[c] Hard scattering is a process that proceeds with large momentum transfer between the partons. The cross-section for such processes can be computed using perturbative QCD, since the coupling constant is small in these cases

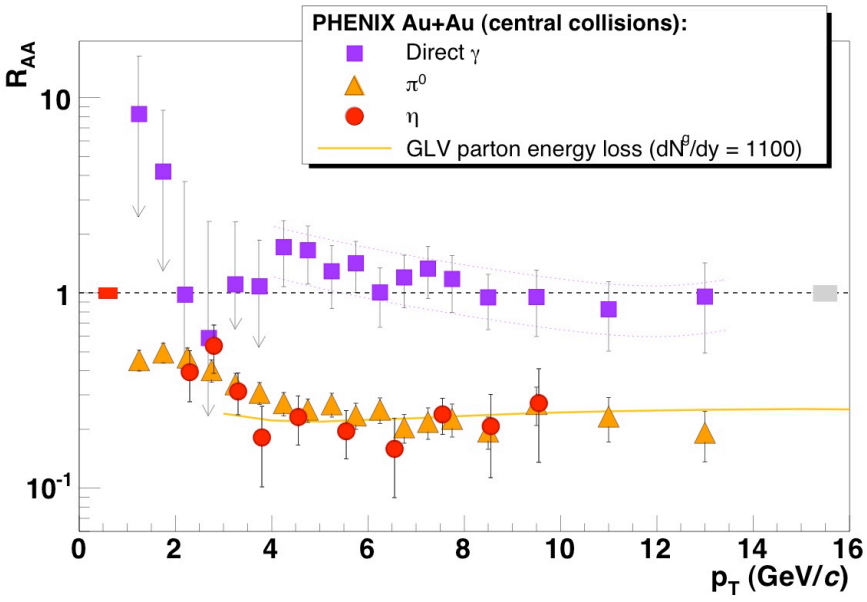

Figure 1.4: Nuclear modification factor (R_{AA}) as a function of p_T for photons (γ), π^0, and η mesons in central $Au + Au$ collision at $\sqrt{s_{NN}}$= 200 GeV [14].

To quantify the effect of the QCD medium, we define a nuclear modification factor, R_{AA}, which is the ratio of the cross section per nucleon-nucleon collisions measured in a heavy-ion collision divided by the cross section measured in $p + p$ collisions. Figure 1.4 shows the nuclear modification factor (R_{AA}) as a function of p_T for photons (γ), π^0, and η mesons in central $Au + Au$ collision at $\sqrt{s_{NN}}$= 200 GeV [14]. If there were no nuclear effect it would be unity. Note the strong suppression of the mesons and the lack of suppression for the photons, which do not interact with the final state medium. This suppression is described as "jet quenching", which is the parton energy loss via gluon radiation. The jet quenching is considered an important probe for the early stage of heavy-ion collisions where very hot, dense partonic matter (QGP) could exist. As stated before, Figure 1.4 shows that direct γ are not suppressed as expected because photons do not interact with the medium.

Over the past years, a lot of work has been devoted to study the propagation of jets thorough QCD matter both experimentally and theoretically. More support for jet-quenching comes from measurements of angular correlations between high-p_T particles on an event-by-event basis. Since the jets originate from partons emitted back-to-back, it is expected that the final state hadrons will be correlated. In the presence of the nuclear medium, these correlations may be modified. Experiments at RHIC show that indeed such modifications are present in the data from $Au + Au$ collisions but not in $p + p$ or $d + Au$ collisions [15]. The $d + Au$ collisions provide an important control experiment since the nuclear matter does not heat up high enough temperature to produce the QCD, but nuclear effects are still present in the initial state. Hence, the observed absence of high-p_T suppression in $d + Au$ tells us that initial state effects are small, so the suppression observed in $Au + Au$ collisions is most likely due to parton energy loss in the hot medium [16].

Suppression of heavy quarkonia has been proposed as a signature of deconfinement. The suppression mechanism follows directly from the Debye screening expected in the medium, which reduces the range of the potential between charm quark and anti-quark pairs [17, 18]. If the radius of a meson is larger than the Debye radius, which is determined by the plasma temperature and density, the meson cannot survive in the plasma. It is proposed that the J/Ψ meson made of $c\bar{c}$ quarks is suitable for the detection of Debye screening effects for the following reasons. First, if the J/Ψ particles decay leptonically, the leptons will not interact strongly with other hadrons and will be detected without being altered by the subsequent evolution of the medium. Secondly, J/Ψ's are produced in the very early stage of the collision. Finally, the hadronic interaction cross-section of J/Ψ is relatively small ($\sigma_{\Psi N} \sim 6mb$), therefore it carries information of the initial state conditions

of the collisions.

1.2.2 Soft Physics

The collective motion of produced hadrons in the final state is expected to provide information on the dynamics of heavy ion collisions. A hydrodynamical description of the collective motion or elliptic flow of the collisions, invokes pressure gradients which drive the compressed matter at the early stage of the collision. In the case of a phase transition from ordinary nuclear matter to the QGP, it is expected that the equation of state should exhibit a corresponding softening due to the increased number of degrees of freedom [19]. For this reason, the observation of collective motion is crucial to validate the hydrodynamical description of the evolution of heavy ion collisions.

A schematic view of a semi-central heavy ion collision in the transverse plane is given in Figure 1.5 (a). One notices an approximately elliptical overlap region, where the short axis of the ellipse is aligned with the azimuth of the reaction plane of the collision (Ψ_{RP}). If the matter is thermalized, pressure gradients can develop that predominantly drive particle emission along the reaction plane (cf. Figure 1.5 (b)), thereby transforming the initial spatial anisotropy (Figure 1.5 (a)) into an effective momentum anisotropy (Figure 1.5 (c)) [20].

This phenomenon, commonly referred to as "elliptic flow", is sensitive to the early stages of a heavy ion collision and can give valuable information pertaining to issues of thermalization, pressure estimates and possibly the equation of state (EOS) [20]. The azimuthal distribution of particles with respect to the reaction plane, can be described via a Fourier decomposition. For symmetry reasons, the odd Fourier coefficients vanish if taken

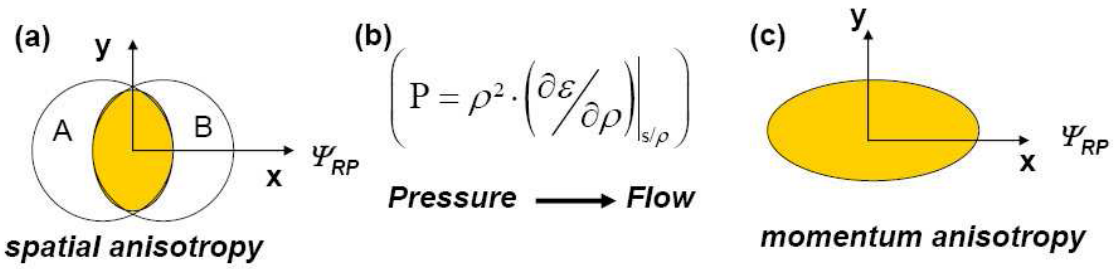

Figure 1.5: Schematic illustration of elliptic flow (see text).

in a symmetric window around midrapidity, and elliptic flow can be identified with the second harmonic Fourier coefficient of this distribution [21], generally know as v_2 (see Equation 1.1).

$$\frac{dN}{d(\phi - \Psi_R)} \propto 1 + 2v_2 \cos 2\phi - \Psi_R \tag{1.1}$$

At RHIC, large azimuthal anisotropy (v_2) has been observed. If v_2 from $\sqrt{s_{NN}}$= 200 GeV is compared to values with lower energies, we find the v_2 to be larger, which suggest that thermalization is taking place much faster than expected from normal hadronic rescattering. Thus the large v_2 implies other ingredients (*i.e.* quarks and gluons) for thermalization than just hadrons, for example large v_2 (as large as 10%) values were observed for decay electrons from D and B mesons. As shown in Figure 1.6 , the p_T dependence of v_2 provides important clues to understand the particle production. The upper panels from Figure 1.6 show the v_2 parameter plotted vs hadron transverse momentum p_T (top left), or hadron transverse kinetic energy $KE_T = \sqrt{p_T^2 + m^2} - m$ (top right). It is observed that at low KE_T there is a mass ordering characteristic of the hydrodynamics behavior of particles flowing with common velocity: the higher mass particles are pushed to higher

transverse momentum. When plotted versus transverse kinetic energy, the elliptic flow for all hadrons follows a uniform trend indicating a common hydrodynamic origin of the elliptic flow. At higher kinetic energy the data show a distinct difference between mesons and baryons. The lower panels of Figure 1.6 show the elliptic flow per valance quark (v_2/n_q) vs transverse momentum per valance quark (p_T/n_q) (bottom left) and the transverse energy per valance quark (KE_T/n_q). The collapse of all data into a single curve in the lower right panel indicates that the collective flow originates as a hydrodynamical phenomenon at the valence quark level [22]. This empirical scaling result also indicates that hadron production at intermediate p_T is likely dominated by the coalescence of quarks in the dense medium instead of fragmentation of hard-scattered partons. This important finding helps resolve unexpected features of baryon production and its modification in the nuclear medium.

The Hanbury-Brown-Twiss effect (HBT), first used to measured the diameter of a star [23], is also used in high energy nuclear experiments to measure the space-time (or energy-momentum) correlation of identical particles emitted from an extended source. In ultrarelativistic heavy-ion collisions, HBT measurements can yield information about the size and the matter distribution of the source. The formation of a QGP will lead to an extended source and long lifetimes.

1.3 Nuclear Clusters as Probes of Final State Effects

Deuterons and anti-deuterons are the simplest composite objects and are useful in establishing expansion and correlations on the emitting source. Volume-expansion due to secondary interactions tends to diminish the cluster yields as particle production rises both

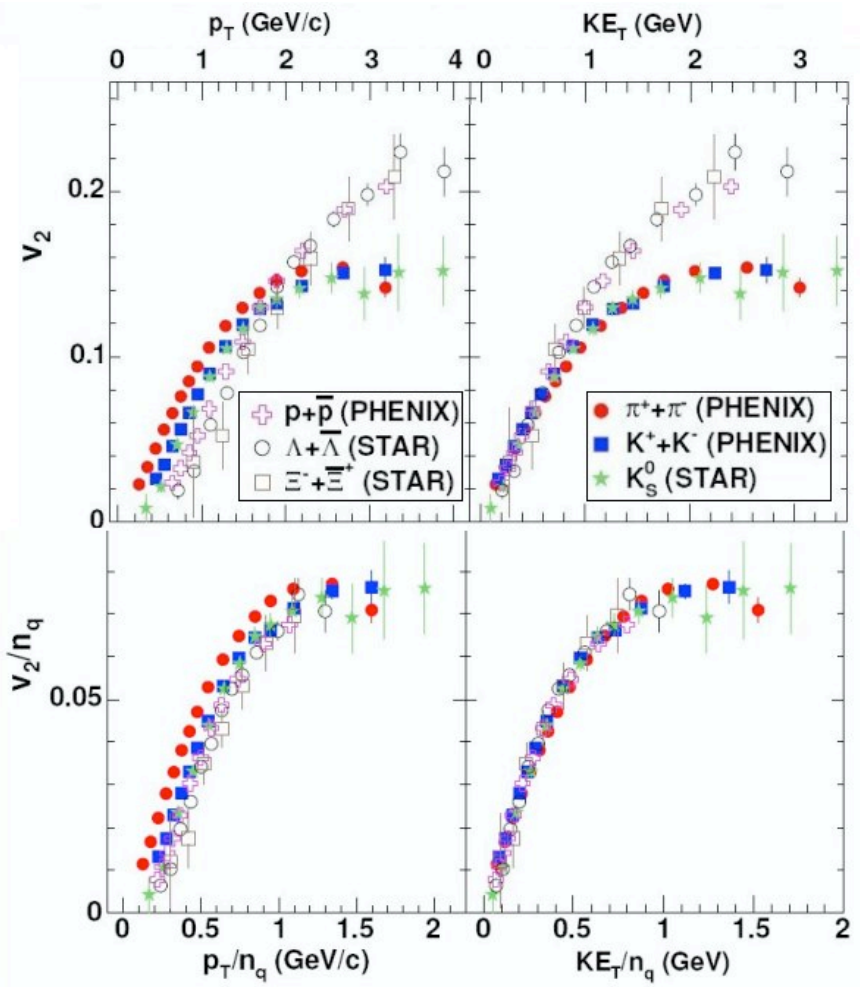

Figure 1.6: Upper panels: The elliptic flow parameter v_2 plotted versus hadron transverse momentum p_T (left) or hadron transverse energy $E_T = \sqrt{p_T^2 + m^2}$ (right). Lower panels: Elliptic flow per valence quark (v_2/n_q) vs transverse momentum per valence quark (p_T/n_q) (left) or transverse energy per valence quark E_T/n_q [22].

with the beam energy and the system size [24].

By studying the production of deuterons and anti-deuterons, we can explore the final state effects of the produced matter from $Au + Au$ collisions at $\sqrt{s_{NN}}$ = 200 GeV. In relativistic heavy ion collisions the systems expands and cools, and when the interaction among the particles finally ceases during the "freeze-out" stage, light nuclei like deuterons and anti-deuterons (d and $\bar{d}$) can be formed. The probability of forming a deuteron is proportional to the product of the phase space density of their constituent nucleons [25, 26]. Due to their small binding energy it is improbable for deuterons to survive repeated collisions inside the fireball.

The work in this thesis focuses on the following aspects of d and $\bar{d}$ including the centrality dependence of spectra, particle ratios of anti-particle to particles ($\bar{d}/d$), the nuclear modification factor (R_{cp}), average transverse momentum $\langle p_T \rangle$, and the coalescence parameter results for the deuteron. Most of these measurements have been done by the PHENIX collaboration for pions, kaons, protons, and anti-protons. We are interested to observe the behavior of deuterons compared to the other hadrons for the signatures mentioned above.

1.3.1 Mean Transverse Momentum, Particle Yields, and Ratios

Hadron yields and ratios carry information about the chemical properties of the system. Measurements from p_T distributions for pions, kaons, protons, and anti-protons both for central and peripheral collisions have been measured [1]. The measured hadron ratios are consistent with production from a thermal source. The measurements of deuteron production is important, since it indirectly carries information about the neutron production and

the baryon transport in heavy ion collisions. In particular, the $\bar{d}/d$, and corresponding $\bar{n}/n$ ratio give information about the baryon chemical potential in the system and help us locate it on the nuclear phase diagram.

The hadron spectral shapes depend on the temperature of the system as well as its dynamical evolution. They have been compared to a Boltzmann distribution modified to account for collective effects, such as collective expansion with a common flow velocity. The results of these studies show the pion spectra having a concave shape at low p_T, where it is believed that most of the pions may come from the decay of resonances: Δ, ρ, etc. The kaons spectra show more or less an exponential distribution over the entire measured p_T.

A striking observation is that the yields of protons and anti-protons are comparable to those of pions above of 2 GeV/c. In order to quantify the changes in the spectra shapes as a function of centrality, we measure the mean transverse momentum of the deuteron and anti-deuteron spectra. Such measurements have been previously performed for π, K, and p. An increase in the $\langle p_T \rangle$ indicates higher temperature and/or higher flow velocity for the produced hadrons [1]. The $\langle p_T \rangle$ for each measured particle increases as we increase the centrality bin which is consistent with increasing flow velocity. If we compare the $\langle p_T \rangle$ for all particles, the protons and anti-protons show the biggest increase. This is consistent with a collective expansion velocity that increases with centrality to produce the largest increase in $\langle p_T \rangle$ for the heavies particles.

1.3.2 Radial Flow: Comparison to Models

Identified hadron spectroscopy is an important tool for studying the collision dynamics. The momentum spectra of hadrons are sensitive to the dynamical evolution of the system and carry information about the radial flow velocity and thermal freeze-out conditions. Hadron spectra measured at RHIC [1] have been successfully compared to full hydrodynamics calculations. Such comparison are outside the scope of this work. However, a comparison to hydrodynamics-inspired models [27] is often performed. In these models, the spectra are fitted to a Boltzmann distribution with a "blue-shift" due to the collective flow. The radial flow velocity, β_T, and freeze-out temperature, T_{fo}, are extracted by "blast-wave" fit to the p_T spectra. The study of deuteron spectra adds significant new information because: 1) the deuterons are much heavier than the protons and will thus multiply possible mass effects in the hadron spectra, 2) the deuterons are composite particles formed at the freeze-out stage and thus their spectra are sensitive to the dynamics and duration of the hadron gas stage.

1.3.3 B2 Parameter, Volume, Radii

The observed deuterons are believed to be created by the coalescence of protons and neutrons at freeze-out. Using this model, the neutron and the proton interact via the strong force coupled to a third body which allows them to bind and form the deuteron. Measuring the d and $\bar{d}$ yields will provide information about the space-time evolution of the system and the source size at freeze-out. The invariant d and $\bar{d}$ yields can be related [28] to the

primordial nucleon yields as:

$$E_d \frac{d^3 N_d}{dp_d^3}\bigg|_{p_d=2p_p} = B_2 \left[E_p \frac{d^3 N_p}{dp_p^3} \right]^2 \tag{1.2}$$

where B_2 is the two-nucleon coalescence parameter. The above equation includes an implicit assumption that the ratio of neutrons to protons is unity. The invariant yield of p and $\bar{p}$ [1, 29] in conjunction with the d and $\bar{d}$ yields are used to extract the coalescence parameter. Physically, the coalesce parameter is the measure of the source size: $B_2 \propto 1/V$.

1.3.4 Nuclear Modification Factors

Nuclear modification factors, R_{AA} and R_{CP}, which are quantitative measures of medium affects on particle production, are used to study parton energy loss in QGP. R_{AA} is the ratio of yields in heavy ion collision to the yields in proton on proton ($p + p$) collisions, normalized to the number of binary collisions. R_{CP} is the ratio of yields in central heavy ion collision to the yields in peripheral heavy ion collisions, scaled by the ratio of the respective number of binary collisions. These quantities are defined as follows:

$$R_{AA} = \frac{Yield^{central}}{N_{coll}^{central} Yield^{pp}}, \tag{1.3}$$

$$R_{CP} = \frac{Yield^{central}}{Yield^{peripheral}} \frac{N_{coll}^{peripheral}}{N_{coll}^{central}}. \tag{1.4}$$

From the above ratio measurements, it has been observed that baryons show a different behavior from that of mesons, where the mesons exhibit a suppression effect at interme-

diate p_T while baryons do not [30]. The proton and anti-proton spectra exhibit a notable deviation from a Boltzmann distribution with a characteristic flattening at low transverse momentum which is attributed to strong radial flow in the expanding source. This effect is not so prominent for the lighter particles. The collective effects gradually set in as the collision between the incoming nuclei become more central. Deuterons are formed by the coalescence of two baryons which can provide information about this process both at the partonic and hadronic stage. It is expected that, as a baryon, the neutron should have a similar R_{CP} to that of the proton, but of course this needs to be verified.

1.4 Thesis Outline

The work presented in this dissertation describes the measurements of deuterons and anti-deuterons transverse momentum spectra. This dissertation is organized as follows. Chapter I provides a general discussion to establish the motivation for this analysis. Chapter II presents the RHIC facility and the experimental setup. In chapter III, the data selection and cut conditions used in the analysis as well as the extraction of raw yields are described. Also, this chapter describes the determination of Monte Carlo (MC) corrections factors and our systematic error studies on the spectra. The results and discussion of the analysis are shown in chapter IV. The final chapter (Chapter V), presents the conclusions of the analysis and the prospects for future results. Appendices provide details that do not cleanly fall into any of the aforementioned chapters. To make this document accessible to non-experts, a brief description of some of the commonly used terms is provided in Appendix D.

CHAPTER II

EXPERIMENT

2.1 The Relativistic Heavy Ion Collider (RHIC)

The Relativistic Heavy Ion Collider (RHIC) is a circular track consisting of super conducting steering magnets placed in a tunnel with a circumference of 3.8 km. The shape of the ring is approximately circular, except for the six regions around intersection points, where magnets steer the two beams' trajectories into straight lines in order to have them collide head-on.

RHIC is a versatile accelerator capable of accelerating a wide variety of nuclei/ions and protons over a wide range of energies. The normal running mode center-of-mass energy for protons is in the range of 200 to 500 GeV. Heavy ions (e.g. Au or Cu ions) have been accelerated to achieve $\sqrt{s_{NN}}$ energies of 19.6, 22.2, 56, 62.4, 130, and 200 GeV per nucleon. Deuteron on gold ($d + Au$) collisions at $\sqrt{s_{NN}}$ = 200 GeV were run during 2003 and 2008 as a comparison experiment to the $Au + Au$ collisions. Another unique capability of RHIC is its ability to run polarized beams of protons for the study of nucleon spin structure. However, the main goal of the collider is still the search for the QGP. Additional information about RHIC can be found elsewhere [31, 32].

RHIC can not start accelerating particles from rest, instead, RHIC is injected with a beam of lower energy, but already accelerated particles from the alternating gradient synchrotron (AGS). Some brief information regarding this accelerator is described in Fig-

ure 2.1. The very beginning of the acceleration process depends on what kind of particle is being accelerated, whether it is a proton or a nucleus.

For heavy ions running at RHIC, the process is as follows: Starting with Au atoms with one extra electron (-1 charge) which originated in the pulsed sputter ion source. The Tandem Van de Graaff accelerates these atoms to 15 MeV (total) by a static electric field into a foil which causes a random number of electrons to be stripped from some of the ions. Again, these positively charged ions are subjected to a static potential and consequently ions with different numbers of electrons left can be differentiated by their curvature in a magnetic field. At this point, Au^{+12} is filtered and further accelerated to 1.0 MeV per nucleon. One more stripping occurs with foil bringing the ions to the Au^{+32} state. These ions then enter the AGS Booster which then accelerates them to 95 MeV, after which they are stripped again until there are only the two highest shell electrons remaining as Au^{+77}. Here, the Au ion is still in this ionic state, and it is not until just before entry into the ATR Transfer line (see Figure 2.1), at an energy of 9.8-10.8 GeV, that the final 2 electrons are stripped. This defines minimum $Au + Au$ energy of RHIC 9.8-10.8 GeV in each ring, resulting in 22 GeV $\sqrt{s}$ collision energy.

The beam exiting the ATR fills the two RHIC beam lines, the beam is then accelerated to full energy. Since the RHIC magnets are superconducting, they must be cooled to a stable operating temperature of 4.6 K. The magnets are used to steer the beams around the rings that are brought to collisions at the interaction points. Collisions can be obtained at the six intersection points in the ring, but only 4 of those are occupied by detectors. The beams are then steered to maximize experimental collision rates, and stored for several hours while the experiment collects data.

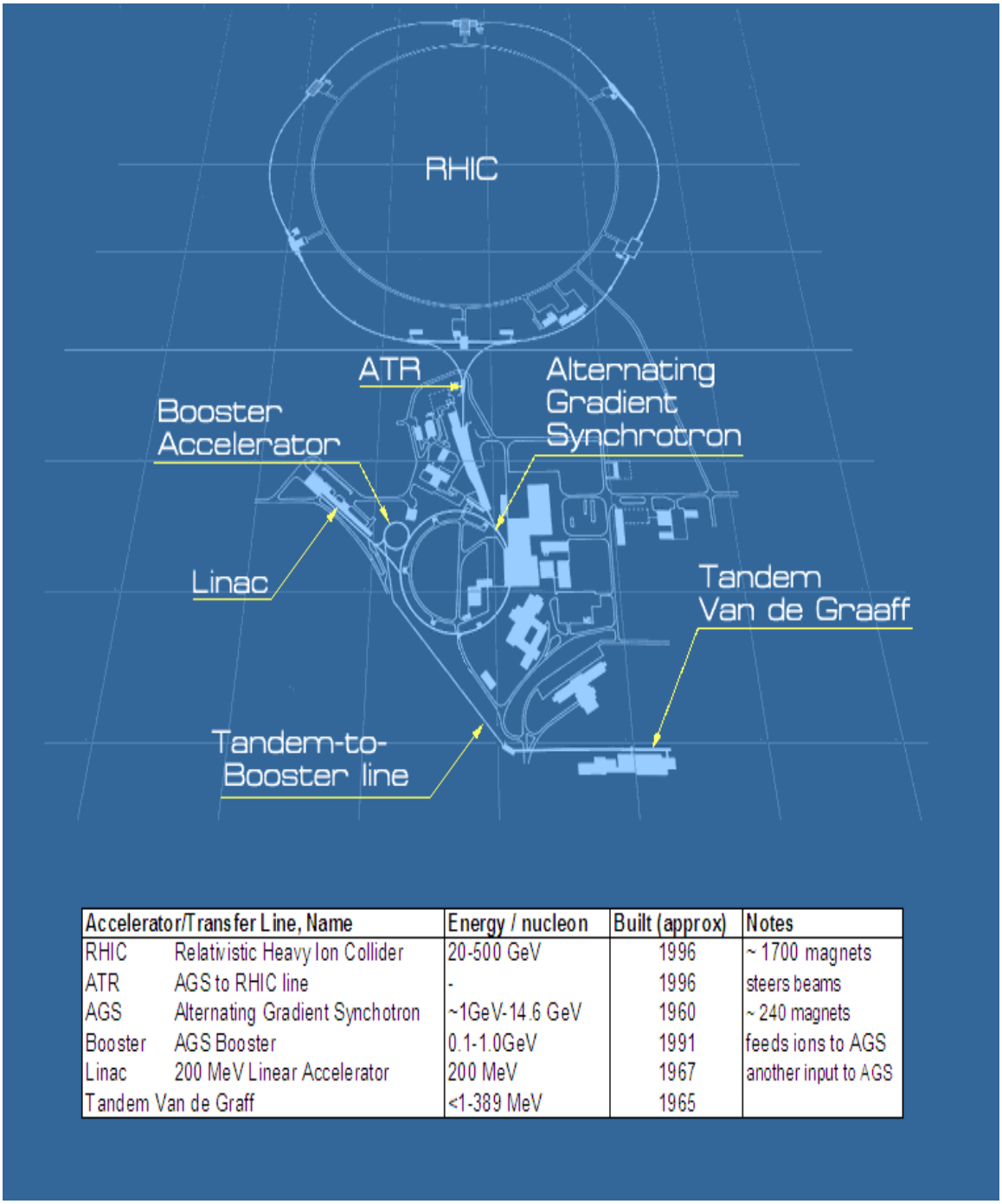

Accelerator/Transfer Line, Name		Energy / nucleon	Built (approx)	Notes
RHIC	Relativistic Heavy Ion Collider	20-500 GeV	1996	~ 1700 magnets
ATR	AGS to RHIC line	-	1996	steers beams
AGS	Alternating Gradient Synchotron	~1GeV-14.6 GeV	1960	~ 240 magnets
Booster	AGS Booster	0.1-1.0GeV	1991	feeds ions to AGS
Linac	200 MeV Linear Accelerator	200 MeV	1967	another input to AGS
Tandem Van de Graff		<1-389 MeV	1965	

Figure 2.1: RHIC is fed by a train of several accelerators.

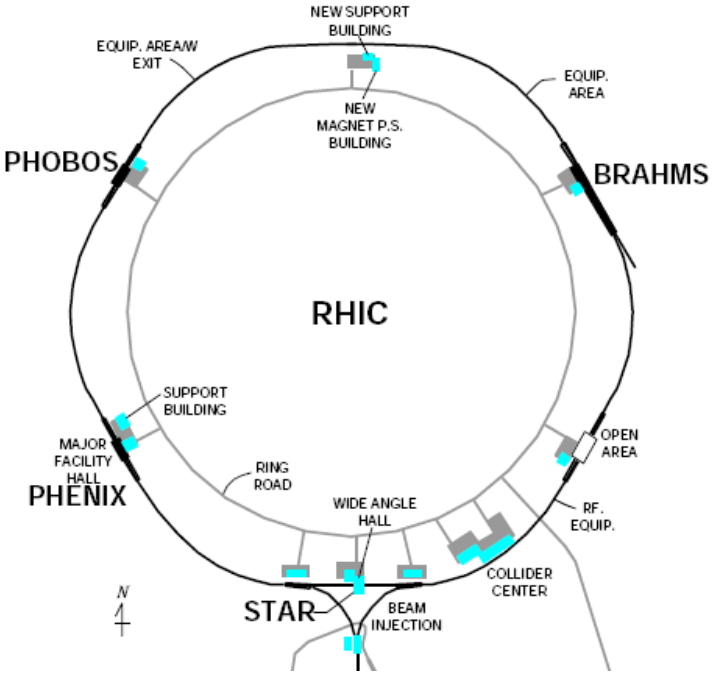

Figure 2.2: Location of the four RHIC experiments along the collider ring.

2.1.1 The Four RHIC Experiments

Experiments are installed at four of the six interaction points inside the accelerator. Two small scale experiments, PHOBOS and BRAHMS (both of them out of commission after the physics Run of 2005), and two large scale experiments, PHENIX and STAR. Their locations on the ring are shown in Figure 2.2

The STAR experiment is based upon a large cylindrical Time-Projection Chamber (TPC), placed inside a solenoidal magnet. The TPC provides tracking and particle identification capabilities covering the full solid angle near mid-rapidity, and it is surrounded by an electromagnetic calorimeter (EMC), which measures transverse energy.

The PHENIX detector consists of a Central Spectrometer and two forward Muon Arms. The Central Spectrometer is equipped with an axial field magnet, and two detector arms

with tracking and particle identification capabilities supplied by layers of several types of detectors. Since this thesis work is based on this experiment, the next sections of this chapter describe the detector subsystems in detail.

The BRAHMS experiment consists of a two-arm magnetic spectrometer, with both arms being movable in order to cover a wide range of kinematic regions with good precision. One of the spectrometers sits in the mid-rapidity region, the other covers the forward angles. The arms are composed of a series of dipole magnets alternating with tracking detectors. Time-of-Flight and $\check{C}$erenkov detectors are also used for particle identification.

The PHOBOS detector main components are a multiplicity array, with an octagonal barrel surrounding the interaction point, and ring detectors in the forward region, vertex detectors, a two-arm magnetic spectrometer, time-of-flight walls, and a set of plastic scintillator trigger counters. Further away from the interaction point are the Zero-Degree Colorimeters common to all the RHIC experiments.

2.2 The PHENIX Detector

The name "PHENIX" stands for Pioneering High Energy Nuclear Interaction eXperiment [33]. The PHENIX layout is shown in Figure 2.3.

It consist of a combination of detectors based on many different technologies to provide a diverse set of measurements. The detector has a built-in redundancy which allows for failure-free operations as well as multiple quality cross-checks. PHENIX is currently made up of 14 subsystems, but new detectors are already scheduled for installation in the upcoming years.

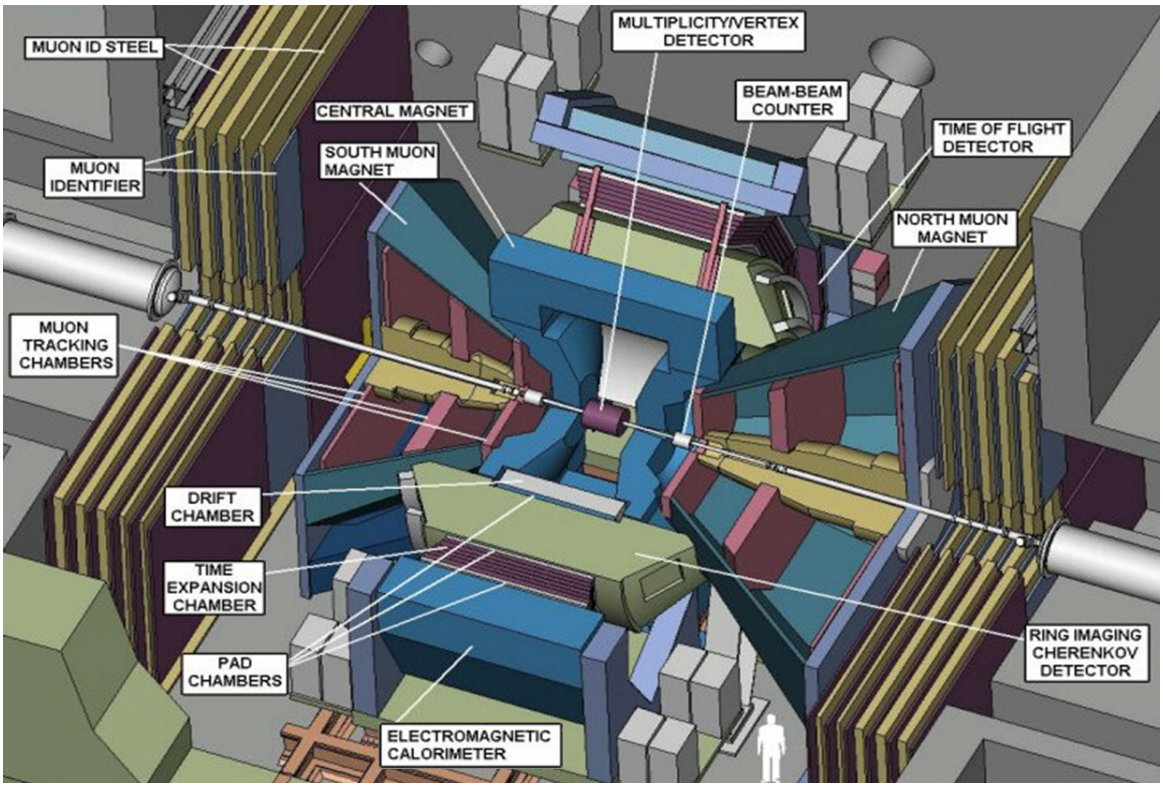

Figure 2.3: A cutaway drawing of the PHENIX detector. Labeled arrows point to the major detector subsystems.

PHENIX's skeleton is approximately 2000 tons of steel magnets which define the three major divisions of the detector: the central arm, the two forward/backward muon arms, and the two global detectors: beam-beam counters (BBC) and zero-degree calorimeters (ZDC). The east and west arms, which form the central arms, are placed around the zero rapidity region and instrumented to detect electrons, photons, and charged hadrons. The north and south forward arms (muon arms) have full azimuthal coverage and are instrumented to detect muons. The global detectors measure the events start time, vertex position and the centrality of the interactions. The rapidity and ϕ coverage and other features of these subsystems are given in Figure 2.3 and a perspective drawing of the PHENIX detector with the major subsystems labeled is shown in Figure 2.4. The data analyzed for this thesis was recorded in 2007, during the Run 7 at RHIC. By this time, the PHENIX detector was a fully mature experiment well described in existing literature [33–41]. So, instead of attempting a fully comprehensive description of the PHENIX detector systems, the following sections will discuss the important details of the subsystems relevant to this analysis, and the final section will just outline the rest of the subsystems.

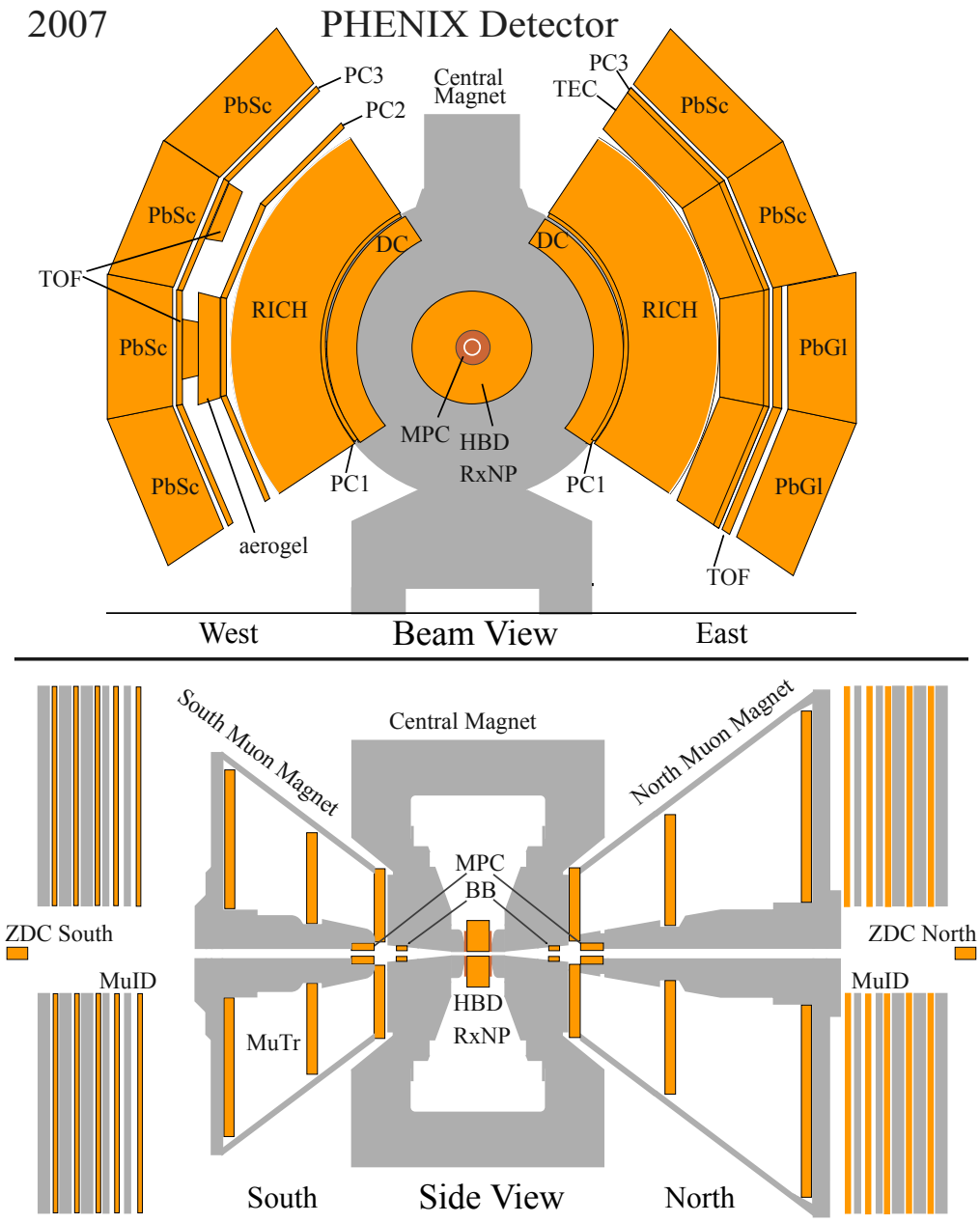

Figure 2.4: Schematic of the PHENIX experiment setup in the 2007 $Au + Au$ run (Run7). Top: Cross section of central arms perpendicular to the beam pipe. Bottom: View from the side with the beam pipe spanning the horizontal direction.

2.3 PHENIX Magnet System

The PHENIX magnet system [38] is composed of three spectrometer magnets with iron yokes and water-cooled copper coils. The Central Magnet (CM) is energized by two pairs of concentric coils, which create field lines which go parallel to the beam in an azimuthally symmetric fashion with respect to the beam axis as shown in Figure 2.5. The magnetic field created here bends charged particles coming from the event vertex in the circumferential ($\overrightarrow{\phi}$) direction, such that after tracking, their momentum can be determined from how much their trajectories are bent. This will be discussed below in the central arm spectrometer section. In the immediate region of the beam, up to a distance of about 1 m, the field is quite uniform and reaches a value of $\sim$ 5000 Gaussian. This field imparts an $\int Bdl$ of about 0.8 Tm. [a] The typical p_T threshold for a charged track by the time it is in the middle of the PHENIX Drift Chamber ($\sim$ 2.2 m) is 86 MeV/c = 0.236 Tm. At a distance of about 2.4 m from the beam, the magnetic field is at its weakest level, with a field integral after that of $\leq$ 0.01 Tm.

Figure 2.4 and Figure 2.5 show how the particle beams go right through the center of the two central field magnet coils, which makes their intersection exactly in the center of the volume between the coils. The origin is defined by this interaction point, and a corresponding choice of axes starts with a z-axis along the beam (the north direction is chosen to be positive z), and y is chosen to point up, away from the ground. The interaction region between the central magnet poles is therefore exactly centered around mid-rapidity and extends to a pseudo-rapidity of +/- 0.35, which also defines the rapidity acceptance of all the detectors in the central arm. The north and south Muon Magnets (MMN and MMS)

[a] 1Tm = 300 MeV/c

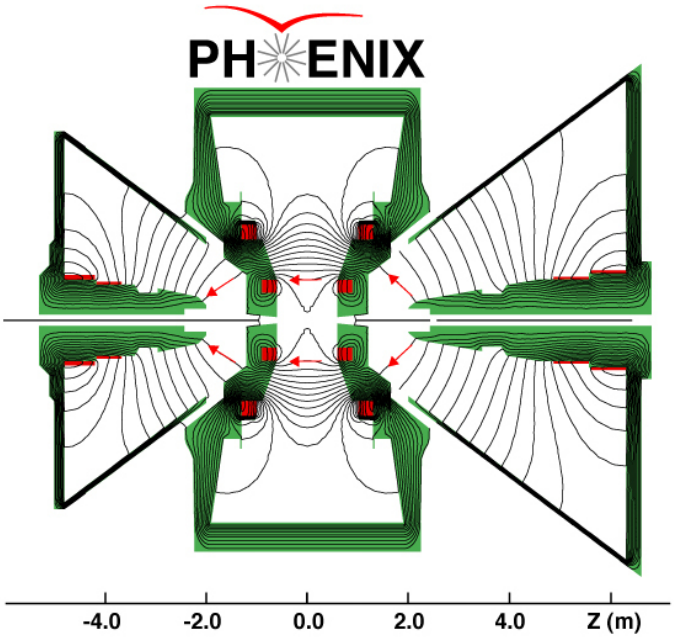

Figure 2.5: PHENIX magnetic field (side view).

use solenoid coils to produce a radial magnetic field for muon analysis. Each covers a pseudo-rapidity interval of 1.1 to 2.3 and full azimuth.

2.4 Global Detectors

The two relatively small global detectors consist of: the Beam Beam Counter (BBC) and the Zero Degree Colorimeter (ZDC). These two detectors are probably the most important detectors on PHENIX. These subsystems perform three essential functions: event recognition (minimum bias trigger), event vertex location, and centrality determination. Both detectors work in very similar ways: they consist of north and south portions, functioning essentially as counters, and providing timing information from both sides. Events are recognized in both coincidental signals in the North and South detectors. The two de-

tectors have good timing timing resolution (BBC 50 ps, ZDC 100 ps) to differentiate the two coincidental signals and the timing difference then gives the event vertex z location. This way, PHENIX has two independent vertex measurements and minimum bias triggers. We can observe the locations of the detectors in the bottom panel of Figure 2.4.

2.4.1 Zero Degree Calorimeter

The zero degree calorimeters (ZDC) are hadron calorimeter detectors that are positioned about 18 m from the center of PHENIX [42]. They are located behind the steering DX magnets that sweep the charged beam particles back to and from the detector. Therefore, they detect only "spectator" fragments of collided nuclei, those neutrons whose momentum direction is essentially unchanged after the collision but are no longer bound to any charge. Charged particles from the collisions, such as "spectator" protons, are bent out of the ZDC acceptance by the DX magnets (see Figure 2.6).

This detector can quantify the number of different particles which hit them by the amount and locations of their energy response. This allows for a global multiplicity determination, which can ultimately be calibrated to a centrality determination (see section 3.1.2).

Each ZDC counter contains a module consisting of tungsten alloy plates with a depth of two hadronic interaction lengths, and each module is read out by a single PMT. The ZDC, like the BBC (see section 2.4.2), also provides timing information, though not as accurately as the BBC. The ZDC is an important part of the minimum-bias trigger in nucleus-nucleus collisions. Figure 2.6 shows a schematic view of the ZDC.

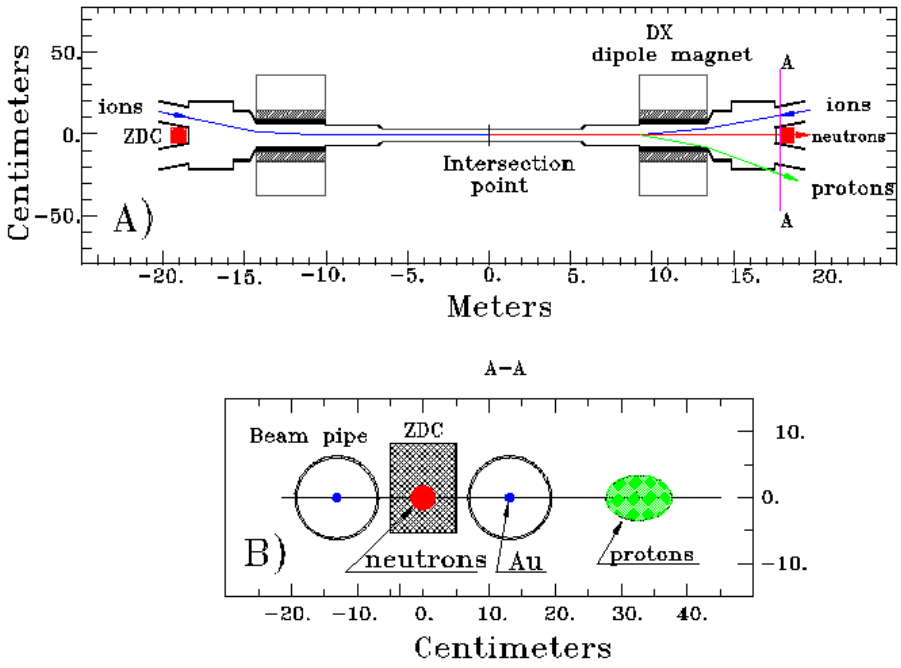

Figure 2.6: Top: Schematic top-view of PHENIX interaction region. Bottom: Projections of protons and neutrons deflection area in the plane of the ZDC.

2.4.2 Beam Beam Counter

The BBC detector is located at $3.0 < \eta < 4.0$ rapidity, and 1.44 m from the interaction point along the beam line (one on the north side, and one on the south side) [37]. It is basically an array of 64 photo tubes each with a $\check{C}$erenkov radiating piece of quartz wired to the front of it as illustrated in Figure 2.7. It therefore detects charged particles with sizable deflection form the event collision. The signals from here will always be particles produced in the collision, which will be a function of the number of participating nucleons. As is the case with the ZDC, the BBC quantifies the number of different particles which hits it. The BBC is also used as a cross-reference to determine centrality (see section 3.1.2).

Finally, the BBC timing is special in that this timing is used as the start time for events and all other detector electronics are therefore synchronized to this detector

2.7 (a)

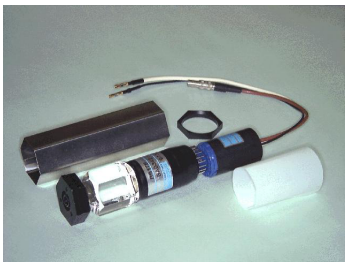

2.7 (b)

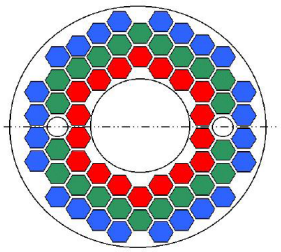

2.7 (c)

Figure 2.7: (a) Picture of the 64 PMTs comprising the BBC array. (b) B BC element consisting of one inch mesh dynode PMT mounted on a 3 cm quartz radiator. (c) Schematic of the BBC, with each box corresponding to a PMT.

2.5 Central Arm Spectrometer

PHENIX has two central arms at zero rapidity to detect electrons, photons, and charged hadrons. This is shown in the top of Figure 2.4. The central arm detectors consist of a tracking system for charged particles and an electromagnetic calorimeter. The tracking system consists of drift chambers (DC), pad chambers (PC1, PC2, PC3), and time expansion chambers (TEC). The ring imaging $\check{C}$erenkov (RICH), and time-of-flight (TOF.E, TOF.W) systems provide identification of charged particles [34, 36]. The electromagnetic calorimeter (EMCal) provides measurements of both photons and energetic electrons [35]. The EMCal can also be used as a TOF detector. The following sections describe the subsystems used for charged hadron measurements.

2.5.1 Drift Chamber

The DC subsystem measures charged particle trajectories in the $r-\phi$ plane to determine the transverse momentum of such particles. By combining the polar angle information

from the first layer of the PC with the transverse momentum, the total momentum p is determined. The DC is also used in the pattern recognition at high particle track densities by providing position information that is used to link tracks through the various PHENIX subsystems. An initial goal of the DC design was to measure the $\phi \rightarrow e^+e^-$ mass with a resolution better than its natural width of 4.4 MeV. This, along with the ability to perform good tracking efficientlyt for the highest multiplicities environment, placed the following design requirements on the DC: 1) single wire resolution better than 150 μm in $r-\phi$ plane, 2) single wire two track separation better than 1.5 mm, 3) single wire efficiency better than 99%, and 4) spatial resolution in the z directions better than 2 mm.

The DC system consists of two independent gas volumes filled with 50%-50% mixture of argon and ethane gas. The mixture was chosen due to its uniform charge drift velocity, high gain, and low diffusion coefficients. They are located in the west and east arms, respectively. The chambers in the east arm and the west arm are symmetric with respect to x = 0 plane. They are located in the region from 2.0 to 2.4 m from the beam axis, and 2.0 m along the beam direction.

Each DC volume is defined by a cylindrical titanium frame defining the azimuthal and beam-axis limits of the vector volume, see Figure 2.8 2.8. A 0.125 mm Al-mylar window defines the limits of the gas volume radially. Each frame is filled with drift chamber modules and is divided in 20 equal sectors covering 4.5° in ϕ. The DC contains a total of about 13000 readout channels organized in 40 layers of wires (see Figure 2.8 2.8). Two sets of wires, X1 and X2 with 12 wires each are parallel to the beam axis and serve to determine the track in the $r-\phi$ plane. Each of the X layers is followed by a set of stereo wires (U and V wires, (Figure 2.8 2.8) which serve to determine the z-coordinate of the track. In ad-

dition to the anode and cathode wires, each plane contains “gate” wires and “back” wires. The gate wires form charge collection regions which limit the track drift length to about 3 mm, reducing the detector occupancy. The back wires contain a low potential to block tracks from one side of the anode, which is done to reduce ambiguity regarding charge drifts between each side of the wire, see Figures 2.8 2.8 and 2.8 2.8 .

2.5.2 Pad Chambers

The pad chambers (PC) are multi-wire proportional chambers that form three separate layers of the PHENIX central tracking system. Each chamber contains a single plane of wires inside a gas volume between two cathode planes, each of which is segmented into an array of pixels. The basic element of the detector is a “pad” of 9 pixels. The PC system determines space points along the straight line particle trajectories outside the magnetic field. Figure 2.4 shows the radial location of the PCs in the central tracking arms. The first pat chamber layer (PC1) is located at the radial outer edge of each drift chamber (see Figure) at a distance of 2.49 m, while the third layer (PC3) is 4.98 m from the interaction point. The second layer (PC2) is located at a radial distance of 4.19 m in the west arm only.

Each cell contains three pixels and an avalanche must be seen by all three pixels to form a valid hit in the cell. The interleaved pixels are ganged together in nine by nine sets, and connected to a common readout channel. This is done this way so the three pixels in a cell are always connected to different but neighboring channels, and each cell is defined by its unique channel triplet. This configuration allows us to break the information down to the cell level by identifying the triplets.

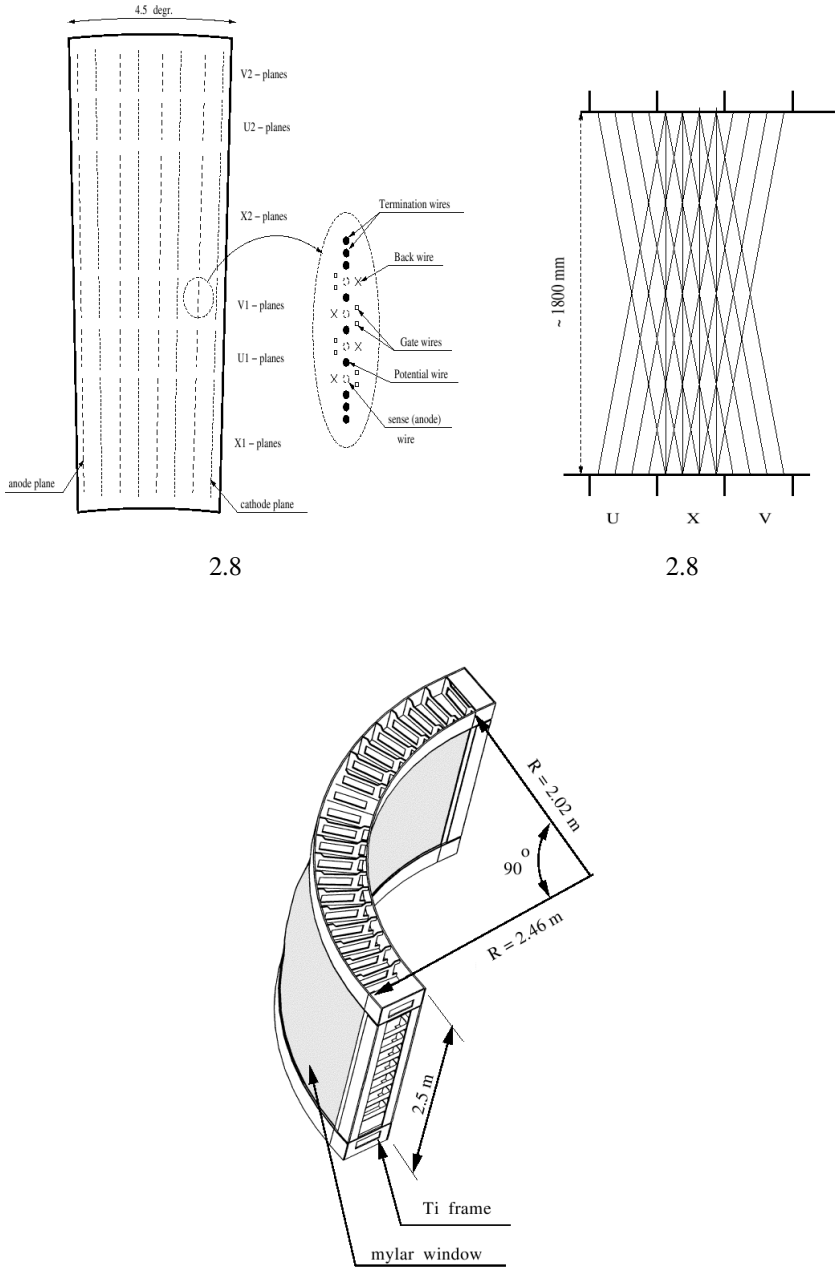

Figure 2.8: (a) Schematic of one arm of the drift chamber. (b) Wire position within one sector and inside the anode plane. (c) Top view of the stereo wire orientation.

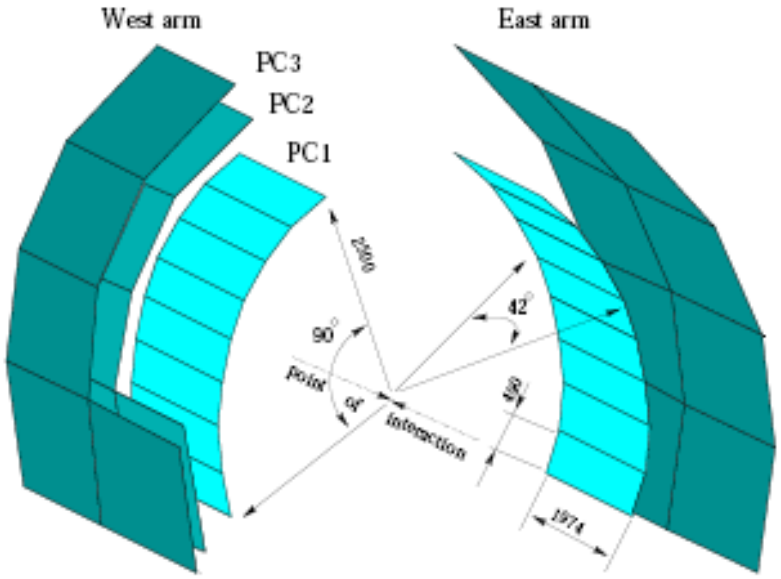

Figure 2.9: Schematic of the PHENIX pad chambers. Some sectors of the PC2 and PC3 sections are removed for clarity.

This solution saves a factor of nine in readout channels compared to readout of every pixel and a factor of three compared to a readout pad geometry where a cell is the actual electrode connected to an electronics channel. The design goals for the position resolution were $\pm$4 mm. This motivated an anode wire spacing of about 8 mm. For geometrical reasons, a spacing of 8.4 mm was chosen. A square cell geometry with coverage area of 8.4 x 8.4 mm^2 was also influenced by the final geometry. This resulted in a position resolution of $\pm$ 1.7 mm in the z direction which was substantially better than the design goals. At the position of PC2 and PC3, it is sufficient to maintain the same angular resolution as of PC1, see Figure 2.9. The cells on PC3 have 4 times the area of PC1 cells; PC3 is at roughly twice the distance from the vertex as compared to PC1.

2.5.3 Time of Flight West

The time-of-flight detector located in the west arm (TOF.W) serves as the primary particle identification device for charged hadrons for this arm. With timing resolution of σ_T $\sim$75 ps, the TOF.W provides a 4σ π/K and K/p separation up to p_T = 3 and 4.5 GeV/c, respectively. The TOF.W is located in two sectors of the arm. The "bottom" section of the TOF.W is located in sector 1 between PC3 and ACC. It is designed to cover $\mid \eta \mid < 0.35$ and $9.26\,^\circ$ in ϕ. The "top" section is located in sector two of the arm, positioned in between PC2 and PC3, covers the same area as the bottom section, for an overall area coverage of 8 m^2.

The TOF.W contains 128 Multigap Resistive Plate Chambers (MRPC) divided into four gas volumes. Figure 2.10 shows a schematic view of one MRPC. Each MRPC contains four double ended readout strips, for a total of 1024 readout channels. As part of my hardware training in Vanderbilt, I was directly involved in the construction of this detector.

2.6 Other Detectors

There are other detectors which were not used for this analysis. The following detectors are mainly used for lepton and photon measurements, as well as for particle ID. For completeness, we will just briefly mention their main functions.

The time-of-flight detector located in the east arm (TOF.E) serves as the primary particle identification device for charged hadrons for this arm. It is designed to have about $\pm$100 ps timing resolution in order to achieve clear particle separation in the high momentum region, i.e. π/K separation up to 2.4 GeV/c K/p separation up to 4.0 GeV/c.

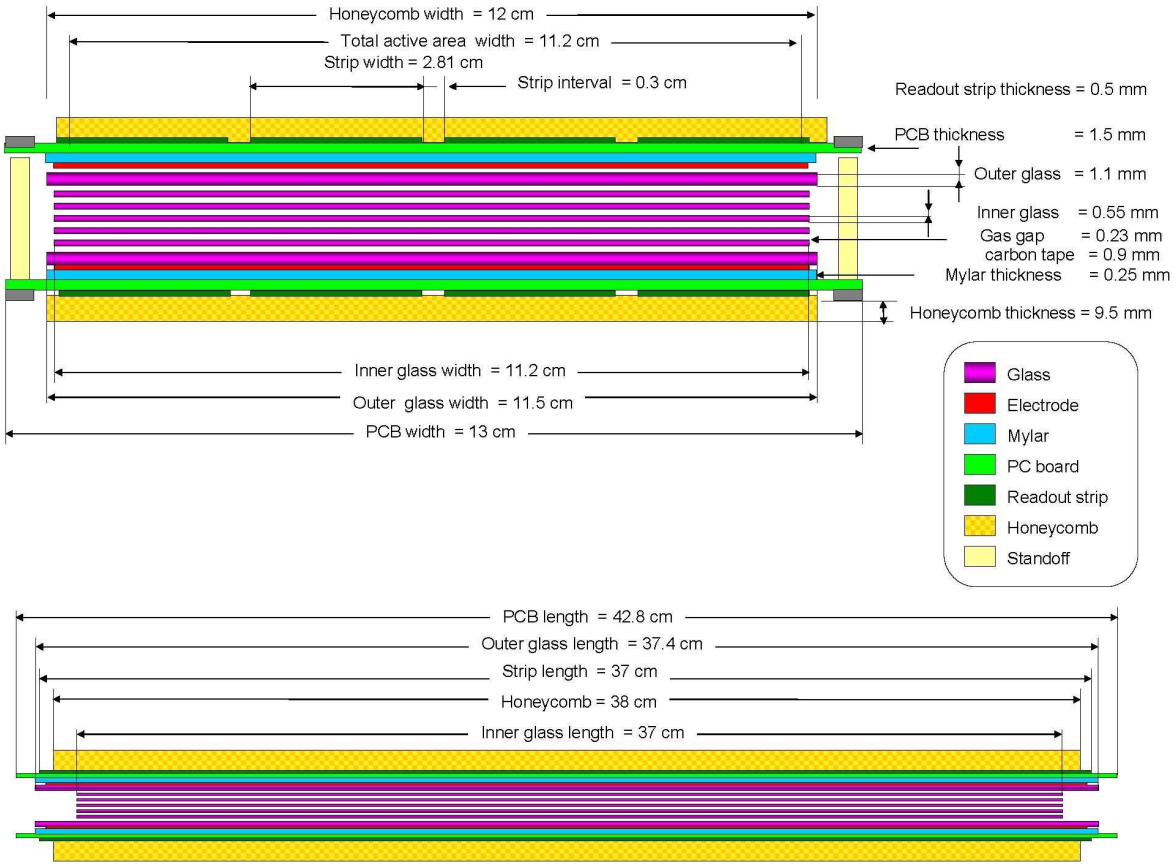

Figure 2.10: Cross sectional view of the TOF.W MRPC. All components and sizes are labeled in the figure. The two views are not to scale.

The Aerogel detector covers an area of 390 cm (z) x 120 cm (ϕ) x 30 cm (r) in the west carriage. The detector is located in sector 1 (W1) of the west arm, with a radial position (r = 4.5 m) located between PC2 and TOF.W. The detector consists of 160 boxes configured in a 16 (z) x 10 (ϕ) array. To eliminate dead space, every other cell along the z-direction is flipped in the radial direction. With this configuration, all the sensitive aerogel volumes are kept in one plane, which contributes to the uniform detector response. The Aerogel $\check{C}$herenkov detector (ACC) has an excellent trigger capability for high p_T particles.

The time expansion chamber (TEC) is composed of a set of 24 large multi-wire tracking chambers arranged in four six-chamber sectors which reside in the east arm. It measures all charged particles passing through its active area, providing direction vectors that are matched to additional track information from the DCs and PCs also located in this arm.

The ring imaging $\check{C}$erenkov (RICH) detector is designed for electron identification and provides e/π discrimination below the π $\check{C}$erenkov threshold, which is about 4 GeV/c. The RICH, in combination with the EMCal helps to limit the false identification of hadrons to better than one part in 10^4 below a momentum of 4.7 GeV/c.

The primary role of the electromagnetic calorimeter (EMCal) is to provide a measurement of the energies and spatial position of photons and electrons produced in heavy ion collisions [35]. With a $\sim$500 ps resolution, the EMCal also plays a major role in particle identification and is an important part of the PHENIX trigger system.

The two forward muon arms at rapidity $1.2 <| y |< 2.4$ with full azimuthal acceptance are designed to detect muons [39]. Each muon arm must track and identify muons and provide good rejection of pions and kaons (one part in 10^3). In order to achieve this, we employ a radial field magnetic spectrometer with precision tracking (Muon Tracks: MuTr)

followed by a stack of absorber low resolution tracking layers (Muon Identifier: MuID). The MuID is used for separating muons from charged hadrons and other background as well as providing a trigger for single particles and dimuons.

2.7 Data Acquisition and Triggering System

As we can see, PHENIX is a very complex detector. A system as sophisticated as this requires an even more elaborate data acquisition (DAQ) and triggering system, involving customized fast electronics and multiple *online* computer farms.

PHENIX is designed to make measurements for a variety of colliding systems from p+p to $Au + Au$. The occupancy in the detector varies from a few tracks in $p + p$ interactions to approximately 15% of all detector channels in central Au+Au interactions. The interaction rate at design luminosity varies from a few kHz for $Au + Au$ collisions to approximately 500 kHz for $p + p$ collisions. The PHENIX DAQ system [40, 41] is designed to be flexible enough to accommodate improvements in the luminosity. This is accomplished through the pipelined and dead-time-less features implemented to the detector front end modules (FEMs) and the ability to accommodate higher-level triggers.

The wide range of events sizes and luminosities present special challenges for triggering and data acquisition. In PHENIX, it is necessary to measure low-mass lepton pairs and low p_T particles in a high background environment. In order to preserve the high interaction rate capability, a flexible triggering system that permits tagging of events is constructed. The DAQ system has two levels of triggering denoted as level 1 (LVL1) and level 2 (LVL2). The LVL1 trigger is fully pipelined. The buffering in the pipeline is sufficient to handle

fluctuations in the event rate so that dead-time is reduced to less than 5% for full RHIC luminosity. The LVL1 trigger and lower levels of readout are clock-driven by bunch-crossing signals from the 9.4 MHz RHIC clock. The higher levels of readout and the LVL2 trigger are data-driven, where the results of triggering and data processing propagate to the next higher level only after processing of a given event is completed.

The schematics of the PHENIX data acquisition system are shown if Figure 2.11. Signals from the various PHENIX subsystems are processed by Front End Electronics (FEE) that convert detector signals into digital events fragments. This involves analog signal processing with amplification and shaping to extract the optimum time and/or amplitude information, development of trigger input data, and buffering to allow time for data processing by the LVL1 trigger and digitization. This is carried out for all detector elements at every beam crossing synchronously with the RHIC beam clock. The timing signal is a harmonic of the RHIC beam clock and is distributed to the FEMs by the PHENIX Master Timing System (MTS). The LVL1 trigger provides a fast filter for discarding empty beam crossing and uninteresting events before the data is fully digitized. It operates in a synchronous pipelined mode, generates a decision every 106 ns, and has an adjustable latency of some 40 beam crossings.

Once an event is accepted, the data fragments from the FEMs and primitives from the LVL1 trigger move in parallel to the Data Collection Modules (DCM). The PHENIX architecture was designed so that all detector-specific electronics end with the FEMs, so that there is a single set of DCMs that communicate with the rest of the DAQ system. The DCM's perform zero suppression, error checking, and data reformatting. Many parallel data streams from the DCMs are sent to the Event Builder (EvB). The EvB performs the

final stage of event assembly and provides an environment for the LVL2 trigger to operate. In order to study the rare events for which PHENIX was designed, it is necessary to reduce further the number of accepted events that are being assembled in the Assembly and Trigger Processors (ATP) in the EvB by selecting designating LVL2 triggers. The EvB then sends the accepted events to the PHENIX On-line Control System (ONCS) for logging and monitoring. The recorded raw data are sent to the RHIC Computing Facility (RCF) for storage on the tape device in the High Performance Storage System (HPSS). The raw data are converted into an intermediate data format for the analysis.

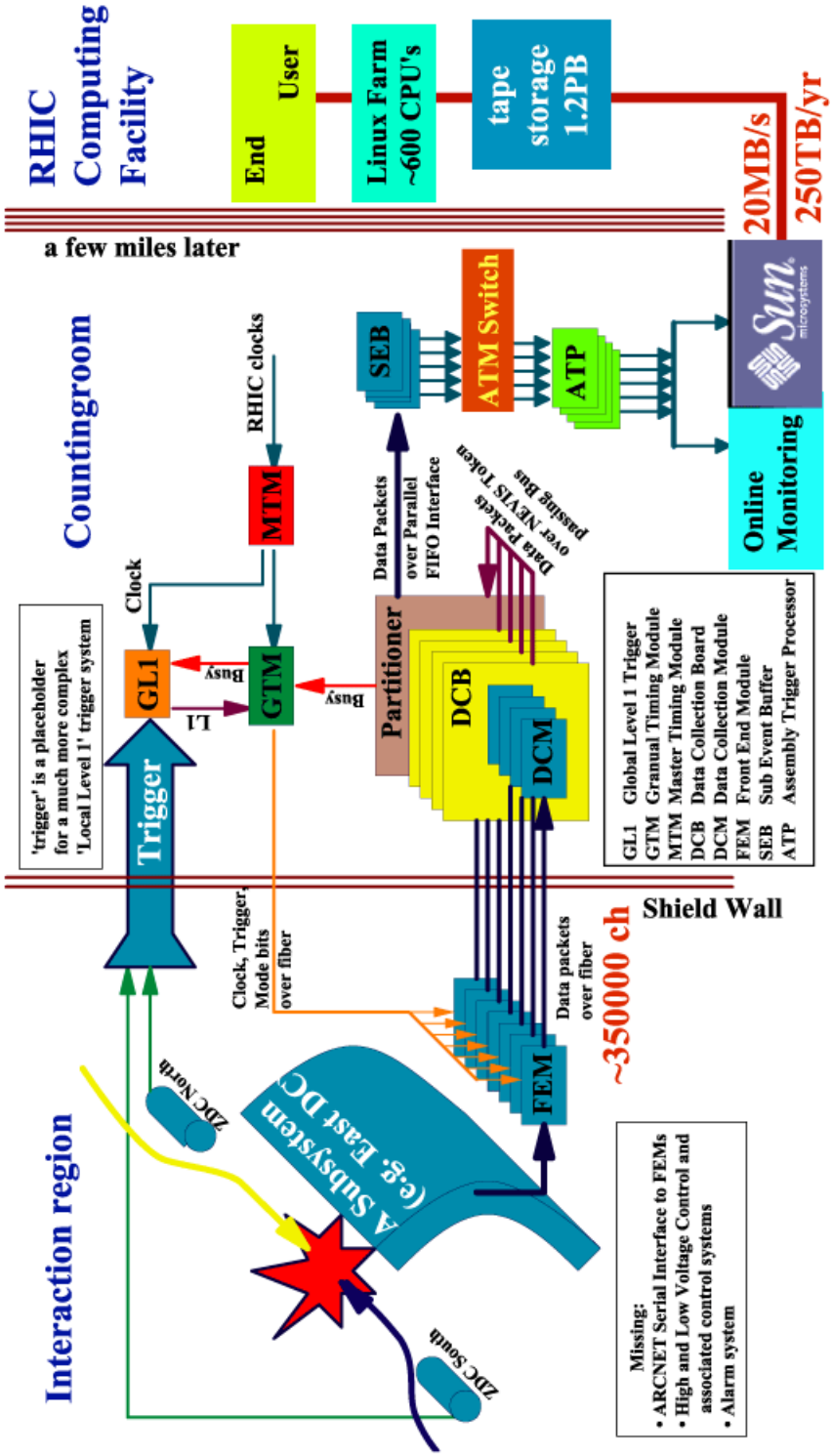

Figure 2.11: Block diagram of DAQ.

CHAPTER III

DATA ANALYSIS

This analysis is based on the experimental data from $Au+Au$ collisions at $\sqrt{s_{NN}} = 200$ GeV. The data was taken during the 2007 data taking period at RHIC (Run 7). In this chapter, we describe the event selection, track selections, momentum determination of particles, and the identification of deuterons and anti-deuterons. In order to obtain absolutely normalized transverse momentum distributions, the data collection needs to be corrected for geometrical acceptance, survival probability of deuterons and anti-deuterons passing through the detector material, and detector occupancy. The transverse momentum distributions are the starting point for all the other physics results obtained in this thesis. These results are presented in Chapter IV.

3.1 Event Selection

RHIC has been operational for eight years, and during this time, the scientists have made significant improvements in the accelerator performance, *e.g.* increase in the recorded integrated luminosity. During this time, PHENIX has also improved our DAQ system which allows us to increase the number of events recorded. A detailed overview of all data sets taken by PHENIX including colliding species, integrated luminosity, total number of events, and data size is illustrated in Table 3.1. The data used in this thesis, as mentioned before, is from the seventh year of RHIC operations (Run 7).

Table 3.1: PHENIX runs information.

	Year	Species	$\sqrt{s}$ GeV	$\int Ldt$	$N_{tot(sample)}$	Data Size
Run1	2000	$Au+Au$	130	1 μb^{-1}	10 M	3 TB
Run2	2001/2202	$Au+Au$	200	24 μb^{-1}	170 M	10 TB
		$Au+Au$	19		<1 M	
		$p+p$	200	0.15 pb^{-1}	3.7 B	20 TB
Run3	2002/03	$d+Au$	200	2.74 nb^{-1}	5.5 B	46 TB
		$p+p$	200	0.35 pb^{-1}	6.6 B	35 TB
Run4	2003/04	$Au+Au$	200	241 μb^{-1}	1.5 B	270 TB
		$Au+Au$	62.4	9 μb^{-1}	58 M	10 TB
Run5	2005	$Cu+Cu$	200	3 nb^{-1}	8.6 B	173 TB
		$Cu+Cu$	62.4	0.19 nb^{-1}	0.4 B	48 TB
		$Cu+Cu$	22.4	2.7 μb^{-1}	9 M	1 TB
		$p+p$	200	3.8 pb^{-1}	85 B	262 TB
Run6	2006	$p+p$	200	10.7 pb^{-1}	233 B	310 TB
		$p+p$	62.4	0.1 pb^{-1}	28 B	25 TB
Run7	2007	$Au+Au$	200	813 μb^{-1}	5.1 B	650 TB
Run8	2007/08	$d+Au$	200	80 nb^{-1}	160 B	437 TB
		$p+p$	200	5.2 pb^{-1}	115 B	118 TB
		$Au+Au$	9.2		few K	

3.1.1 Minimum Bias Trigger

For this analysis, we used the PHENIX minimum bias triggered events which are determined by the following conditions on the BBC and ZDC.

- A coincidence between the north and south BBC with at least two PMTs fired in each BBC is required. The collision vertex position has to satisfy $|z_{vtx}| < 75$ cm. These cuts are performed online by the BBC Level-1 (BBCLL1) trigger (BBCLL1>=2).

- At least one forward neutron has to be detected in each of the two ZDCs (ZDCNS).

- An offline collision vertex cut of $|z_{vtx}| < 30$ cm is required.

The trigger efficiency for minimum bias $Au+Au$ nuclear interactions related to these cuts is studied by a detailed simulation of the BBC and ZDC response [43]. The minimum

bias trigger captures ≈92% of the total geometric cross-section.

3.1.2 Centrality Determination

The events are classified by centrality, which is related to the measured fraction of the total geometrical cross-section between the two colliding nuclei. The ZDC measures spectator neutrons that are not bound in deuterons or heavier fragments. The BBC measures the number of charged particles at forward rapidity. The centrality is determined by the combined information on spectator neutrons measured by the ZDC and the charged sum information measured by the BBC as shown in Figure 3.1. Different centrality classes are chosen by appropriate cuts in ZDC-BBC space as shown in Figure 3.2. In this figure, the response of both detectors is shown for a large event sample. The centrality is defined such that each 5% centrality bin contains an equal number of events. The lines superimposed on the distribution defined different "slides" of centrality. The number of participants, N_{part}, is defined as the number of nucleons in the overlap region, as seen in Figure 3.1. Collisions with vanishing impact parameter, that is where there is total overlap, are called the "most central" whereas collisions where the impact parameter is nearly equal to the nuclear radius, that is where there is almost no overlap, are called the "most peripheral". Therefore, the most central collisions (0-10%) have the largest N_{part}, and the most peripheral (80-92%) have the smallest.

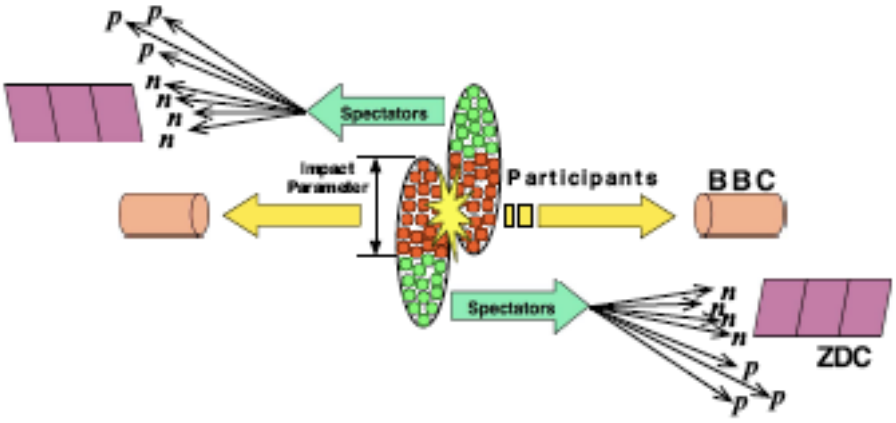

.

Figure 3.1: A schematic figure showing nucleus-nucleus collisions. Nucleons which have interacted with other nucleons are called "participants". Nucleons which have not interacted go straight with initial momenta are called "spectators". Protons in the spectators are swept out by the accelerator dipole magnet and only neutrons are emitted in the ZDCs.

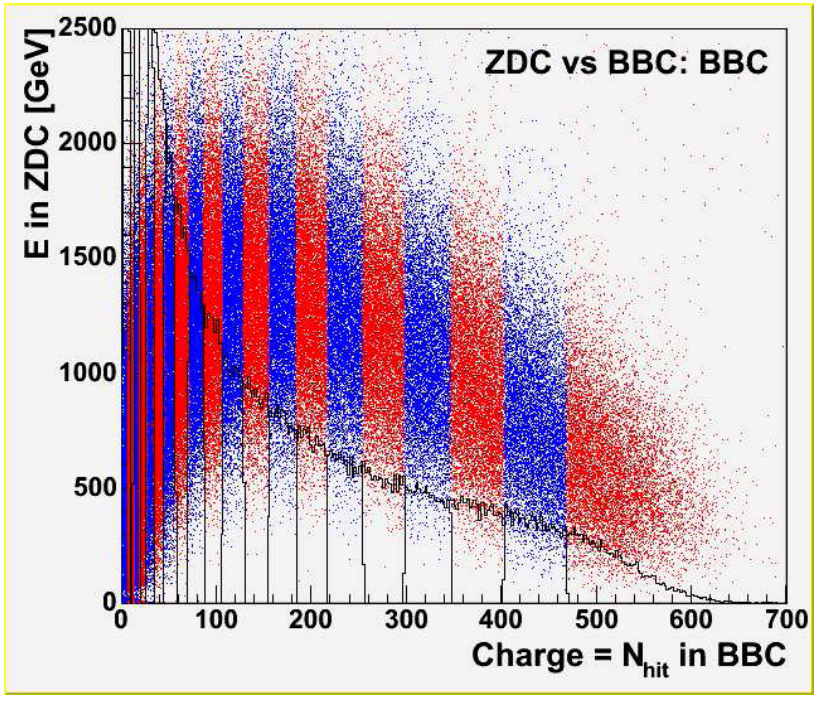

Figure 3.2: ZDC vs BBC scatter-plot used to calculate centrality bin cuts by BBC. The lines show the definition of centrality classes from this correlation.

3.1.3 Glauber Model Calculation

Another important quantity for the classification of any observable produced in hard process is the number of nucleon-nucleon binary collisions N_{coll}. N_{coll} is calculated using the Glauber model [44] Monte-Carlo simulation. This model uses the response of the BBC and ZDC detectors. Here, a participant is defined as a nucleon which has suffered at least one inelastic nucleon-nucleon collisions. The average number of binary collision $< N_{coll} >$ and the geometrical nuclear overlap function T_{AB} are related quantities:

$$T_{AB} =< N_{coll} > /\sigma_{NN} \tag{3.1}$$

where σ_{NN} is inelastic nucleon-nucleon cross section. Based on a Glauber model calculation, T_{AuAu}, N_{coll}, and N_{part} are obtained for each centrality bin used in this analysis. For a comparison of N_{part} and N_{coll}, see Table 3.2.

Table 3.2: Average number of participants $< N_{part} >$ and collisions $< N_{coll} >$ in $Au+Au$ obtained from Glauber Monte Carlo [44]. The error associated with each number is the systematic error.

Centrality (%)	$\langle N_{part} \rangle$	$\langle N_{coll} \rangle$
0 - 10	325.2 $\pm$ 3.3	955.4 $\pm$ 93.6
10 - 20	234.6 $\pm$ 4.7	602.6 $\pm$ 59.3
20 - 30	166.6 $\pm$ 5.4	373.8 $\pm$ 39.6
30 - 40	114.2 $\pm$ 4.4	219.8 $\pm$ 22.6
40 - 50	74.4 $\pm$ 3.8	120.3 $\pm$ 13.7
50 - 60	45.5 $\pm$ 3.3	61.0 $\pm$ 9.9
60 - 70	25.7 $\pm$ 3.8	28.5 $\pm$ 7.6
70 - 80	13.4 $\pm$ 3.0	12.4 $\pm$ 4.2
80 - 92	6.3 $\pm$ 1.2	4.9 $\pm$ 1.2
60 - 92	14.5 $\pm$ 2.5	14.5 $\pm$ 4.0
0 - 92 (Min. Bias)	109.1 $\pm$ 4.1	257.8 $\pm$ 25.4

3.2 Track Reconstruction

Once the characteristics of an event are known, information about all the "tracks" coming out of such event are reconstructed. This process involves the identification of particle tracks through the detectors which is then used to determine the tracks momentum.

3.2.1 Track Algorithm

The tracking algorithm used by the drift chamber must have a high single track efficiency, while simultaneously being able to perform well in a high multiplicity environment, keeping falsely reconstructed "ghost" tracks to a minimum. A perfect track would create 6 hits in both the X1 and X2 sections. The efficiency of each wire varies across channels, but is between 90% and 95% for all wires. If we require tracks to have at least 4 hits in both X1 and X2 sectors of the detector, then the single track efficiency is better than 99%. The first stage of the tracking algorithm uses a combinatorial Hough transform [45] and assumes that the particles have a straight line trajectory inside the drift chamber volume. The output of the Hough transform consist of two angles, ϕ and α, as illustrated in Figure 3.3. After the Hough transform has been applied, the next step is the algorithm for the removal of background tracks. First, a robust fitting procedure is used to provide tighter constraints on whether a hit is associated with a track. An iterative linear fitting approach is used, weighting hits according to their deviation from a straight line guess so that the fit is not disturbed by hits from noise or other tracks. The closest track remaining to the given hit is kept, while the hit is removed from all other associated track candidates. Tracks with fewer than 8 total associated hits are discarded.

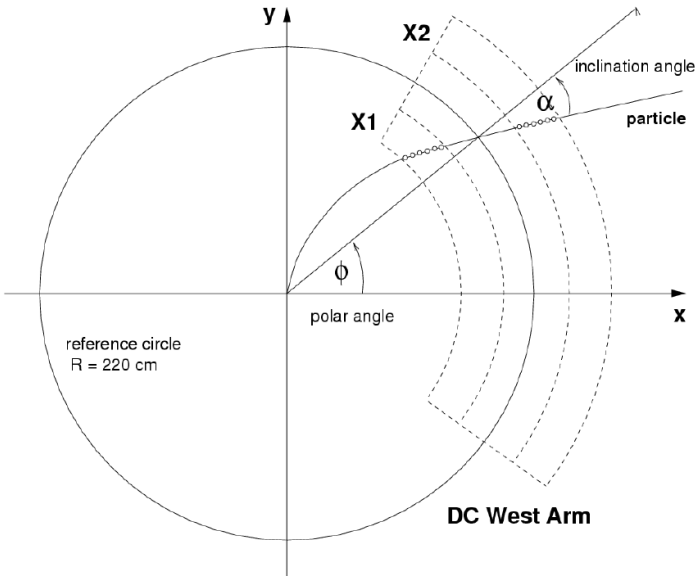

Figure 3.3: Definition of the Hough transform parameters ϕ and α in the DC track reconstruction.

The above algorithm only gives track information on the $r - \phi$ plane. If there is a hit on the PC1 associated with the projection of a track candidate from the X1, X2 section, then the z position of the PC1 hit fixes the track in three dimensions. If there is more than one associated PC1 hit, then the PC1 hit with the most associated hits in the U and V sections of the drift chamber is used.

3.2.2 Momentum Determination

The momentum (in GeV) determined by the DC is related to the angle of bending α (in mrad) by the following equation:

$$\alpha \simeq \frac{K_1}{p} \tag{3.2}$$

where K_1 is the field integral,

$$K_1 = \int_{0.3/R_{DC}} lBdl = 74 \quad mrad \quad GeV/c \tag{3.3}$$

However, due to the small non-uniformity of the focusing magnetic field along the flight path of charged particles, an accurate analytical expression for the momentum of the particles cannot be determined. A four-dimensional field integral grid was constructed within the entire radial extent of the central arm. This allows for momentum determination based on DC hits. The variables in the grid are the vertex on the z-direction, z_{vtx}, the polar angle θ_0 of the particle at the vertex, the momentum p, and radius r, at which the field integral $f(p, r, \theta_0, z)$ is calculated. The field integral grid is generated by explicitly "swimming" particles through the magnetic field map from survey measurement and numerically integrating to obtain $f(p, r, \theta_0, z)$ for each grid point. An iterative procedure is used to determine the momentum for reconstructed tracks using equation 3.2 as an initial assumption. For this analysis, a momentum cut of $0.5 < p < 10.0$ GeV/c was applied.

3.2.3 Track Association

In order to associate a track with a hit on the TOF.W, the track is projected to its expected hit location on the TOF.W. The residual distributions (hit position minus the projected track location) in the z and ϕ are fitted with Gaussian functions. The widths of the residual distributions are larger at small momentum due to multiple scattering of the particles in the material. At high momentum, the width is governed by the drift chamber track pointing resolution and the position resolution in the detector to which the track is

projected. Since we are interested in measuring absolutely normalized particle spectra, it is important to know what fraction of the tracks survive the cuts imposed in the analysis. For this reason it is convenient to parameterize all relevant distributions on which cuts are being made in terms of their Gaussian width (σ). In this analysis, tracks are required to have a hit on the TOF.W and on the PC3 within $\pm 2\sigma$ of the expected hit location in both the azimuthal and the z directions. The flight path-length is calculated from a fit to the reconstructed track trajectory.

3.3 Particle Identification

The particle identification (PID), is performed by using the combination of three measurements: time-of-flight from BBC and TOF.W, momentum from the DC, and flight path-length from the collision vertex point to the hit position on the TOF.W wall. The mass squared is derived from the following formula,

$$m^2 = p^2(\frac{t^2c^2}{d^2} - 1) \tag{3.4}$$

where t is the time of flight from TOF.W, d is the TOF.W path-length, and c is the speed of light. The charged particle identification is performed using cuts in m^2 and momentum space.

In Figure 3.4 shows an example of a Run 7 data PID histogram showing the m^2 distribution integrated over all reconstructed momenta. Deuterons are well separated from protons as seen in Figure 3.5 for all measured momenta. The new TOF.W detector with a timing resolution $\sim$90 ps before subtraction of BBC timing (40 ps) (see Figure 3.6) extended our

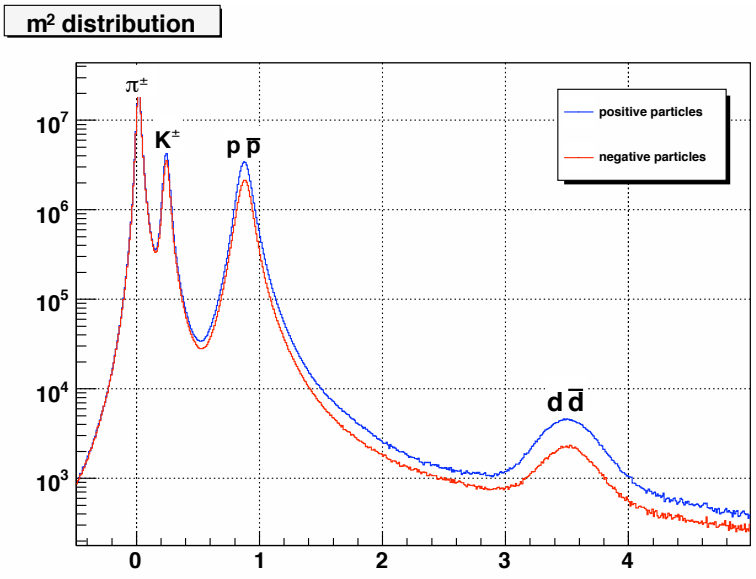

Figure 3.4: m^2 distribution with TOF.W from Run 7 $Au + Au$ data.

PID capabilities. The analysis itself it is limited by statistics and background rather than PID.

3.3.1 Cut Conditions

The cut conditions used in this analysis are summarized in Table 3.3.1. Most of the cuts are commonly used in PHENIX analysises, *e.g.* minimum bias event selection, BBC z-vertex cut, and track quality selection, but there are a few extra cuts (fiducial cuts, see Appendix B) for the DC, PC3, and TOF.W detectors. We used the same (or equivalent) cuts on the single particle Monte Carlo output to get the necessary bin-by-bin corrections. Please refer to Section 3.4 for more details about single particle Monte Carlo simulation.

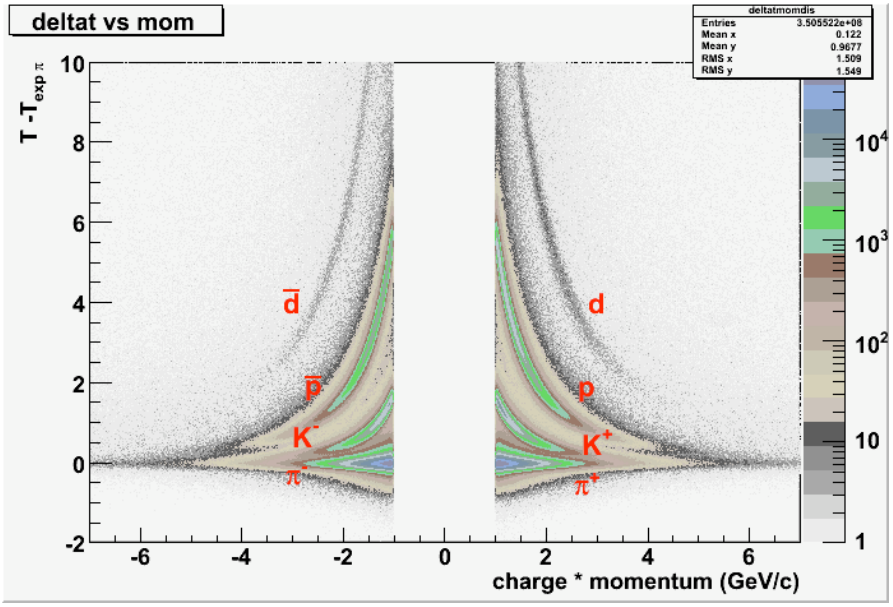

Figure 3.5: $T - T_{exp}$ vs. charge*momentum using the TOF.W from Run 7 $Au + Au$ data.

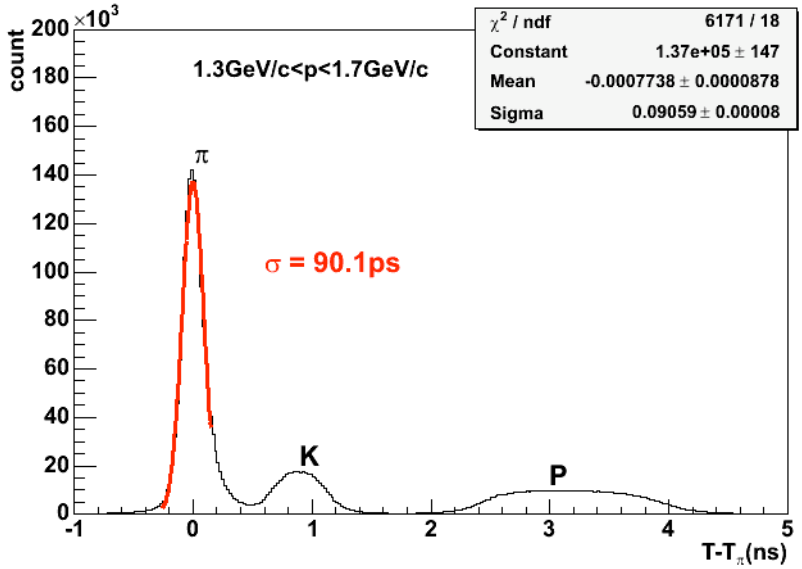

Figure 3.6: Timing resolution for TOF.W from Run 7 $Au + Au$ data.

Table 3.3: Cut conditions.

Cut	Value
Trigger	Minimum Bias
BBC z-vertex cut	$\pm$ 30 cm
DC-PC1 zed cut hits	$\|Z\| < 75$ cm
Fiducial Cut	see Section
DC track quality	31 or 63 (X1 && X2 w/ and w/o unique PC1 association)
TOF.W Matching cut	2σ spatial matching cut
PC3 Matching cut	2σ spatial matching cut
TOF.W energy loss cut	see Section
Momentum cut	$0.5 < p < 10.0$ (GeV/c)

3.3.2 Signal Extraction for Deuterons

To extract the deuteron yield as a function of transverse momentum and centrality classes, we construct an array of mass-squared distribution shown in Figures 3.7, A.1, A.2, A.3 for deuterons and Figures 3.8, A.4, A.5, A.6 for anti-deuterons. Although track quality selection cuts have been made, significant background remains under the deuteron mass peak and needs to be subtracted. We extracted (anti-)deuterons yields using a Gaussian fit for the signal and an exponentially falling distribution to fit the background. The deuteron yield is given by the integral under a Gaussian function:

$$N_d = \sqrt{2\pi} A_d \sigma_d \tag{3.5}$$

where A_d is the amplitude and σ_d is the sigma of the Gaussian. In order to obtain directly the statistical error on the yield associated with the fit, we rearrange the fit parameter. Thus

Table 3.4: Raw yields vs p_T (mid-point) and $\langle p_T \rangle$ for minimum bias (+-Field) events.

p_T GeV/c	$\langle p_T \rangle$	Deuterons (MB)	Anti-deuterons(MB)
1.1	1.10086	4427.41 $\pm$ 58.0521	1483.27 $\pm$ 38.5796
1.3	1.30029	5661.09 $\pm$ 40.997	2325.14 $\pm$ 28.7577
1.5	1.49971	6355.35 $\pm$ 39.0367	2717.35 $\pm$ 27.3102
1.7	1.69914	6358.07 $\pm$ 36.8747	2745.61 $\pm$ 25.7281
1.9	1.89857	5987.38 $\pm$ 34.5328	2534.27 $\pm$ 24.1493
2.1	2.09799	5184.5 $\pm$ 31.6737	2219.27 $\pm$ 22.0473
2.3	2.29742	4182.61 $\pm$ 28.4752	1783.12 $\pm$ 19.9874
2.5	2.49685	3257.86 $\pm$ 27.1362	1387.16 $\pm$ 17.7874
2.7	2.69628	2488.69 $\pm$ 24.9539	1029.73 $\pm$ 15.753
2.9	2.8957	1760.28 $\pm$ 22.689	737.659 $\pm$ 15.8795
3.1	3.09513	1170.89 $\pm$ 17.5749	507.752 $\pm$ 14.6618
3.3	3.29456	767.217 $\pm$ 15.0635	326.532 $\pm$ 13.5669
3.5	3.49399	478.667 $\pm$ 12.8242	199.174 $\pm$ 12.2101
3.8	3.77288	402.942 $\pm$ 13.2947	178.5 $\pm$ 10.7544
4.25	4.20045	239.808 $\pm$ 14.7765	70.5604 $\pm$ 11.7271
5.0	4.78034	85.2449 $\pm$ 28.4287	39.6173 $\pm$ 24.806

we fit the mass squared histogram with the following function:

$$f(x) = \frac{N_d}{\sqrt{2\pi}\sigma} exp(-\frac{x^2}{2\sigma^2}) + Background \tag{3.6}$$

where

$$N_d = \int_{-\infty}^{+\infty} A_d * exp - \frac{(x - x_0)^2}{2} \sigma^2 dx \tag{3.7}$$

The mass squared distribution for deuterons fit with equation (3.6) are shown in the following figures 3.7, A.1, A.2, A.3. The mass squared distribution for anti-deuterons fit again with equation (3.6) are shown in Figures 3.8, A.4, A.5, A.6.

Raw spectra for deuterons and anti-deuterons are shown in Figure 3.9. Raw counts

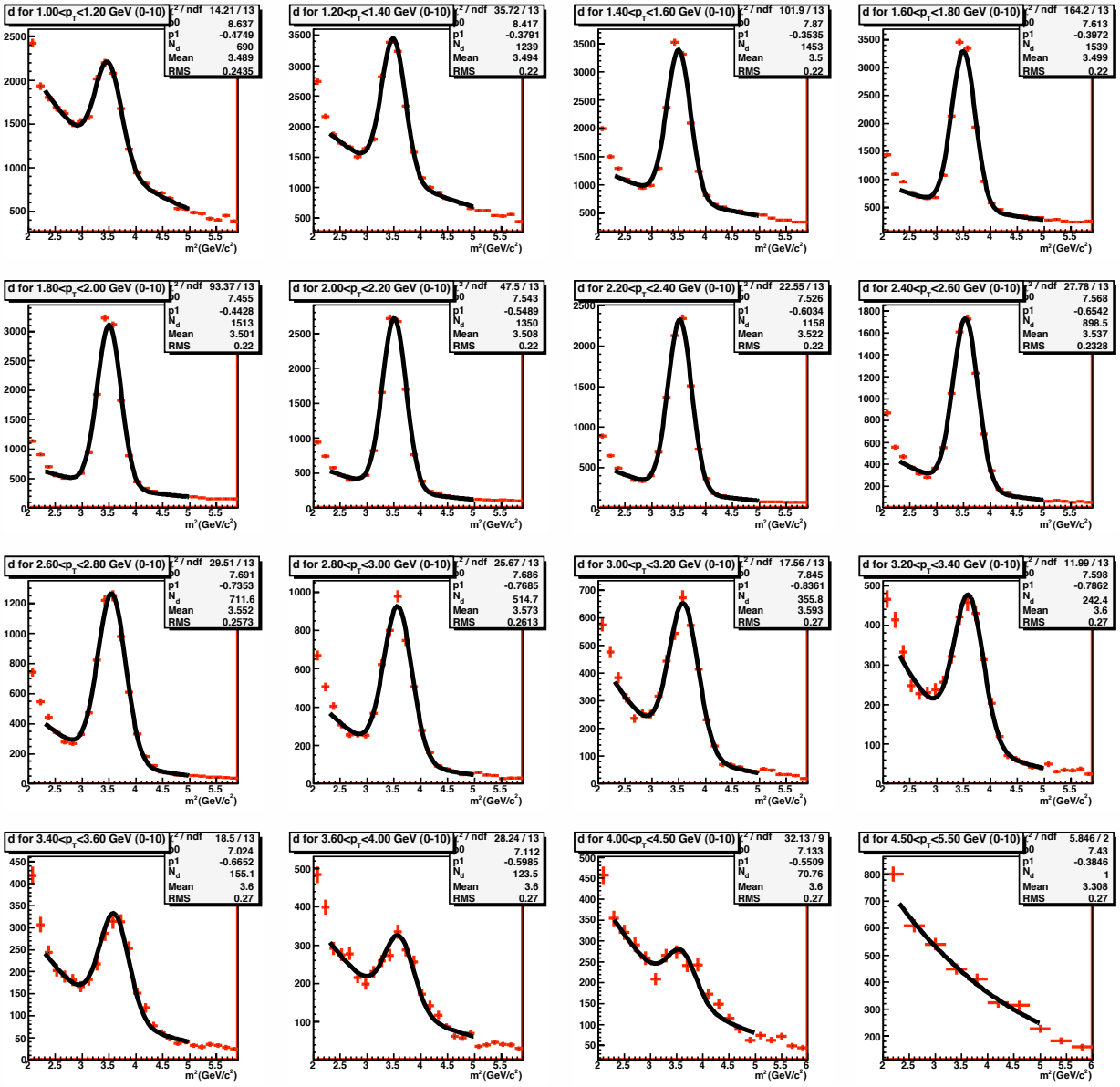

Figure 3.7: Raw deuteron yield for 0-10% centrality.

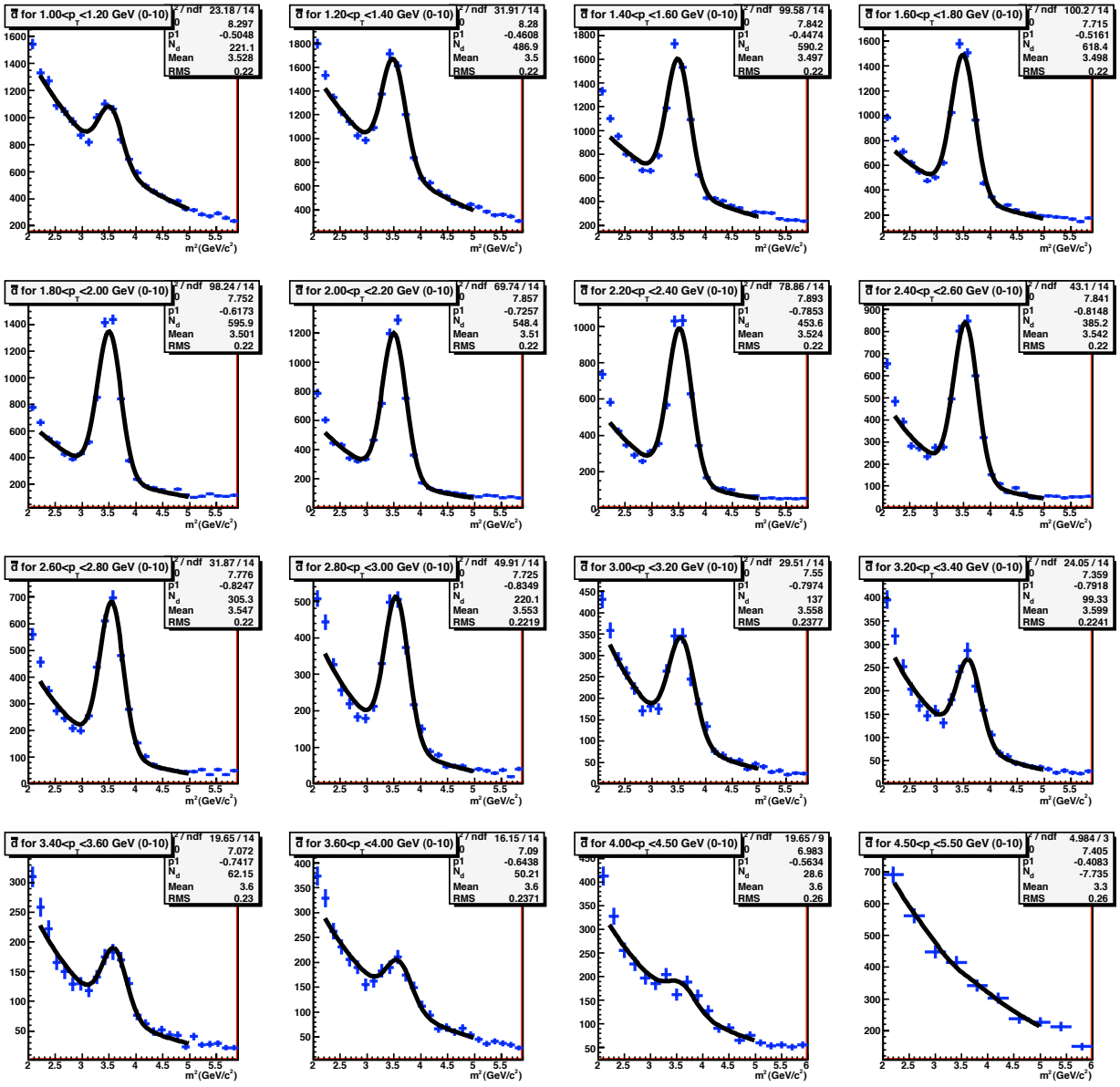

Figure 3.8: Raw anti-deuteron yield for 0-10% centrality.

for the 2.1 billion events analyzed ("+- Field [a] ") are extracted from the fitting procedure described above are listed in Table 3.4. In this final, we used the full data size for Run 7, 5.1 billion events.

Because we use wide bins in transverse momentum and the distribution is exponentially falling, the mid-point of the bin does not correspond to the mean p_T of the bin. We report the yield at the position of the mean p_T as:

$$\langle p_T \rangle = \frac{\int_{p1}^{p2} p_T f(p_T) dp_T}{\int_{p1}^{p2} f(p_T) dp_T} \tag{3.8}$$

where $f(p_T)$ is a Gaussian function used to fit the data. The raw yields as a function of p_T are shown in Figure 3.9.

3.4 Single Particle Monte Carlo Simulations

In order to obtain absolutely normalized invariant yield distribution, we need to take into account that the detector does not cover the full solid angle and is not perfectly efficient. Single particle Monte Carlo simulations are used to compensate for the cuts applied in the analysis, track reconstruction efficiency, and geometric acceptance. It is customary to report the experimental results for the invariant yield at mid-rapidity and within one unit of rapidity. The PHENIX detector does not cover a full unit of rapidity. However, we assume that the distributions are flat within $-0.5 \leq y \leq 0.5$. This is expected to hold, since measurements from the BRAHMS and PHOBOS experiments indicate a wide mid-rapidity

[a] PHENIX usually runs data for two magnetic fields, the two data sets allow for detector and acceptance studies. For Run 7, the two magnetic field configuration were +- field and -+ field, they are roughly equal in data size. The total data size for Run is 5.1 billions events.

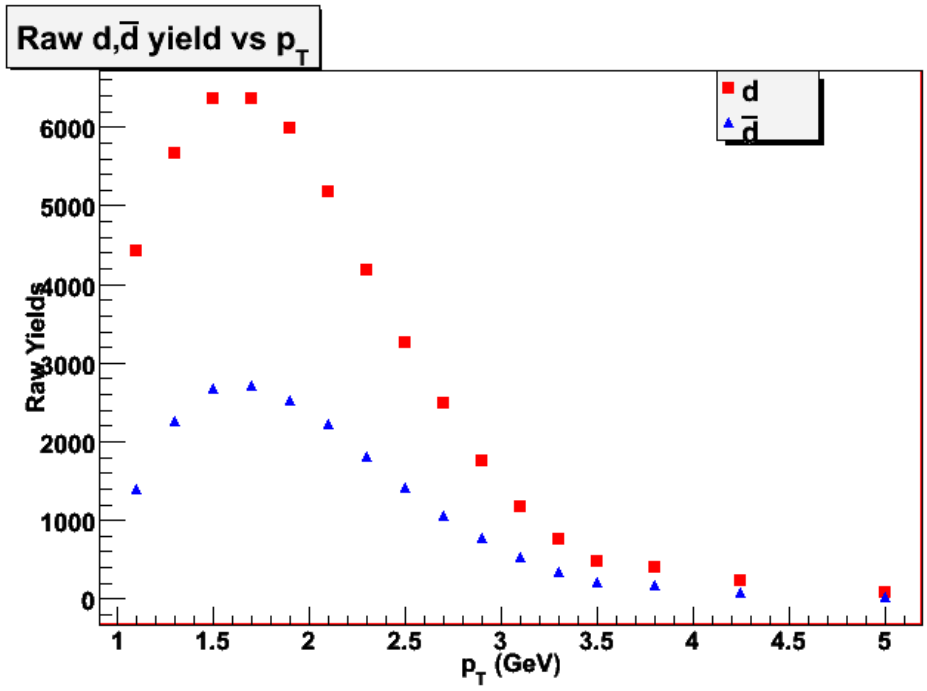

Figure 3.9: Raw spectra for deuterons and anti-deuteron minimum bias centrality, +- Field.

plateau of the measured charged particle yield. The PHENIX detector has a pseudo-rapidity coverage of $-0.35 < \eta < 0.35$ which translates into rapidity acceptance for pi, K, p, d as shown in Figure 3.10.

Five million (anti-)deuteron events were generated using the EXODUS single particle Monte Carlo generator. To save CPU cycles and disk-space, these events were generated for the west arm only (-0.698 $< \phi <$ +1.091 in rad) [b], with a rapidity coverage of $|y| < 0.6$, p_T ranges from 0.5 to 8 GeV/c with a flat transverse momentum distribution and vertex location within 30 cm of the nominal origin of the PHENIX coordinate system. Assuming that the distributions are symmetric in the azimuthal angle, we correct for the acceptance loss due to the limited simulation range. The events are processed using the PHENIX PISA

[b] This is actually 6.25 degrees more on each side (top, bottom) of the west arm.

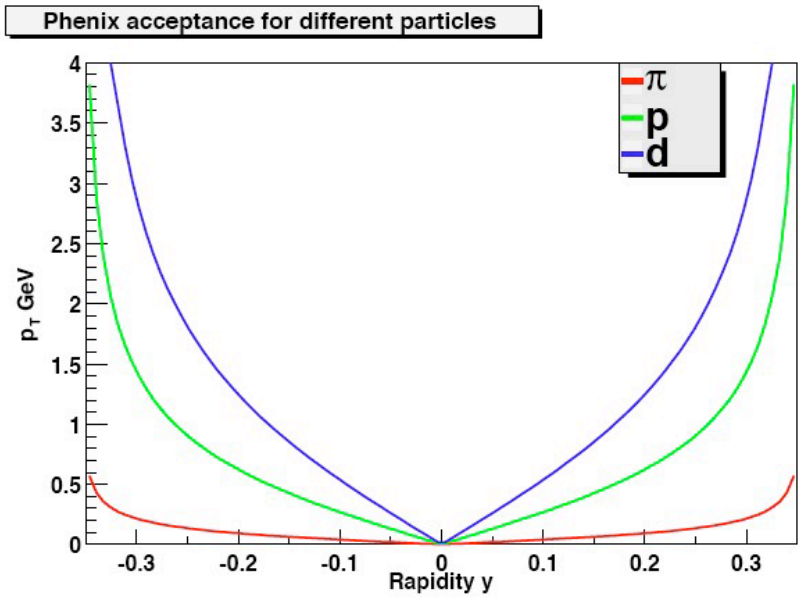

Figure 3.10: PHENIX rapidity Acceptance for pions, protons, and deuterons.

software package, which is a GEANT-based Monte Carlo [46] detector simulation software for the PHENIX detector. The PISA output files were then reconstructed to produce the simulation Data Summary Tapes (sim DSTs). The sim DSTs were then analyzed with exactly the same cuts used on the real data, so that we can correct for acceptance efficiency (ϵ_{acc}) of reconstruction, and our various track quality and matching cuts, as well as an ADC cut (see Section 3.6.1) (ϵ_{eff}). The p_T dependent correction factors are determined as follows:

$$\frac{dN_{gen}/dp_T}{dN_{reco}/dp_T} = \epsilon_{acc} * \epsilon_{eff} * x \tag{3.9}$$

where the $dNgen/dp_T$ is the total number of events generated by EXODUS, $dNreco/dp_T$ are the total number of events reconstructed by PISA, and x, a factor to account for ϕ angle and y coverage which contains trivial geometric factors discussed previously.

Once the calculations are performed, a set of bin by bin corrections for (anti)-deuterons,

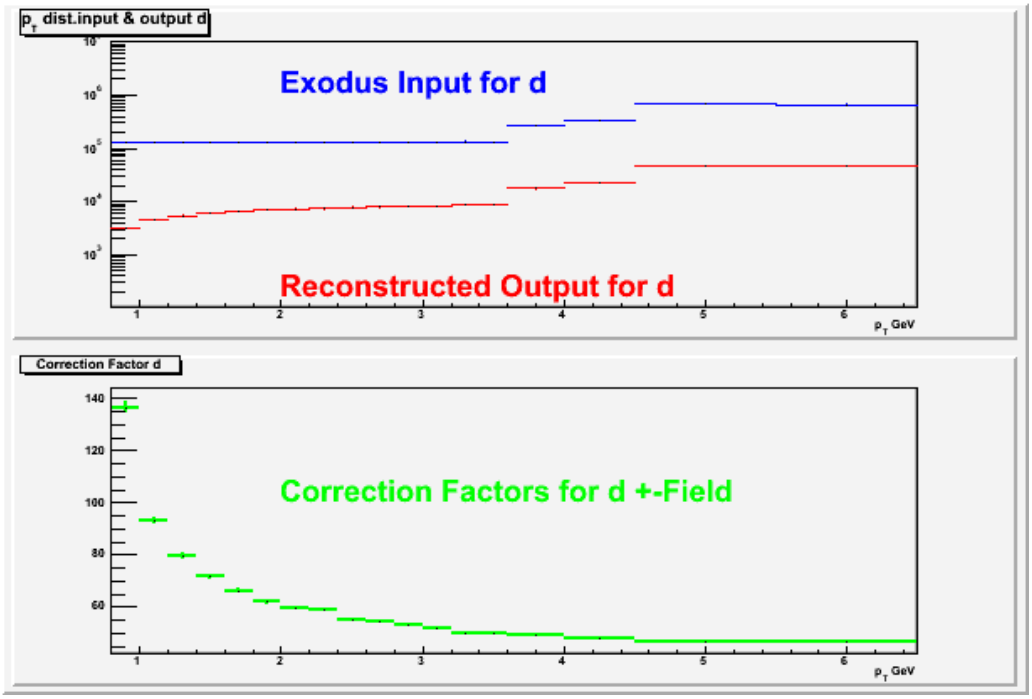

Figure 3.11: MC Correction Factor as a function of p_T for deuterons +- Field.

as shown on figures 3.11 and A.7 are obtained for each magnetic field configuration. The values of the bin-by-bin corrections are shown in Tables 3.5 and A.1 .

3.5 Tracking Efficiency

High multiplicity events generate very large numbers of tracks, and in such cases the reconstruction efficiency of the detectors is smaller due to increased occupancy. It is thus important to study the detector occupancy effects to correct for the loss in efficiency. For example, in a high multiplicity event, it is possible that two separate particles could hit the same strip in the TOF.W, resulting in only one readout and thus a loss in efficiency.

A commonly used approach to estimate occupancy effects is to “embed” single particle simulated events into real events with high multiplicity and then analyze the mixed data file

p_T GeV/c	Deuterons	Anti-deuterons
0.9	136.676 $\pm$ 2.45582	216.533 $\pm$ 4.87926
1.1	93.2842 $\pm$ 1.39145	137.774 $\pm$ 2.48832
1.3	79.6208 $\pm$ 1.10091	100.978 $\pm$ 1.56323
1.5	71.7997 $\pm$ 0.94688	89.0737 $\pm$ 1.30189
1.7	66.2906 $\pm$ 0.838792	81.2617 $\pm$ 1.13555
1.9	61.8892 $\pm$ 0.757641	74.6201 $\pm$ 0.997926
2.1	59.4974 $\pm$ 0.71581	70.8516 $\pm$ 0.926381
2.3	59.0239 $\pm$ 0.708561	67.813 $\pm$ 0.869109
2.5	55.1494 $\pm$ 0.640361	64.5935 $\pm$ 0.808395
2.7	54.5984 $\pm$ 0.632732	62.9222 $\pm$ 0.77863
2.9	53.1733 $\pm$ 0.607472	61.5617 $\pm$ 0.75230
3.1	52.0023 $\pm$ 0.5867	61.0953 $\pm$ 0.74453
3.3	50.1544 $\pm$ 0.555141	58.6923 $\pm$ 0.70022
3.5	49.617 $\pm$ 0.547894	58.6212 $\pm$ 0.7009
3.8	49.2955 $\pm$ 0.383901	57.6744 $\pm$ 0.482831
4.25	48.1396 $\pm$ 0.331613	56.6625 $\pm$ 0.421707
5	46.6812 $\pm$ 0.224066	55.3251 $\pm$ 0.28746

Table 3.5: Single Particle Monte Carlo Corrections for the +- Field.

using the same reconstruction cuts as used for the real data. Since full information about the simulated particle is available, one can estimate the reconstruction efficiency losses and then correct for those. At the time when this analysis was performed, the PHENIX embedding software was not operational so we applied an alternative method which is subject to somewhat larger systematic error than the embedding method. We assumed that the multiplicity dependent efficiency for this analysis can be factorize into tracking efficiency and TOF.W efficiency. We determined the loss efficiency in TOF.W from the data assuming 100% efficient tracking. We then applied tracking efficiency corrections which were obtained in a previous PHENIX analyse (from Run 2).

To implement this, we recorded the p_T distribution of tracks which pass through the

TOF.W fiducial area (see Appendix B) and register a hit in the pad chambers located in front and back of the TOF.W detector. Tracks with 3σ spacial matching hits in PC2 and PC3 were selected. We compare these distributions to the p_T distributions obtained when additional matching to TOF.W was requested. Some fraction varies with the centrality of the events as expected. No momentum dependence was observed in this process, so we applied a single multiplicative correction to the full p_T spectrum. This procedure takes into account multiplicity dependent efficiency loss in the TOF.W but it does not take into account the loss of tracking efficiency loss in the TOF.W. This tracking efficiency correction was separately applied (see Table 3.5).

Table 3.6: Efficiency correction factors for TOF.W.

centrality	**Efficiency**
Min. bias	0.748283 ± 0.05216
0 – 10%	0.677323 ± 0.07771
10 – 20%	0.725466 ± 0.09392
20 – 30%	0.768783 ± 0.07948
30 – 40%	0.810979 ± 0.05163
40 – 50%	0.849061 ± 0.03065
50 – 60%	0.889678 ± 0.01088
60 – 70%	0.918376 ± 0.02578
70 – 80%	0.940186 ± 0.05642
80 – 90%	0.949185 ± 0.13444
20 – 40%	0.78988 ± 0.06794
40 – 60%	0.86936 ± 0.00119
60 – 92%	0.93948 ± 0.05718

Since this method is not an embedding study itself, we compared this study with the tracking efficiencies obtained from Ref [47] and Ref [48] . The TOF.W was built with

similar granulation as TOF.E (i.e. in the design, the active area per track was estimated to be very similar to TOF.E). The main difference between the two detectors is the efficiency itself. In order to make a comparison to the TOF.E results, these numbers needed to be additionally corrected for the overall TOF.W efficiency of (90%). This "extra" correction allows to compared the numbers based on the same detector efficiency capacities.

The tracking correction as a function of p_T for different centrality classes is shown in Figures 3.12, A.8, A.9

3.6 Other Corrections

3.6.1 TOF.W ADC Cut

The ADC distribution for real data in the TOF.W is markedly different from that in the simulations. Because of this, the effects of the ADC cuts on real data were studied. After the analysis was finished, it was concluded that the optimal ADC range was from 60 to 600. The pedestal cut below 60 reduces background and noise, and the streamer cut at about 600 keeps the timing resolution as high as possible. The range used in this analysis represents 90% of the total ADC distribution, and is accounted for in the analysis code.

3.7 Comparison of Simulations and Real Data

When using simulations to correct the spectra, it is important to ensure that an "apples to apples" comparison is being made. If there are any differences between the simulated detector response and the actual detector response, these differences need to be accounted for accordingly. As an example, the next section describes the differences between simulation

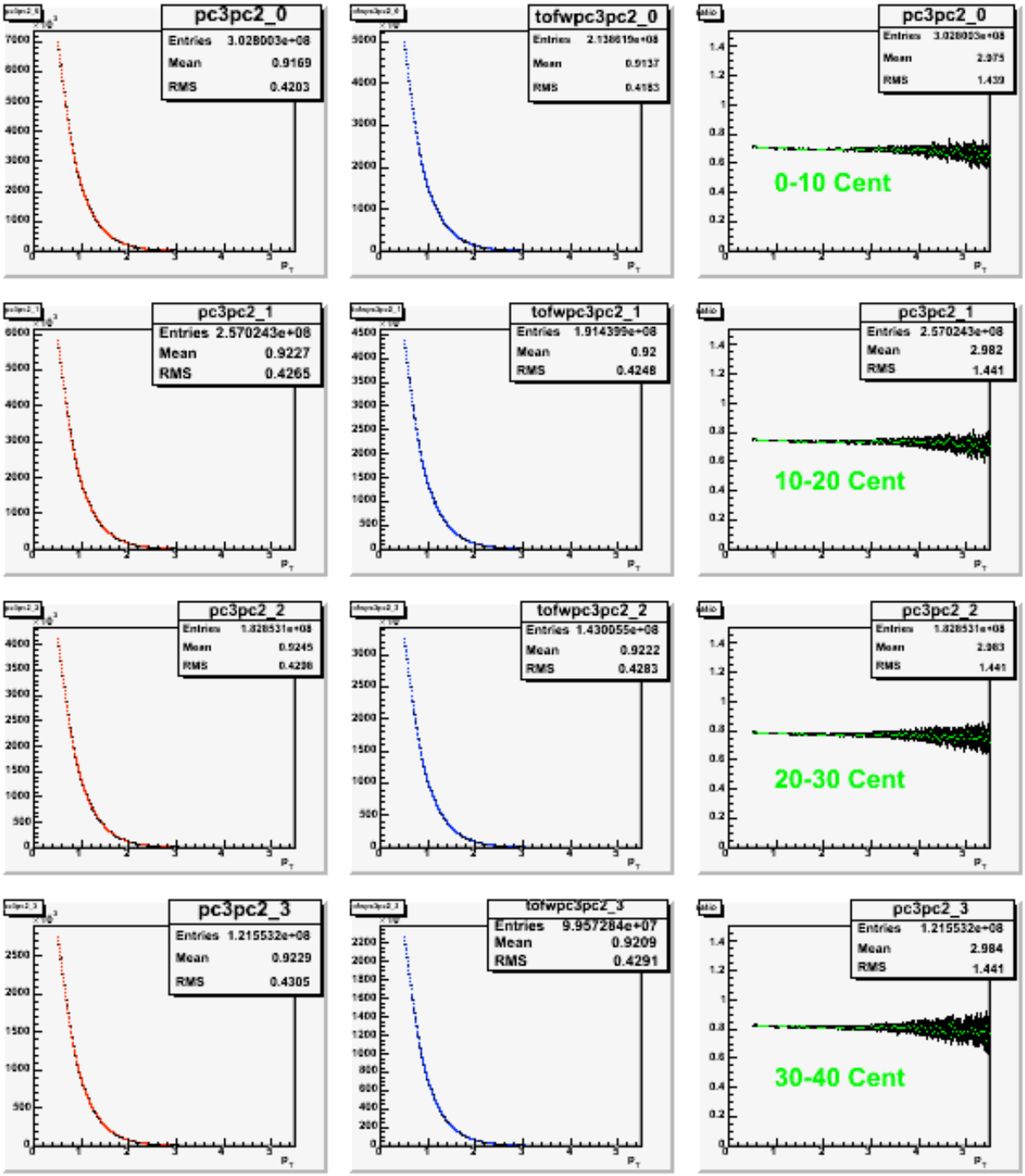

Figure 3.12: PC2-PC3 matching histogram (left panel), PC2-PC3-TOF.W matching histograms (middle panel), and the corresponding correction factor (right panel) for 0-10%, 10-20% 20-30%, and 30-40% centrality bins.

and real data for the TOF.W. For more details regarding our matching cuts ($TOF.W_{\sigma d\phi}$, $TOF.W_{\sigma dz}$, $PC3_{\sigma d\phi}$, $PC3_{\sigma dz}$), and for some comparison for acceptances between data and simulation, please refer to Appendix B.

3.8 Hadronic Absorption of d and $\bar{d}$

3.8.1 Hadronic Absorption

To obtain the acceptance and efficiency corrections for deuterons and anti-deuterons, we used PISA simulations. (Anti-)deuterons in PISA can only be observed with electromagnetic interactions, since hadronic processes for nuclei are not implemented in GEANT [c]. Calculating the hadronic absorption effect is necessary for the correction of our data.

To get an estimate of the nuclear interactions we performed a PISA simulation for protons and anti-protons with and without hadronic interactions. In addition, we estimated the proton and anti-proton absorption based on our knowledge of the material in the detector (implemented in PISA) and a parameterization of the interaction cross-section. The results from the two methods were compared and were found to be in reasonable agreement, as discussed below. For deuterons and anti-deuterons only the stand-alone calculation is possible and we extracted corrections on the basis of this calculation. It is used as inputs to a cross section parameterization (see Appendix C), and the detector material is extracted from PISA.

[c] GEANT (for GEometry ANd Tracking), is a software toolkits platform for "the simulation of the passage of particles through matter"

3.8.2 PISA Simulation for Protons and Anti-protons

Protons and anti-protons were generated with the following specifications:

- a flat distribution in the range -0.35 $<$ y $<$ +0.35
- $0.25 < p_T < 2.5$
- -40.0 $< \phi <$ +62.50 in degrees, which is 6.25 degrees more on each end of the west arm. (The EXODUS input azimuth range in radian is -0.6981317 to +1.090831)
- Z_{vertex} = 0

The input files were processed through PISA with hadronic interaction turned ON and OFF. The same input events were used in both events[d]. The TOF.W detector consist of two "sections", located in two areas of the west arm, and for this reason, the survival probability was calculated separately for each section and then combined. The results are about 3% different from each other, so that for the final PISA survival probability for TOF.W, we weighted the two numbers with the following formula

$$\bar{S} = \frac{n_1 S_1}{n_1 + n_2} + \frac{n_2 S_2}{n_1 + n_2} \tag{3.10}$$

where n_1 is the number of hits in the top sector, n_2 is the hits in the bottom sector, and S_1 and S_2 are the survival probabilities of top and bottom sections respectively. The results from our PISA calculations are given in Table 3.7 and A.4 for protons and anti-protons respectively.

[d]Protons and anti-protons are no-primary particles by definition, as long as they interact either elastically or inelastically. There is, as far as we know, no simple way to tell whether a hadronic interaction in GEANT (for the version used in this analysis) was elastic or inelastic

Table 3.7: Hadronic survival probability calculation with PISA for protons.

p_T GeV/c	Ratio(Hadronic ON/Hadronic OFF)
0.50-0.75	89.9317 $\pm$ 3.9598
0.75-1.00	90.4984 $\pm$ 1.84061
1.00-1.25	90.2014 $\pm$ 1.31932
1.25-1.50	89.1776 $\pm$1.1493
1.50-1.75	89.2637 $\pm$1.05014
1.75-2.00	89.2179 $\pm$0.996658
2.00-2.25	89.1231 $\pm$0.956603
2.25-2.50	89.2705 $\pm$1.16701

3.8.3 Stand-Alone Calculations

Since hadronic processes for nuclei are not implemented in our GEANT version, we have performed stand-alone calculations. The material in the west arm is extracted from PISA. For this purpose, a small run using "geantinos" was performed. A total of 1000 geantinos were generated originating from Z_{vertex} = 0 and hitting the TOF.W uniformly. The tracking media transversed by the geantinos and the average distance through each medium are given in Appendix C.2.

The material as calculated is fed into the stand-alone program together with energy-dependent inelastic cross-sections for protons, anti-protons, deuterons, and anti-deuterons. The cross section parameterization is discussed in Appendix C.

The survival probability is calculated from

$$exp(-\sum \sigma_i n_i l_i) \tag{3.11}$$

where n_i and l_i are the number density and thickness of material i, respectively. The

Table 3.8: Hadronic survival probability, stand-alone calculation for (anti)-protons.

p_T GeV/c	protons[%]	anti-protons[%]
0.50-0.75	92.3559	89.9258
0.75-1.00	92.3478	90.0223
1.00-1.25	92.3401	90.1637
1.25-1.50	92.3361	90.3064
1.50-1.75	92.3344	90.4348
1.75-2.00	92.3338	90.5513
2.00-2.25	92.3336	90.652
2.25-2.50	92.3335	90.7409

materials are broken down to elements in the same way as in PISA (see Appendix C.2).

Using the the above equation, we obtain our stand-alone calculation for proton, anti-protons (Table 3.8), deuterons, and anti-deuterons (Table A.5). For these calculations, the top and bottom TOF.W sector hadronic survival probabilities were computed separately, then we averaged the numbers to obtain for the final results.

If we compare these values with the values obtained from PISA, we see that the probabilities in this case are slightly larger than in PISA. This is due to the different cross sections being used (inelastic vs. total). Furthermore, the p_T in both cases is similar.

3.9 Discussion of Systematic Error Estimation

Our systematic errors fall into two categories: errors that vary point to point as a function of p_T, and errors that are constant.

3.9.1 Errors that Vary Point to Point as a Function of p_T

Most errors fall in this category and include matching, PID errors, etc. We calculate the p_T dependent errors by varying our cuts to generate spectra and then look at the difference between the new yields and the final yields. The combined point to point value of these systematic errors is listed in Tables 3.9, A.6, A.7

The source of each systematic uncertainty is explained below:

- **Matching Cuts Systematics**: As discussed before, to select high-quality tracks and reduce background we make cuts on the residual distributions (in ϕ and z) between the track projection on the TOF.W and PC3 and the hit position as recorded in these detectors. These cuts are made as a function on p_T in terms of a fixed number of σ which is the Gaussian width of the corresponding residual distribution. The same cuts are performed in simulations and thus corrections are obtained for the cut fractions. However, it is possible that the distributions are not simply Gaussian and that the fraction of real tracks included in the cut for real data deviates from a Gaussian estimate by some amount. To estimate the systematic uncertainty associated with this we increase the matching cut from 2.0σ to 2.5σ for TOF.W and PC3 (for both real and simulation data) and then calculate the corrected spectra with the two difference cut conditions. This ratio represents the systematic error due to the cut in consideration. The ratio of the two spectra is shown in Figure A.10.

- **PID Systematics**: To extract the deuteron yield we fit the mass-squared distribution with a Gaussian function for the signal and an exponential for the background. It is possible that the shape of the background distribution is different and thus the relative

Table 3.9: p_T dependent absolute systematic errors from different sources, added in quadrature for 0-10% and 10-20% at the mean of the p_T bin for all centrality classes.

Centrality	p_T GeV/c	deuterons	anti-deuterons
0-10%	1.10086	0.000786038	0.000244821
	1.30029	0.000546962	0.000111733
	1.49971	0.000291396	0.000128076
	1.69914	0.000194325	9.655e-05
	1.89857	0.000138452	9.86288e-05
	2.09799	0.000104937	6.5263e-05
	2.29742	7.29394e-05	8.52289e-05
	2.49685	5.40648e-05	3.2297e-05
	2.69628	5.30844e-05	2.7397e-05
	2.8957	2.47212e-05	2.59758e-05
	3.09513	2.12197e-05	1.18379e-05
	3.29456	1.00362e-05	1.18808e-05
	3.49399	1.18683e-05	5.50626e-06
	3.77288	3.61545e-06	3.4505e-06
	4.20045	3.10408e-06	2.3724e-06
	4.78034	6.19236e-07	6.77302e-07
10-20%	1.10086	0.000841671	0.000461822
	1.30029	0.000796446	0.00023534
	1.49971	0.000581502	0.000221921
	1.69914	0.000450729	0.0002277
	1.89857	0.000355338	0.000156647
	2.09799	0.000273004	0.000123264
	2.29742	0.000191668	0.000184361
	2.49685	0.000132975	7.53226e-05
	2.69628	9.33811e-05	5.43933e-05
	2.8957	5.49037e-05	3.34259e-05
	3.09513	4.13994e-05	3.60342e-05
	3.29456	3.09107e-05	1.48563e-05
	3.49399	1.4e-05	9.65546e-06
	3.77288	6.08761e-06	3.72723e-06
	4.20045	2.48723e-06	1.41539e-06
	4.78034	7.93546e-07	9.14713e-07

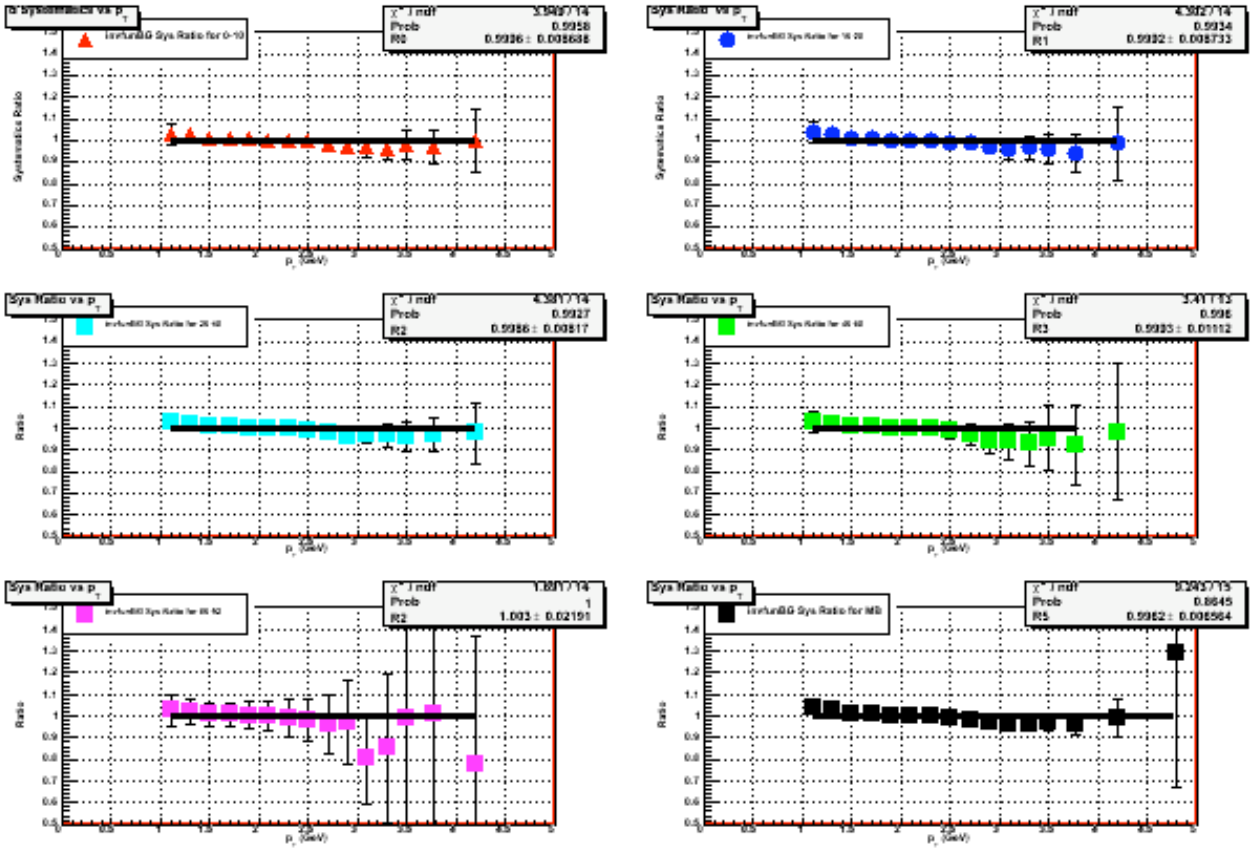

Figure 3.13: Systematic error estimate for PID using different background fit. Plotted in the six panels show the ratio of the two background fits used for the six centrality bins.

contribution of the signal in the mass-squared histogram is different. To estimate the systematic error in the yield extraction we compare the yields extracted from two different functional forms ($1/x$ and e^{-x} for the background). The ratio of the two number is shown in Figure 3.13

- **ADC Systematics**: In order to study the influence of the ADC cut, the ADC window, both on the low and high ends, was increased. Our "master" cut is 60<ADC<600,

and another cut of 40<ADC<800 [e] was used. The results of the two spectra is shown in Figure A.11

- **Magnetic Field Systematics**: For the -+Field, we created two new simulation projects based on this field and repeated all the previous steps to extract the particle yields. We found this error to be less than 0.5%. The ratio of the corrected spectra for both magnetic fields is shown in Figure A.12

3.9.2 Errors that are Constant as a Function of p_T

The errors in this category include tracking efficiency, annihilation/hadronic interaction corrections, and feed down correction (for proton yields). These systematic errors are summarized in Table 3.9.2

Table 3.10: p_T independent systematic errors form different sources.

centrality	Annihilation d(d)	Tracking
Min. bias	1.2% (3.7%)	74.82%
0 – 10%	1.2% (3.7%)	67.73%
10 – 20%	1.2% (3.7%)	72.54%
20 – 40%	1.2% (3.7%)	78.98%
40 – 60%	1.2% (3.7%)	86.93%
60 – 92%	1.2% (3.7%)	93.94%

- **Annihilation Correction Systematic**: The systematic error due to the survival probability (annihilation) correction for deuterons are 1.2% and 3.7% for anti-deuterons

[e] opening the ADC window will bring more BG into play

(see Section 3.8.1).

- **Tracking Efficiency Systematics**: Tracking efficiency error results as described in Section 3.5 are tabulated in Table 3.5. These results are constant as a function of p_T.

3.9.3 Proton Yield Systematic Error for Coalescence Parameter

When calculating systematic error for the coalescence parameter, an additional error based on the proton yields needs to be included. This error is estimated to be 10.2%, as detailed in [47, 48].

3.9.4 Summary of Systematic Error Study

The following table summarizes our yield systematic error study in percent error (%).

Table 3.11: Summary of systematic error.

centrality	Matching	BG Fit	ADC Cut	Mag. Field	Annihilation d($\bar{d}$)	Tracking
0 – 10%	1.9%	0.04%	2.9%	0.4%	1.2% (3.7%)	67.73%
10 – 20%	1.4%	0.08%	2.7%	1.8%	1.2% (3.7%)	72.54%
20 – 40%	1.1%	0.14%	2.7%	2.4%	1.2% (3.7%)	78.98%
40 – 60%	2.6%	0.07%	2.5%	2.7%	1.2% (3.7%)	86.93%
60 – 92%	6.7%	3.0%	3.8%	3.7%	1.2% (3.7%)	93.94%
Min. bias	1.4%	0.38%	2.7%	1.8%	1.2% (3.7%)	74.82%

For the systematic error calculations due to survival probability and matching, please refer to Section 3.9.2

CHAPTER IV

EXPERIMENTAL RESULTS AND DISCUSSION

The hadrons produced in the collision zone carry information about the nature of the collision, as well information on its size and composition. In particular, the p_T behavior of the spectra can yield information about the dynamics of the collision, while the particle yields and abundances can help us to determine the temperature and the baryon chemical potential. In this chapter, the transverse momentum spectra and yields of identified deuterons and anti-deuterons at mid-rapidity in $Au+Au$ collisions at $\sqrt{s_{NN}} = 200$ GeV are presented. Using the spectra results, particle to antiparticle ratios for all centrality classes as well as nuclear modification factors are obtained. The transverse momentum spectra are fit with a hydro-dynamics inspired model to obtain the freeze-out temperature and the common flow velocity of the QCD matter produced in the collisions. The deuterons, being much heavier than the commonly produced pions have greater sensitivity to the radial flow. They are also uniquely sensitive to the assumption about the shape of the source and the emission time duration, since they are composite particles. We also determine the proton-neutron the coalescence parameter (B_2) which is related to the source volume and study its evolution as a function of centrality and p_T.

4.1 Spectra and Yields

After applying the corrections discussed in section 3.4 and 3.9, we obtain the deuteron and anti-deuteron invariant yields as a function of p_T in the momentum range $1.1 < p_T < 5.5$ GeV/c. We divided the spectra into 6 different centrality classes:

- 0-10% centrality (most central collisions)
- 10-20% centrality
- 20-40% centrality
- 40-60% centrality
- 60-92% centrality (most peripheral collisions)
- 0-92% centrality, usually referred to as minimum bias

Figure 4.1 shows the deuterons (left) and anti-deuterons (right) p_T distributions for all centrality classes. The same data is also plotted as a function of transverse mass, m_T, in Figure 4.2. For a thermal spectrum, one expects an exponential distribution in m_T. Radial flow changes the slope of the spectrum, but it may still remain exponential, if the flow is not very strong. For the first time at RHIC we have observed radial flow that is strong enough to produce significant deviation from purely exponential m_T distributions. These deviations are most pronounced for the central collisions (black points) where the flow is strongest. After all corrections, the final corrected deuterons yield are given by Table A.8, A.9, and A.10

As seen in Figure 4.3, all the m_T spectra display an exponential shape in the low m_T region, and a visible change in slope with the particle mass. In this plot, one can naively

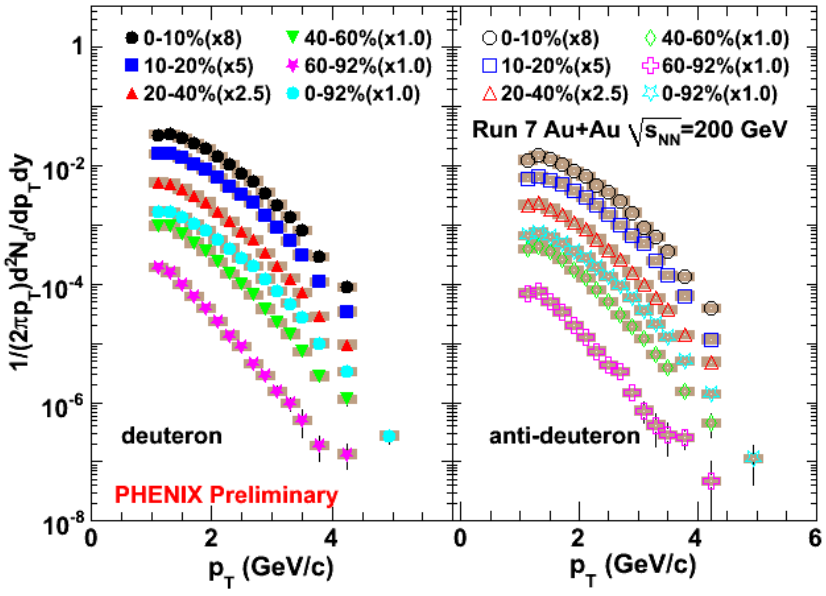

Figure 4.1: Corrected deuteron yields (left) and anti-deuteron yields (right) vs p_T for all centrality classes. Shaded bands represent systematic error.

expect that the slope of deuterons, being heavier particles, would be the same as that of protons (because deuterons are made of protons and neutrons), but this is not exactly the case. There is information about the source size that one can eventually extract from a more detailed analysis.

4.2 dN/dy and $< p_T >$

It is often convenient to characterize the shape of the spectra by one number. If the m_T spectra are exponential, then a good measure of the shape is the slope, which is inversely proportional to the temperature of the source at freeze-out. However, with the strong radial flow, the spectra are no longer exponential. The slope depends on the p_T or the m_T range of the fit. Its value is affected by both the temperature and the radial flow veloc-

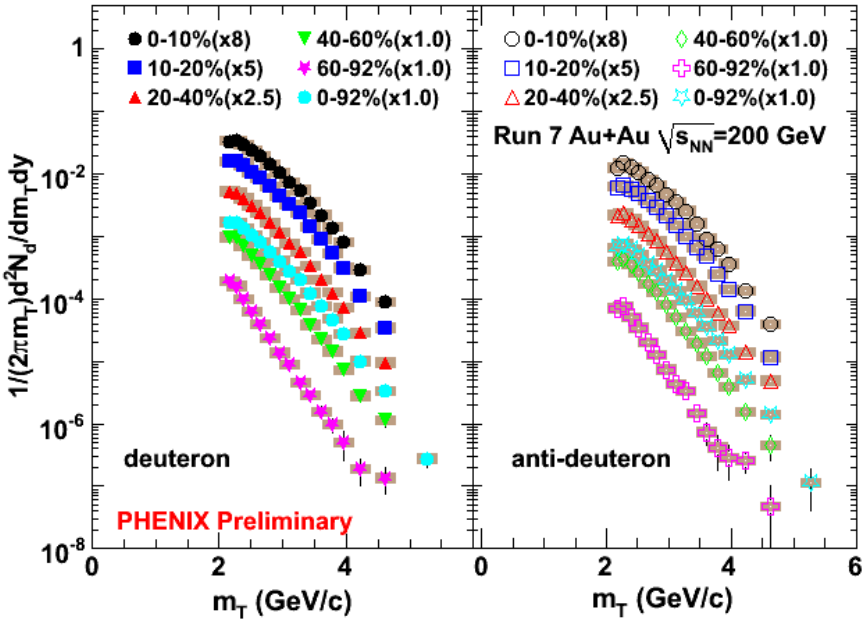

Figure 4.2: Corrected deuteron (left) yields and anti-deuterons (fight) yields vs m_T for all centrality classes. Shaded bands represent systematic error.

ity. At asymptotically high p_T or m_T, when the mass of the particle is small compared to its momentum, the slopes of all spectra become the same and are given by $T_{slope} = T_{freeze-out}\sqrt{(1+\beta)/(1-\beta)}$ which is a thermal spectrum "blue-shifted" by the flow. To describe the spectra and facilitate an easy comparison between different particle species, centrality classes, experimental systems, etc., we study the behavior of the mean transverse momentum.

Similar tools are used to extract the total yield per unit rapidity. This number is important, because it provides additional information about the thermal properties of the system. For example, particle yields and ratios are used to determine the chemical potentials in the system and they are compared to thermal models of particle production to test the equilibration in the produced QCD matter. By integrating a measured p_T spectrum over, one

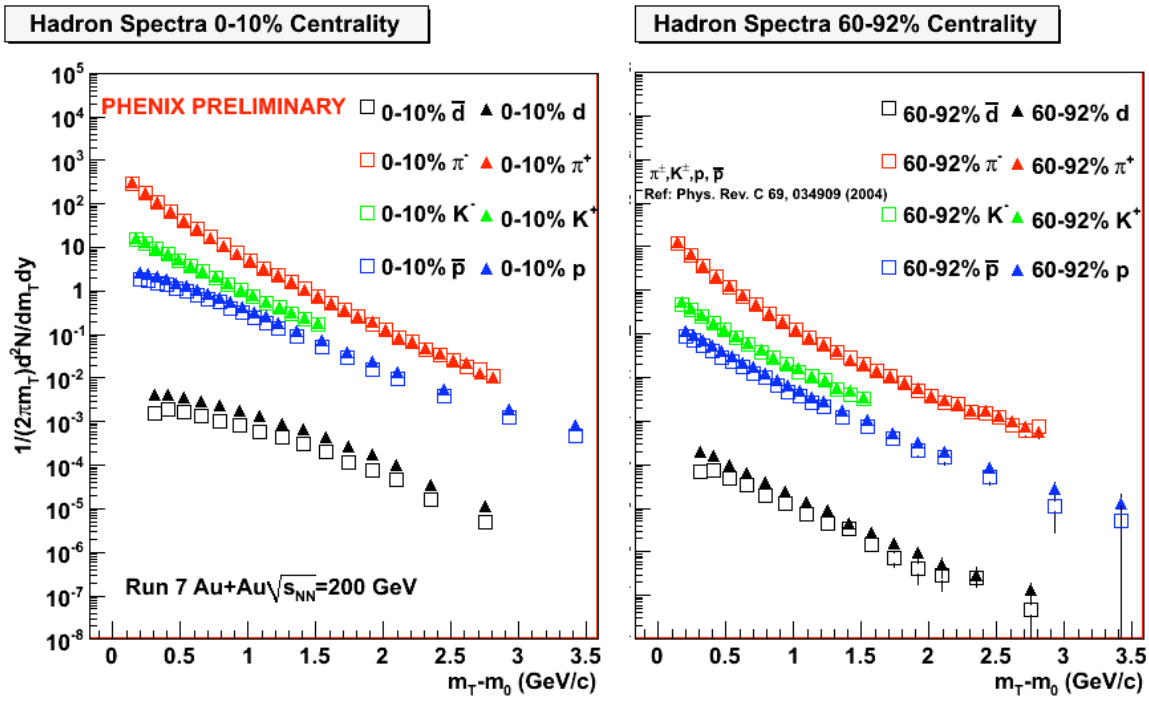

Figure 4.3: Transverse mass distribution for $\pi^{\pm}$, $K^{\pm}$, protons, anti-protons, deuterons, and anti-deuterons for central 0-10%(left) and peripheral 60-92% (right) in $Au + Au$ collisions at $\sqrt{s_{NN}}$ = 200 GeV. The error bars are statistical error only.

can determine the mean transverse momentum, $\langle p_T \rangle$, and particle yield per unit rapidity, dN/dy for each particle type. The dN/dy was calculated as follows:

$$\frac{dN_d}{dy} = \int_0^{10} 2\pi p_T f(p_T) dp_T \tag{4.1}$$

where f (p_T) is the function that gives us the invariant yield as a function of p_T:

$$\frac{d^2N_d}{2\pi p_T dy} = f(p_T) \tag{4.2}$$

In order to minimize our errors, we substituted this integral into three regions:

1. The lower p_T region is in the range from 0 to 1.0 GeV. This limit correspond to the lowest point of our experimental data. Here, we have extrapolated a function to predict the yield in the low p_T region. For the extrapolation function, we used a Boltzmann distribution (see Figures 4.4 and Figure A.17) of the form:

$$\frac{d^2n}{2\pi m_T dm_T dy} = Am_T e^{\pm m_T/T_{eff}} \tag{4.3}$$

2. The second region is our actual experimental measurement of the data. Here, we have numerically integrated our data in the region from 1.0 to 5.5 GeV in p_T and propagated the statistical error accordingly.

3. The third and final integral range, consist of the high p_T region. Here, once again, we have used a function (same as in region one) for extrapolation. We have integrated from 5.5 to ∞ in p_T.

4.2.1 Systematic Error for dN/dy and $< p_T >$

It should be noted that the data constitutes approximately 62% for deuterons and 65% for anti-deuterons of the total extrapolated yields. The systematic error on dN/dy and $\langle p_T \rangle$ was estimated using three different functional forms.

1. A truncated Boltzmann in which we assume a flat distribution for $p_T < 1.1$ GeV. The truncated Boltzmann fits are shown in Figures 4.5, A.18, A.19, A.20, A.21, and A.22.

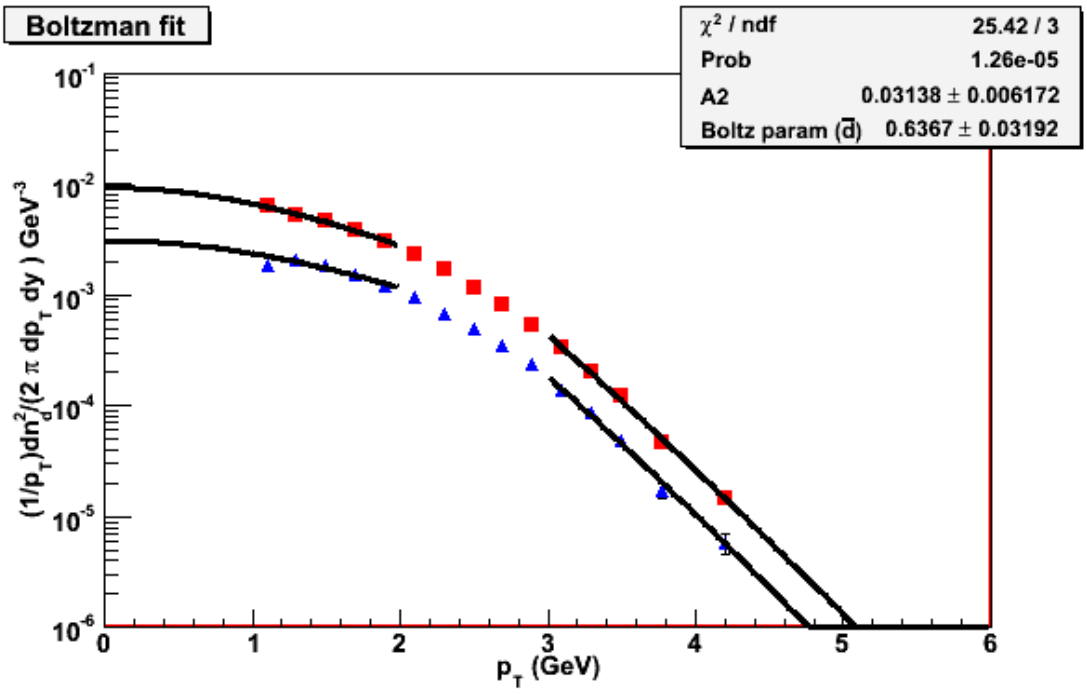

Figure 4.4: dN/dy using Boltzmann ratio 0-10% centrality.

2. p_T exponential fit of the form:

$$\frac{d^2n}{2\pi m_T dm_T dy} = Ae^{p_T/T_{const}} \tag{4.4}$$

The p_T exponential fits are shown in Figures 4.6, A.23, A.24, A.25, A.26, and A.27.

3. The last fit we used is a Gaussian fit for the low p_T region. The Gaussian fits are shown in Figures 4.7, A.28, A.29, A.30, A.31, and A.32.

After a carefully examination of all the fits results, we concluded that a combination of the different systematic errors would be used to estimate the overall systematic error. The high limit for our systematic error will be dictated by Gaussian fit results, while the low

limit comes from our exponential fit results. [a]

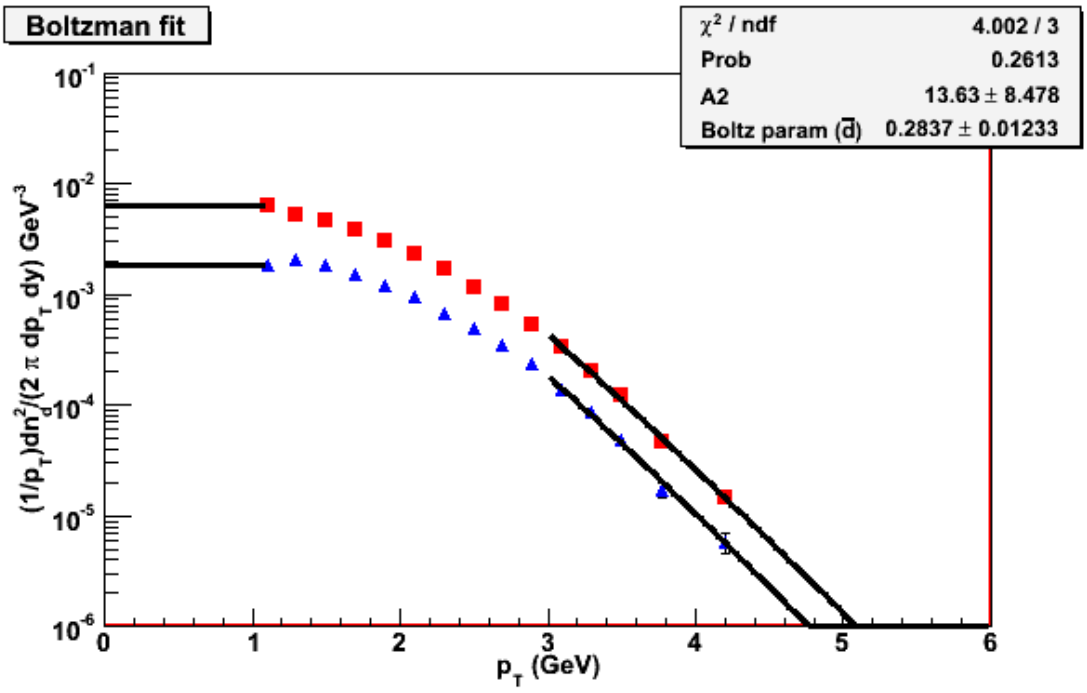

Figure 4.5: dN/dy using Boltzmann "flat" ratio 0-10% centrality.

4.2.2 Average Transverse Momentum $< p_T >$

To calculate the average p_T ($\langle p_T \rangle$) of the spectra, we followed a similar method as above, with the $\langle p_T \rangle$ defined as the ratio of the integrals:

$$\langle p_T \rangle = \frac{\int_0^\infty p_T^2 f(p_T) dp_T}{\int_0^\infty p_T f(p_T) dp_T} \tag{4.5}$$

[a] The Gaussian fit resulted in a $< 2\%$ systematic error for the 60-92% centrality for the deuteron spectrum and $\sim$10% error for the anti-deuteron. The error on the deuterons seems unrealistically small and thus we for this centrality only, we assigned the same systematic error as we got from the Gaussian fit for the anti-deuteron.

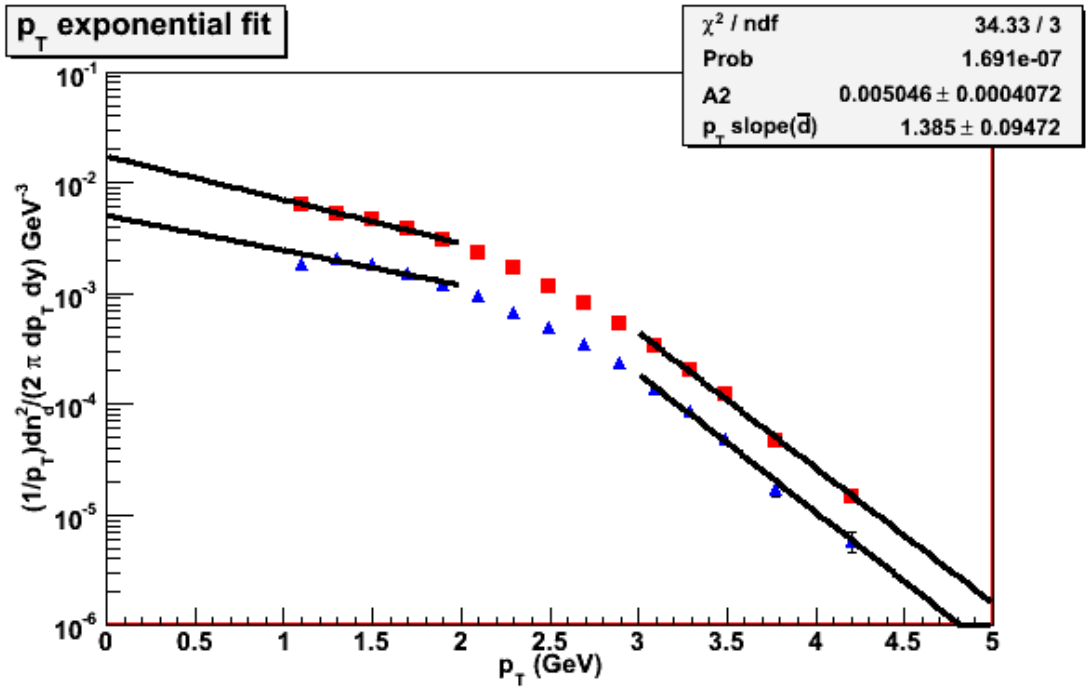

Figure 4.6: dN/dy using exponential fit for 0-10% centrality.

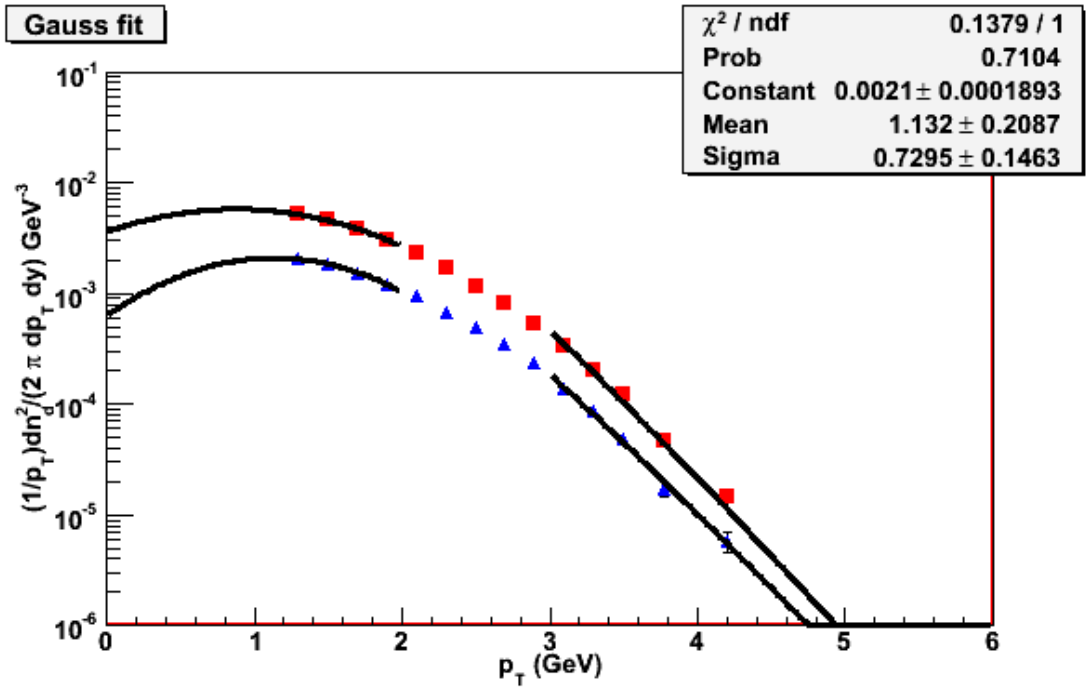

Figure 4.7: dN/dy using Gaussian fit for 0-10% centrality.

Table 4.1: $\langle p_T \rangle$ values for different centrality classes.

Centrality	Deuterons $\langle p_T \rangle$	Anti-deuterons $\langle p_T \rangle$
0-10	$1.4182 \pm 0.00747(\text{stat}) \pm^{0.1051(sysHigh)}_{0.0795(sysLow)}$	$1.4773 \pm 0.0114(\text{stat}) \pm^{0.1787(sysHigh)}_{0.0806(sysLow)}$
10-20	$1.3801 \pm 0.00717(\text{stat}) \pm^{0.0864(sysHigh)}_{0.0918(sysLow)}$	$1.4372 \pm 0.01067(\text{stat}) \pm^{0.2384(sysHigh)}_{0.0795(sysLow)}$
20-40	$1.2923 \pm 0.00609(\text{stat}) \pm^{0.1259(sysHigh)}_{0.1070(sysLow)}$	$1.3490 \pm 0.00875(\text{stat}) \pm^{0.1771(sysHigh)}_{0.0986(sysLow)}$
40-60	$1.1611 \pm 0.00683(\text{stat}) \pm^{0.0622(sysHigh)}_{0.1435(sysLow)}$	$1.2236 \pm 0.01047(\text{stat}) \pm^{0.2034(sysHigh)}_{0.1296(sysLow)}$
60-92	$0.9676 \pm 0.00946(\text{stat}) \pm^{0.1086(sysHigh)}_{0.1913(sysLow)}$	$1.0501 \pm 0.01672(\text{stat}) \pm^{0.1085(sysHigh)}_{0.1692(sysLow)}$

The $\langle p_T \rangle$ values obtained from the above procedures are recorded in Table 4.1.

In Figure 4.8 the centrality dependence of $\langle p_T \rangle$ for d and $\bar{d}$ along with data from pions, kaons, and protons(Ref. [1]) is shown. The systematic error from cut conditions are shown as shaded boxes on the right for each particle species. It is found that $\langle p_T \rangle$ increases from the most peripheral to mid-central collisions and appears to saturate from mid-central to central collisions for pions and kaons. On the other hand, the $\langle p_T \rangle$ values for p, $\bar{p}$, d, and $\bar{d}$ continue to rise as a function of N_{part}. One of the main sources of the uncertainty is the yield extrapolation in the unmeasured p_T range (e.g $p_T < 1.0$ GeV for deuterons and anti-deuterons).

Figure 4.9 shows the centrality dependence of dN/dy per participant pair ($0.5N_{part}$). Once again, we plotted our deuteron results with previously published spectra results from $\pi^{\pm}$, $K^{\pm}$, protons, anti-protons [1]. Here, the data indicates that dN/dy participant pair increases up to ≈ 100 and saturates from mid-central to the most central collisions.

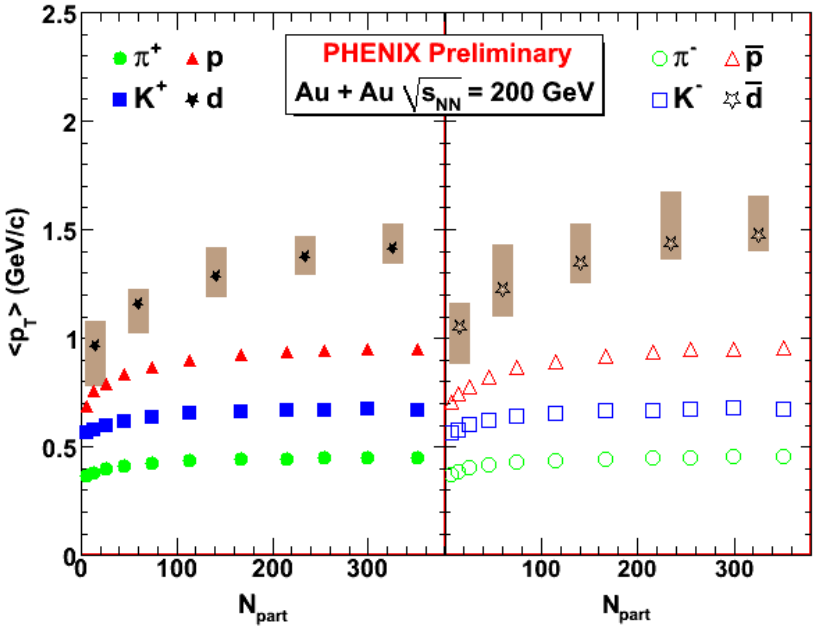

Figure 4.8: Mean transverse momentum as a function of N_{part} for pions, kaons, protons, anti-protons, deuterons, and deuterons.

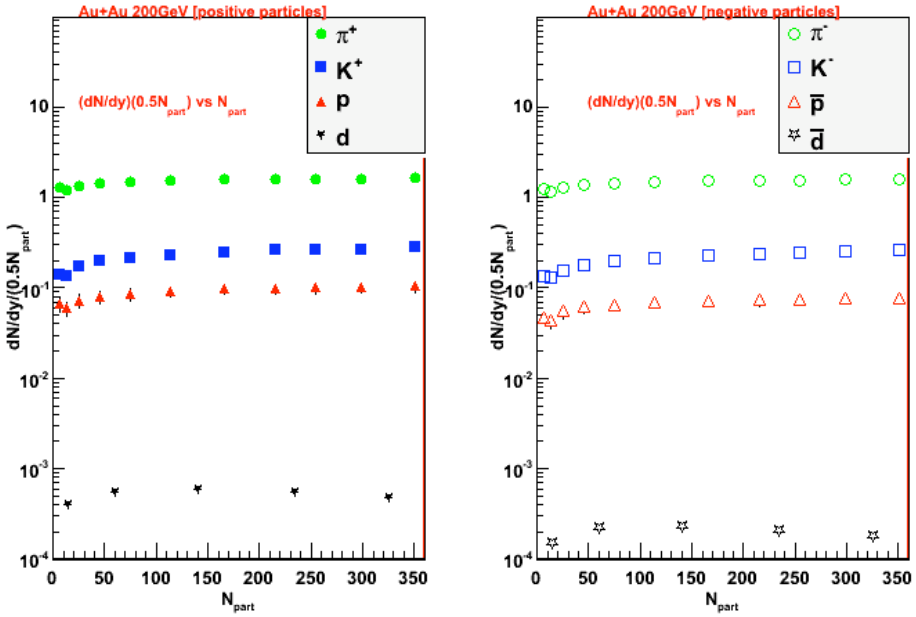

Figure 4.9: Particle yield per unit rapidity (dN/dy) per participant pair ($0.5N_{part}$) as a function of N_{part} for pions, kaons, protons, anti-protons [1], deuterons, and deuterons.

4.2.3 Comparison to Previous Published Results

In this section, we compare our results with previous PHENIX published results [48]. In the previous publication, due to the low statistics of Run2, results were presented for only three centrality classes (0-20%, 20-92%, and minimum bias) . In figures: 4.10, and 4.11, we compare our results within the same centralities of those published in [48]. For centrality 0-20% (Figure 4.10), we also plotted STAR data [49] at $\sqrt{s_{NN}} = 130$ GeV measured for the 0-18% centrality class. One can see from the figures that our results agree with those of [48] results within statistical and systematic errors.

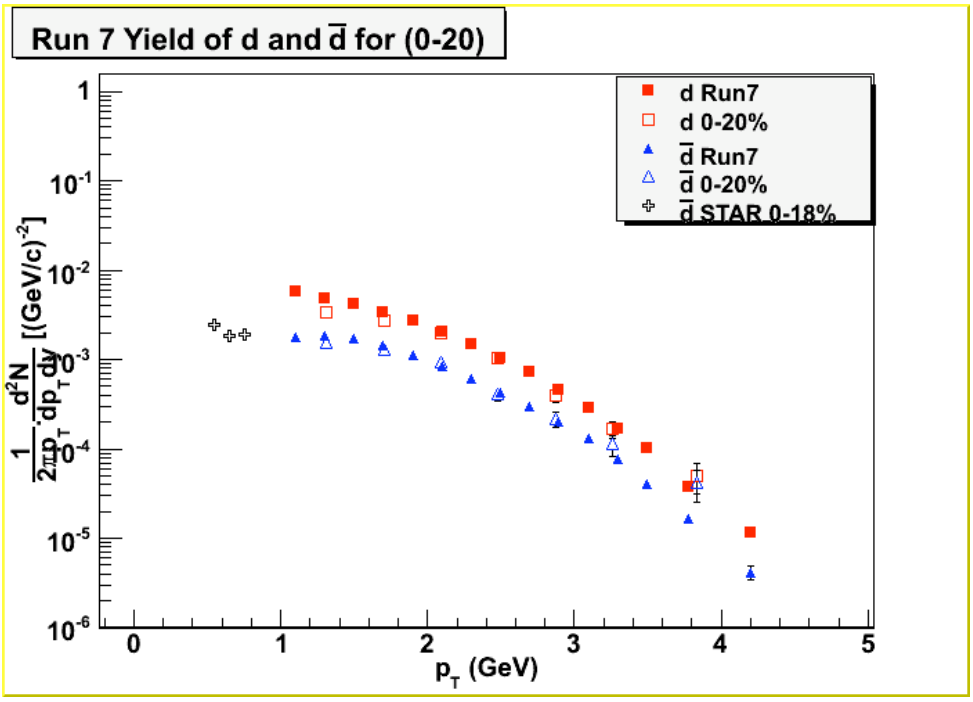

Figure 4.10: (Anti-)Deuteron spectra for 0-20% centrality with Reference [48] points, and STAR data [49].

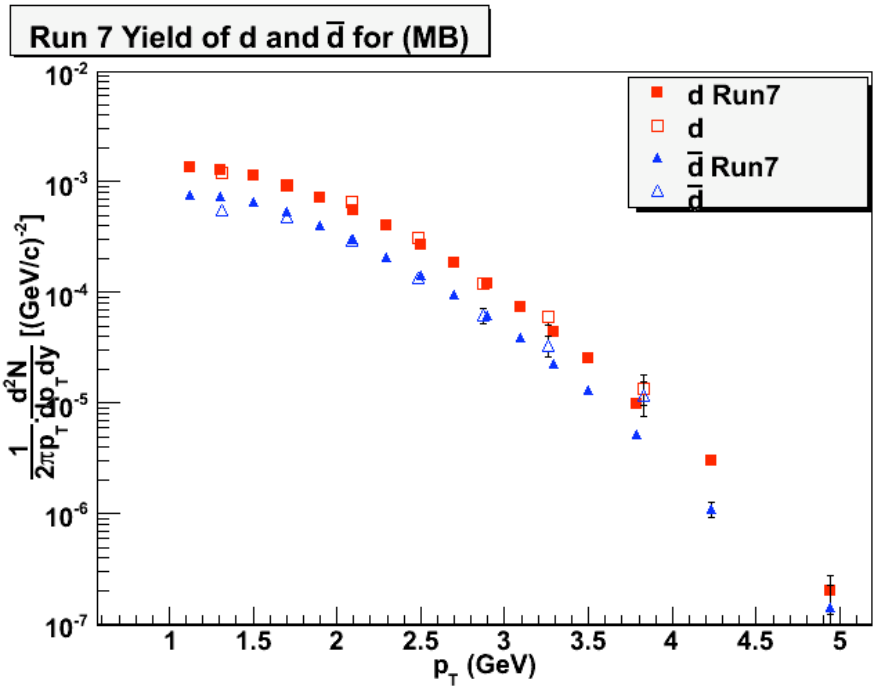

Figure 4.11: Minimum Bias (Anti-)Deuteron spectra from Run 7 compared with Reference [48] points.

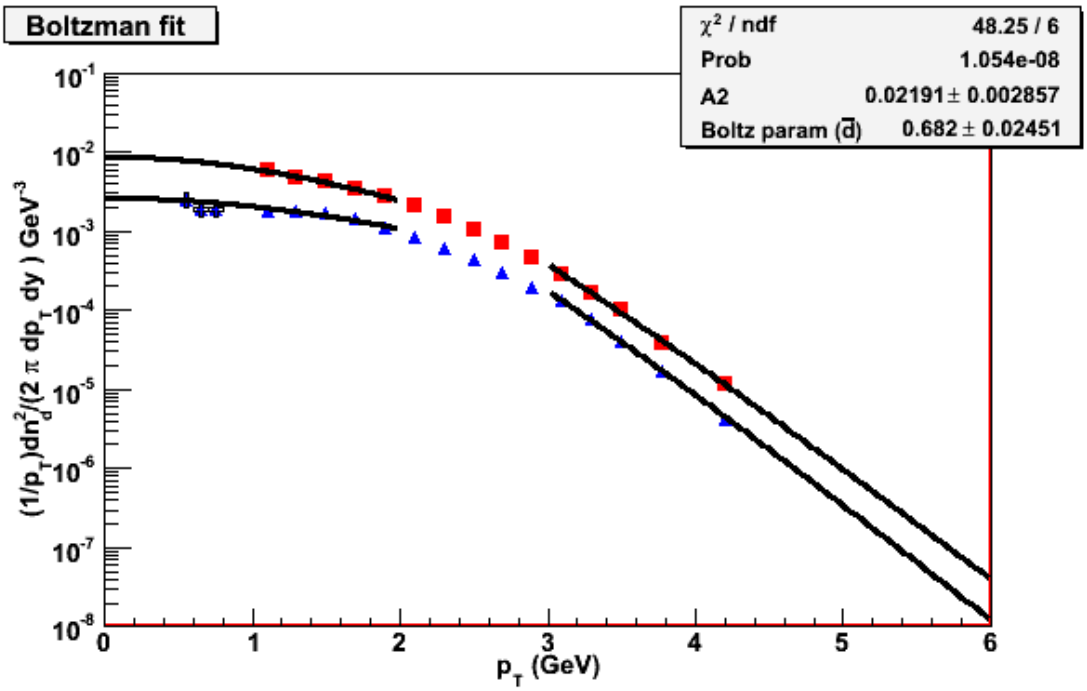

Figure 4.12: dN/dy using the Boltzmann distribution fit for 0-20% centrality compared with 3 points for $\bar{d}$ from STAR. STAR points are from 130 GeV Au+Au Collisions and at 18% centrality.

4.3 Radial Flow Study

Identified hadron spectroscopy is an important tool for studying collision dynamics. The momentum spectra of hadrons are sensitive to the dynamical evolution of the system and carry information about the radial flow velocity and thermal freeze-out conditions. Due to an overall very good qualitative agreement between radial flow considerations and the experimental results seen so far, it is interesting to check for qualitative agreement with a hydrodynamic model. In a hydrodynamical model, the radial flow velocity (β_T) and freeze-out temperature (T_{fo}) are extracted by a "blastwave" fit to the p_T spectra.

4.3.1 Blast-Wave Model Parameterization

The radial flow velocity (β_T) and freeze-out temperature (T_{fo}) are extracted using a phenomenological hydrodynamical model presented in Ref [50]. Here we consider a very simple "blastwave" model, which can be summarized by the following relation determining the momentum spectra for various particles:

$$\frac{1}{p_T}\frac{dN}{dp_T} = A\int_0^1 dx f(x) x m_T K_1(\frac{m_T \cosh\rho}{T_{fo}}) I_0(\frac{p_T \sinh\rho}{T_{fo}}), \tag{4.6}$$

where I_0, K_1 represent modified Bessel functions, $x = r/R$ measures the position along the radial direction of the source, and $\rho = \tanh^{-1}(\beta_T r/R)$ is the transverse boost which depends on the radial position and the transverse flow velocity β_T measured at the freeze-out surface. The normalization constant A is a free parameter but it does not affect the spectral shapes.

We fit the above formula for a fixed pair of β_T and T_{fo}. We scan a grid of possible

values for the two parameters and record the χ^2 for each fit. Next, we use a minimization procedure to get the best χ^2 from all values we obtained from the grid (see Figure 4.14). This is done for either one particle or for several particles simultaneously. The contour plots (see Figure 4.13) give the standard deviation from the determined minimum χ^2

This equation considers all particles produced in all stages of the fireball evolution. However, as prescribed in [27], one can make certain adjustments to account for the nature of cluster particles, such as deuterons. The quantum mechanical corrections affect only the normalization constant A and not the spectral shapes, therefore they have no affect on determining β_T and T_{fo}. When changing the description from produced particles to cluster of two nucleons, various factors of two come into play and most of them cancel out. One factor comes in the momentum of the cluster, being the sum of the momenta of the nucleons. The second factor is the mass of the deuteron which is almost exactly twice the mass of the proton due to the small binding energy. The only parameter that is different in the description of produced particles and cluster is that the source spatial distribution function, written above as $f(x)$ is squared. In the case when clusters are produced, this function is the product of the distribution functions of the constituent nucleons. If we assume that protons and neutrons have the same spacial distribution, then this function will be equal to the square of the proton source spacial distribution function.

Two profiles have been commonly used in the literature when blast-wave model fits are done: a Gaussian density profile and a flat or box density profile. In the case of a Gaussian density profile, multiplying the constituent nucleon distribution function has the effect of narrowing the distribution. In the case of a flat, or box, density profile, this has no effect. The fits are typically done in a restricted transverse mass range $(m_T - m_0) < 1$ GeV in

which the soft particle production is expected to dominate the particle spectra and thus the hydrodynamics description is expected to hold.

4.3.2 Results

To extract the source temperature and surface flow velocity at freeze-out, we make a grid of (T_{fo}, β_T) pairs and then fit the expression in equation 4.6 to the measured particle spectrum. The χ^2 values of the fit are recorded and the best fit value for T_{fo} and β_T is obtained from a minimization procedure in the χ^2 space. The χ^2 values for each pair of the two parameters T_{fo} vs β_T obtained from fitting the spectra in the centrality class 0-10% are shown in Figure 4.13. Shown in the lower panels of the figures are the χ^2 contour levels obtained from fitting each particle spectrum separately. We observe that the parameters T_{fo} and β_T are anti-correlated; the different particles have different preferred parameter space and different sensitivity to the parameters. For example, the heavier particles are more sensitive to the radial flow velocity than to the kinetic freeze-out temperature. After a careful analysis, we can observe that the contours for the six particle species ($\pi^{\pm}$, $K^{\pm}$, p, and $\bar{p}$) do overlap at a single common point at the 3σ level. To find the values of the parameters at this overlap point, a simultaneous fit to the six single particles spectra was done which converges to the best fit value. Now, by adding the deuteron results to the contour plot, we do not observe the common overlap point for all eight particles. One can still try to find a "Best Fit" to match all particles.

The best fit results for T_{fo} and β_T are used to produce a curve which is compared to the measured spectra in Figure 4.14. The values for the parameter are shown in the plot.

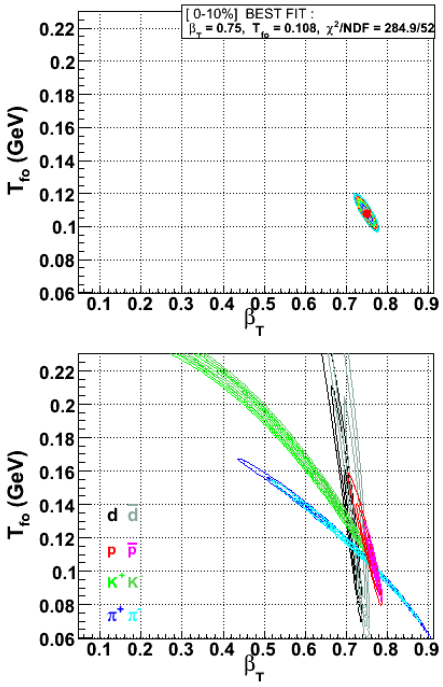

Figure 4.13: Contour plots for the hydrodynamical fit to the 200 GeV single particle particle transverse momentum spectra for $\pi^{\pm}$ $K^{\pm}$, p, $\bar{p}$, d, and $\bar{d}$ in the centrality 0-10%. The contour lines are in one standard deviation steps. The upper plot is from simultaneous fit with the best value shown as the dot. The lower plot is from independent fits for the 8 particles.

The legend describes data points for the different particle species. The same legend is used consistently in subsequent plots. The results for this eight particle simultaneous fit are very interesting. The main feature observed from this plot is the behavior for the prediction of the deuterons compared to the other particles. The pions, kaons, and protons follow the same trait, that is, the (blast-wave) prediction falls below the data in a region of transverse momentum which depends on the particle mass. The higher the mass, the higher the p_T at which deviations are observed. This behavior is expected for a source with a common flow velocity which boosts the heavier particles further in p_T. The point at which deviations are observed marks the region of the spectra where hard scattering is the dominant production

mechanism. We note that hard scattering production in $p + p$ collisions has been observed to produce power-law shaped transverse momentum spectra. Now, we observe the opposite behavior for the deuterons. The data points fall below the blast-wave fit at high p_T. We also noted that the fit does not describe well the low-p_T behavior either. Obviously, the deuteron spectra are not well described with the same freeze-out parameters as the produced hadrons. From the plots, we can observe that the blast-wave method does not predict the deuterons spectra well. One reason for this, is that the method assumes the deuterons can be produced in the process throughout the evolution of the source. However, due to their small binding energy, they are not likely to survive interactions in the hadron gas stage of the collisions. Thus, only those deuterons formed at the latest stage in the evolution of the expanding system are likely to survive. This complicated time evolution in the emission process is not implemented in the blast-wave model, so the failure of the model is not so surprising. Even full hydrodynamics calculations have difficulties reproducing observables which are sensitive to emission duration. Most notable is the failure of hydrodynamics to reproduce experimental results from intensity interferometry (HBT). With this is mind, we release the requirement that the deuterons freeze-out at the same T_{fo} and β_T as the produced hadrons and concentrate on obtaining a fit which will give a good description of the deuteron spectra with the goal to study the soft particle production range and the dynamics of the coalescence process. Figure 4.15 shows the simultaneous fit for hadrons, but with the deuterons fitted separately. Again, it can be observed that the fit fails to reproduce the data. A new approach is thus needed to measured the radial flow and temperature of deuterons.

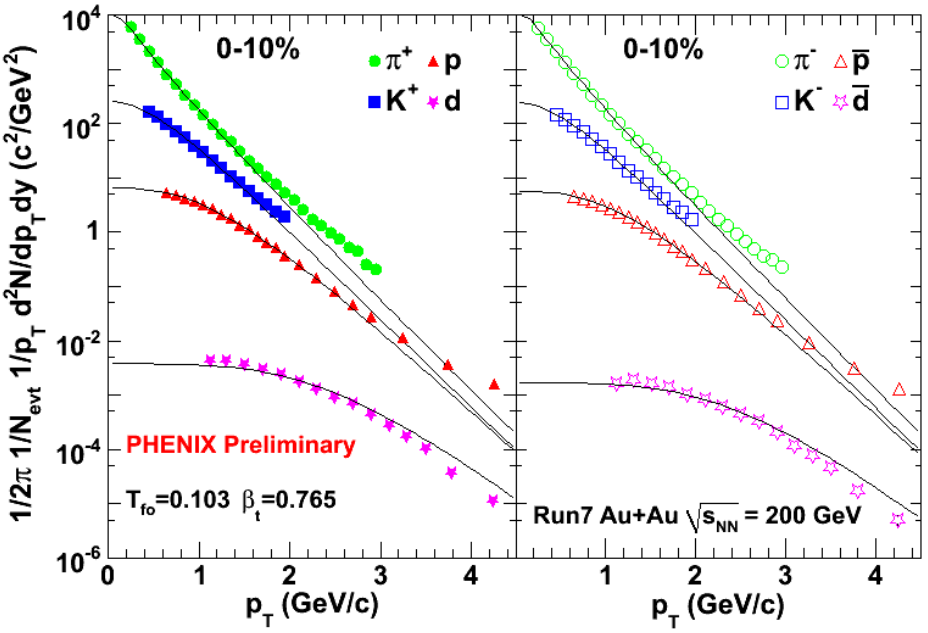

Figure 4.14: p_T spectra for 0-10% centrality Box profile. Positive particles (left) and negative particles (right) using the same parameters for deuterons as all produced hadrons.

4.3.3 A New Approach

In the previous section, fits were done either requiring freeze-out for all particles, or allowing the deuterons to freeze-out at a different time. In both cases the fit range over the spectra was limited to m_T - $m_0 < 1$ GeV which is know to be dominated by soft particle production. However, neither of these fits produce a good description of the deuteron spectra. In this section, we keep the produced hadron fit procedure the same, but conversely, the momentum range for the fit over the deuteron has been modified to fit the entire p_T range as opposed to just part of it. The new fit parameters describe the entire spectrum quite well. This is not surprising, as a deuteron momentum of 4 GeV/c corresponds to a nucleon momentum of 2 GeV/c, where the blastwave fits still fit the proton data well. It is not until $p_T \approx 3$ GeV/c for protons that there is noticeable deviation from the blastwave fits,

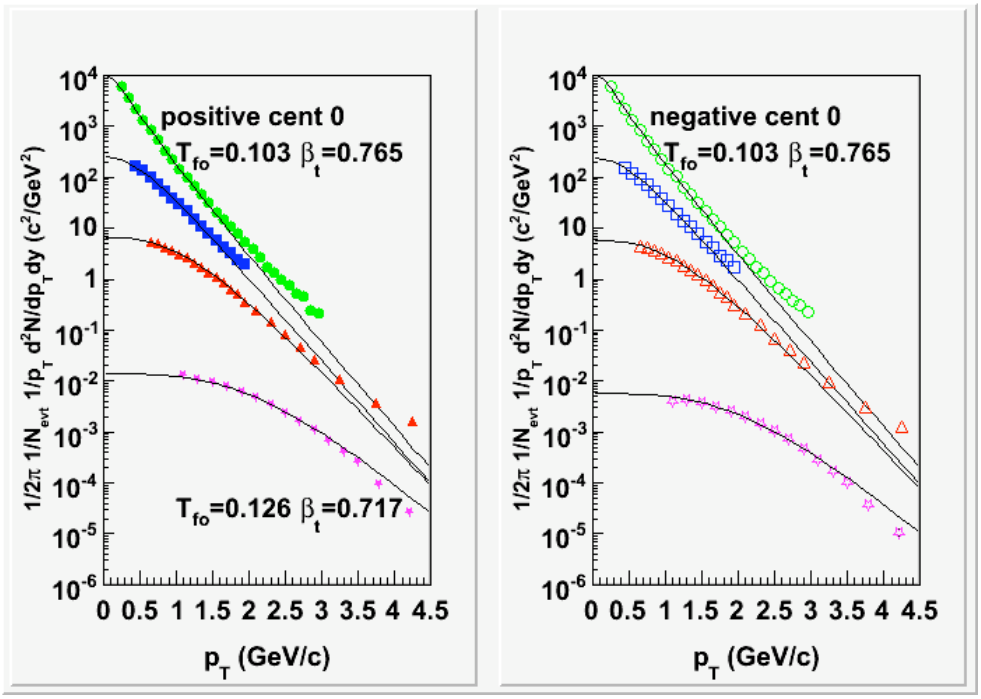

Figure 4.15: p_T spectra for 0-10% centrality Box profile. Deuterons are fitted separately over a limited p_T spectrum range.

as this is where hard production begins to dominate. Correspondingly, one would expect similar a deviation of the deuterons at a momentum of about 6 GeV/c. However, such high momentum is not available in this study.

We extended our study further by including a comparison between fit results using a box density profile and a Gaussian density profile. As discussed before, because the phase-space distribution function of the deuteron is presumed to be a product of the neutron and proton phase-space distribution functions, and the neutron's function is further assumed to be equivalent to that of the proton, one exponent of 2 appears in the density profile function when clusters of size A=2 are described in the blast-wave model. This modification of the model will produce identical results for the produced hadrons if we use a box spacial density profile, but will differ if we use a Gaussian profile. The result for a box profile

phase space distribution is shown in Figure 4.16. The results fitted to spectra are shown in Figure 4.17. The only difference of this Figure 4.17 to Figure 4.15 is that the deuterons fit range is increased. However, deuterons still do not freeze-out at the same β and T as produced hadrons. In both cases they require lower flow velocities than the protons. This can be understood as a result from the limited time duration of the coalescence process The result is that the final deuteron spectrum does not carry the full integrated flow as the proton spectra do. Here we observe that there is no effect which originates in the different density distribution function for clusters, since for a box profile vis-a-vis $1^2 = 1$. However, for a Gaussian profile shown in Figure 4.18 , the exponent two multiplies with the exponent in the Gaussian function, and effectively halves the FWHM [27]. The fit to the spectra using the Gaussian phase-space distribution results are shown in Figure 4.19). Now, the deuteron spectra require a higher flow velocity than before (still lower than the proton spectra, though) but a much lower freeze-out temperature. It appears that in order to compensate for the very compact source, the blast-wave needs longer source expansion (and cooling) to reproduce the spectra.

4.4 Particle Ratios $\bar{d}/d$ and the Neutron Chemical Potential

In this section, we present the ratio of antiparticles to particles. Figures 4.20, and A.33 through A.37 show the particle ratios of $\bar{d}/d$ for different centrality classes. The error bars represent statistical errors and the shaded boxes on each panel represent the systematic errors (see Section A.1.8).

As we can observe from the plots, the $\bar{d}/d$ ratio does not change from one centrality

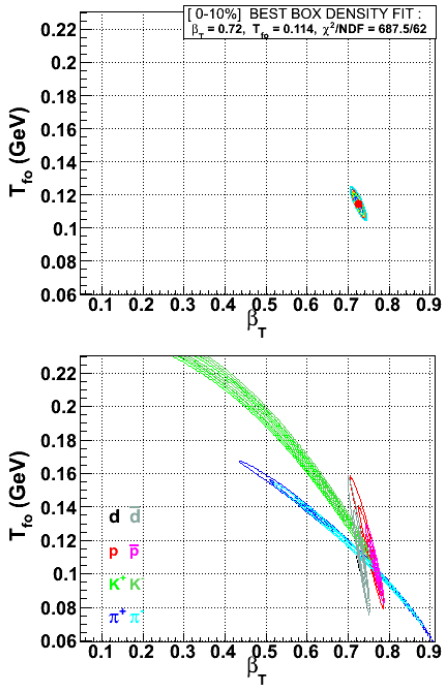

Figure 4.16: Box profile contour plots for the hydrodynamical fit to the 200 GeV single particle particle transverse momentum spectra for $\pi^{\pm}$ $K^{\pm}$, p, $\bar{p}$, d, and $\bar{d}$ in the centrality 0-10%.

to the other within the experimental errors over the measured p_T range (Table 4.2). We find that $\bar{d}/d$ = 0.42$\pm$ 0.0029 for min-bias data. This is comparable with the square of the $\bar{p}/p$ = 0.73 $\pm$ 0.01 [1], within the statistical and the systematic errors, as expected if (anti-)deuterons are formed by coalescence of (anti-)nucleons. Using the measured $\bar{d}/d$ and $\bar{p}/p$ we can estimate the $\bar{n}/n$ ratio and chemical potential. In a thermal model, the particle yields follows a Boltzmann distribution with a common temperature. Previous PHENIX study [48] found that $\bar{n}/n$ = 0.64 $\pm$ 0.04. The results presented here are consistent with this finding. Based on this results it appears that the chemical potential for neutrons is larger for that of protons $\mu_n \geq \mu_p$. This is expected since the entrance $Au + Au$ channel has larger net neutron density than net proton density.

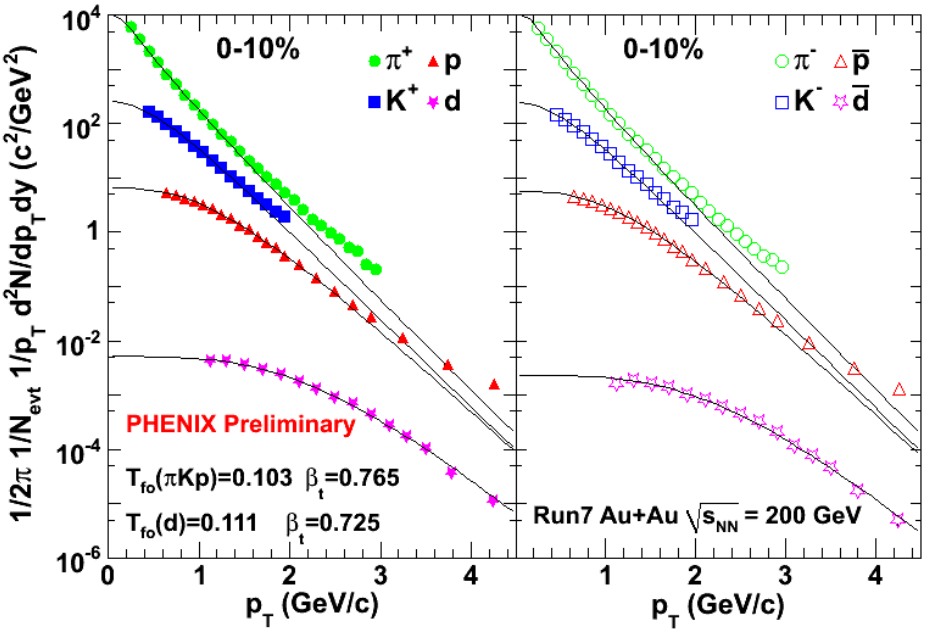

Figure 4.17: p_T spectra for 0-10% centrality Box profile. Deuterons are fitted over entire p_T spectrum range.

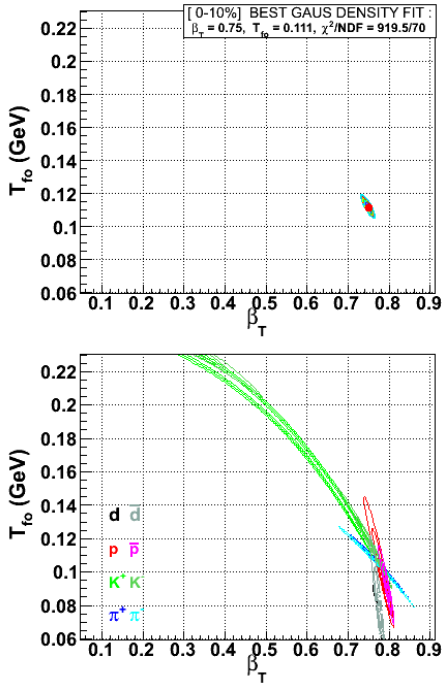

Figure 4.18: Gaussian profile contour plots for the hydrodynamical fit to the 200 GeV single particle particle transverse momentum spectra for $\pi^{\pm}$ $K^{\pm}$, p, $\bar{p}$, d, and $\bar{d}$ in the centrality 0-10%.

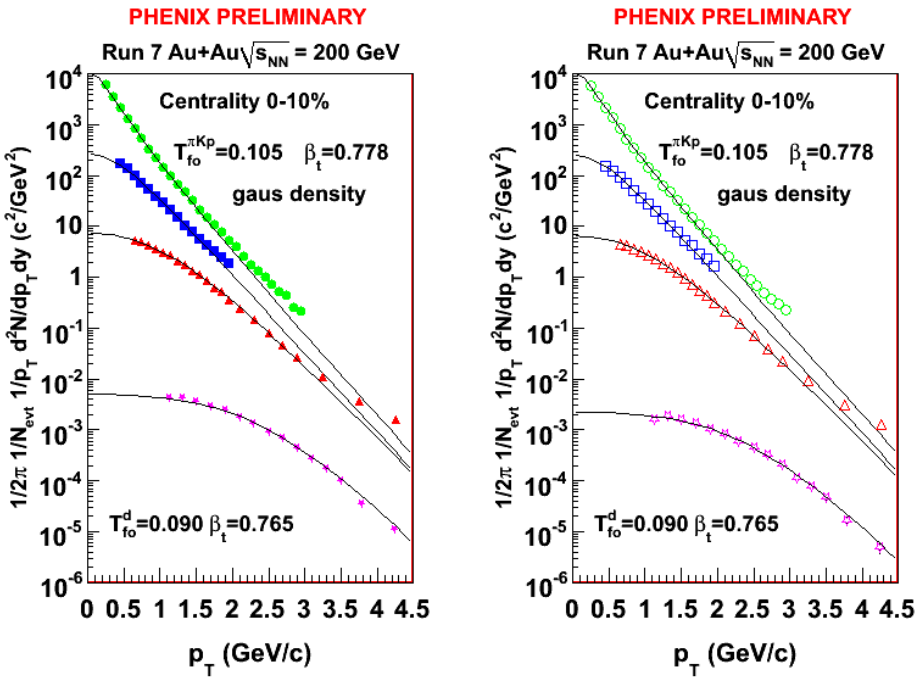

Figure 4.19: p_T spectra for 0-10% centrality with Gaussian profile. Deuterons are fitted over entire p_T spectrum range.

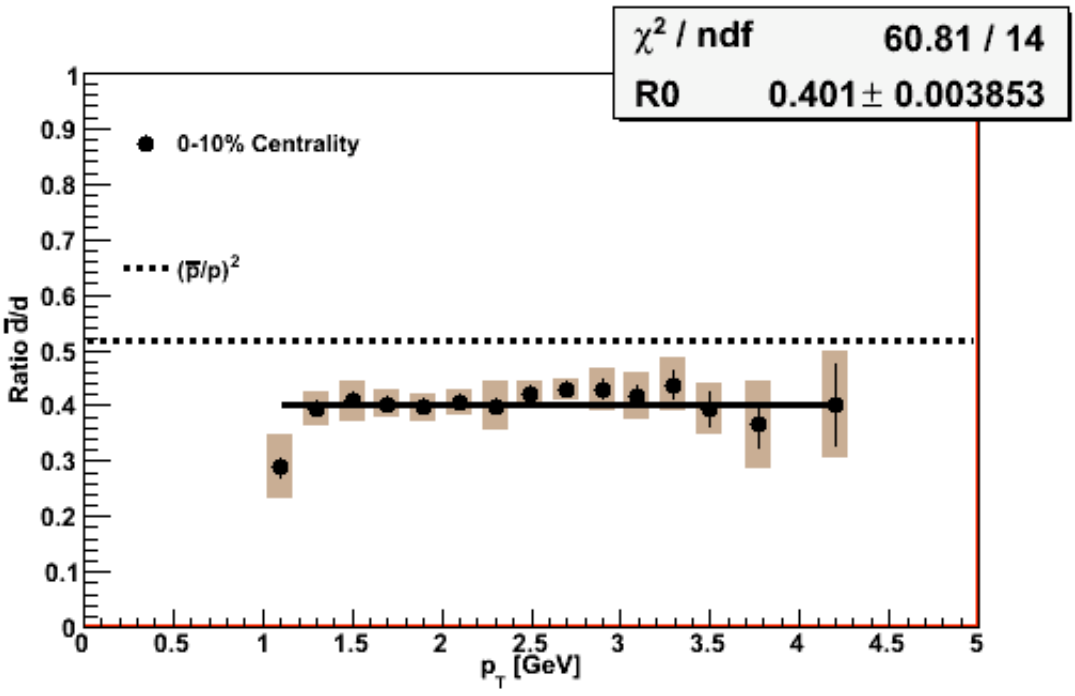

Figure 4.20: $\bar{d}/d$ ratio 0-10% centrality.

Table 4.2: Fit results of $\bar{d}/d$ for all centrality classes.

centrality	**Ratio**$\bar{d}/d$)	**Fit Error**
0 – 10%	0.401	0.003
10 – 20%	0.406	0.004
20 – 40%	0.432	0.004
40 – 60%	0.447	0.005
60 – 92%	0.442	0.011
Min. bias	0.419	0.0029

4.4.1 Systematic Errors for $\bar{d}/d$ Ratios

The systematic errors were calculated by making the same cuts as for the spectra as outlined in Section 3.9, and then taking the $\bar{d}/d$ ratio. The final ratios for all centrality

classes are tabulated in Tables A.11, A.12, and A.13

4.5 Coalescence Parameter B_2

With a binding energy of 2.24 MeV, the deuteron is a very loosely bound state. Thus, it is formed at the latest stage in the evolution of the system by the coalescence of protons and neutrons tightly correlated in position and momentum space. The d and $\bar{d}$ yields provide information about the space-time evolution of the system and the source size at freeze-out. The invariant d and $\bar{d}$ yields can be related [28] to the primordial nucleon yields as:

$$E_d \frac{d^3N_d}{dp_d^3}\bigg|_{p_d=2p_p} = B_2 \left[E_p \frac{d^3N_p}{dp_p^3} \right]^2 \tag{4.7}$$

where B_2 is the two-nucleon coalescence parameter. The above equation includes an implicit assumption that the ratio of neutrons to protons is unity. The p and $\bar{p}$ spectra measured in [1] and in conjunction with the d and $\bar{d}$ presented here, are used to extract the coalescence parameter. Physically, the coalesce parameter is the measure of the source size: $B_2 \propto 1/V$.

Figure 4.21 shows the coalescence parameter B_2 as a function of p_T for different centrality classes. The decrease in more central collisions implies that the average relative separation between nucleons increases in large sources, thus decreasing the probability of deuteron formation. We also observe that the B_2 increases with p_T. This is consistent with an expanding source because position-momentum correlations lead to a higher coalescence probability at larger p_T.

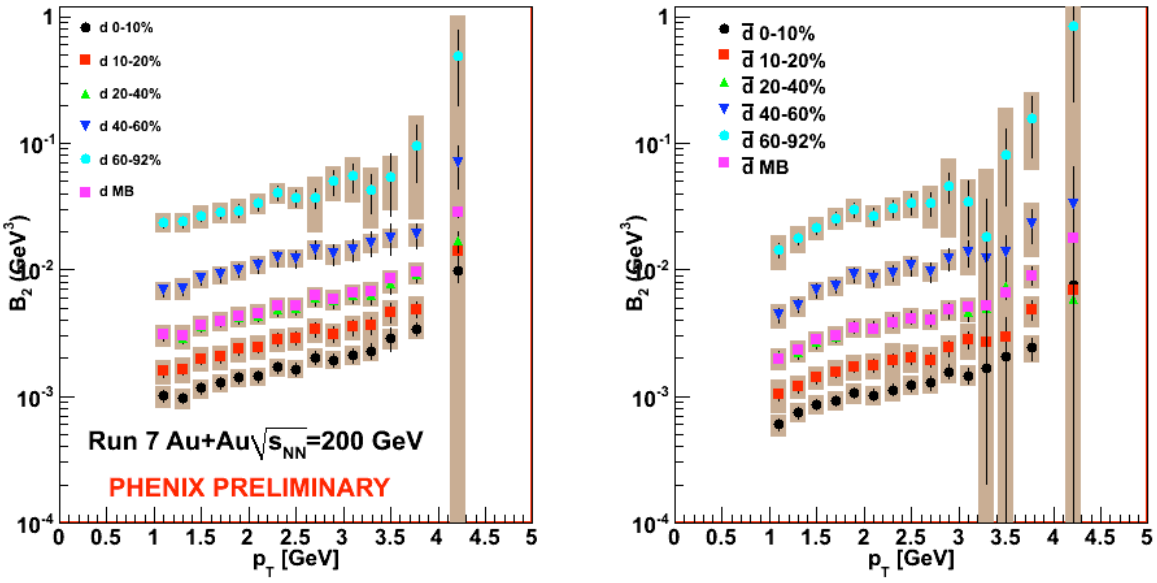

Figure 4.21: Coalescence parameter B_2 vs p_T for deuterons (left) and anti-deuterons (right). The bands indicate the systematic errors.

4.5.1 Energy Dependence of B_2 Parameter

Next, we plot our B_2 values along with previously measured coalescence values (Figure 4.22). Here, we compare our result for all centrality classes with results at lower energies from the Bevelac [51], AGS [52, 53], SPS [54, 55], and STAR (130 GeV data) [49]. From the plot, it can be noticed that the coalescence parameter is nearly independent of $\sqrt{s}$ indicating that the source volume does not change much with beam energy. This behavior is consistent with what has been observed in Bose-Einstein correlation HBT measurements [56, 57]. This may also indicate that the freeze-out conditions are similar to those existing at SPS and AGS energies.

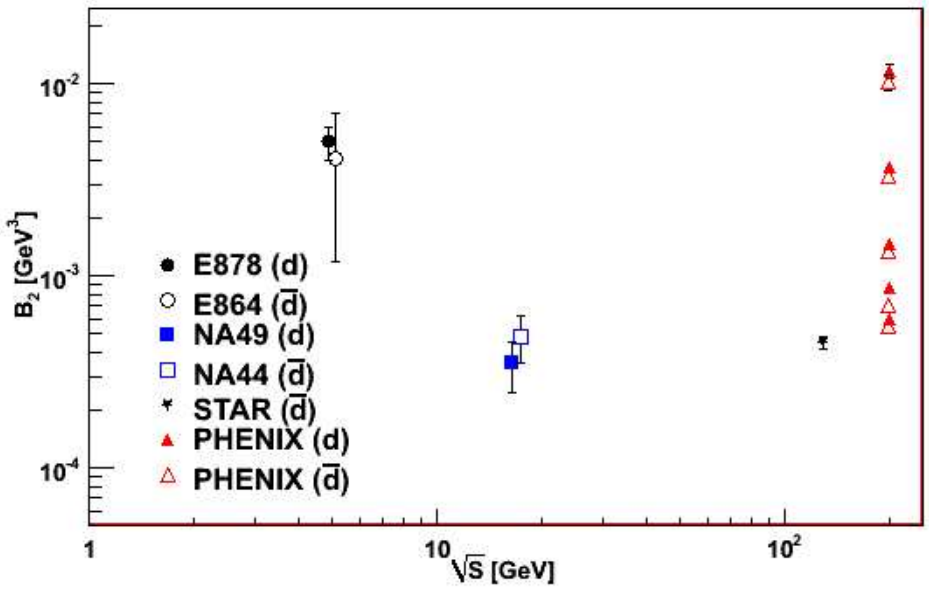

Figure 4.22: Comparison for the coalescence parameter (B_2) for (anti-)deuterons with other experiments at different values of $\sqrt{s}$. This comparison points come from the most centrality class in each experiment. PHENIX points (red triangles) going from the low to high values in the measured B_2 correspond to the central to peripheral events.

4.5.2 B_2 and System Volume

The coalescence parameter B_2 can also be used to obtain the source size at freeze-out. Now, we take two p_T values over all centrality classes to study the system. In Figure 4.23 we plotted these B_2 values as a function of N_{part}. Thermodynamic models [26] predict that B_2 scales with the inverse of the effective volume V_{eff}. In Figure 4.24, $1/B_2$ is plotted as a function of N_{part} for two fixed p_T bins. The data show a linear rise of $1/B_2$ as a function of N_{part}.

Using a fireball model in thermal and chemical equilibrium and assuming a Gaussian source, we extract the radius of the source [25, 26] with the following relation:

$$R^3 = \alpha R_{np} (\hbar c)^3 \frac{m_d}{m_p^2} (B_2)^{-1} \tag{4.8}$$

where $\alpha = (3/4)\pi^{3/2}$ for a Gaussian source and $\alpha = (9/2)\pi^2$ for a hard sphere and R_{np} is the ratio of neutrons to protons [b]

Assuming a Gaussian distribution particle source, we take two p_T data point (p_T = 1.5 and p_T = 3.0 GeV) for all centrality classes. Figure 4.23 shows B_2 as a function of N_{part} for these two p_T points. Here we can observe a significant change in B_2 from 14.5 to 60 N_{part}.

In figure 4.24, we also plotted the same two p_T points, but now using V_{eff} as a function of N_{part} ($V_{eff} \propto 1/B_2$). From this figure, we can observe B_2 vs N_{part} has a consistent linear rise. The soft particle production also scales as N_{part}. These two findings taken together imply that the source freeze-out happens at constant particle density independent

[b] Assume to be unity here

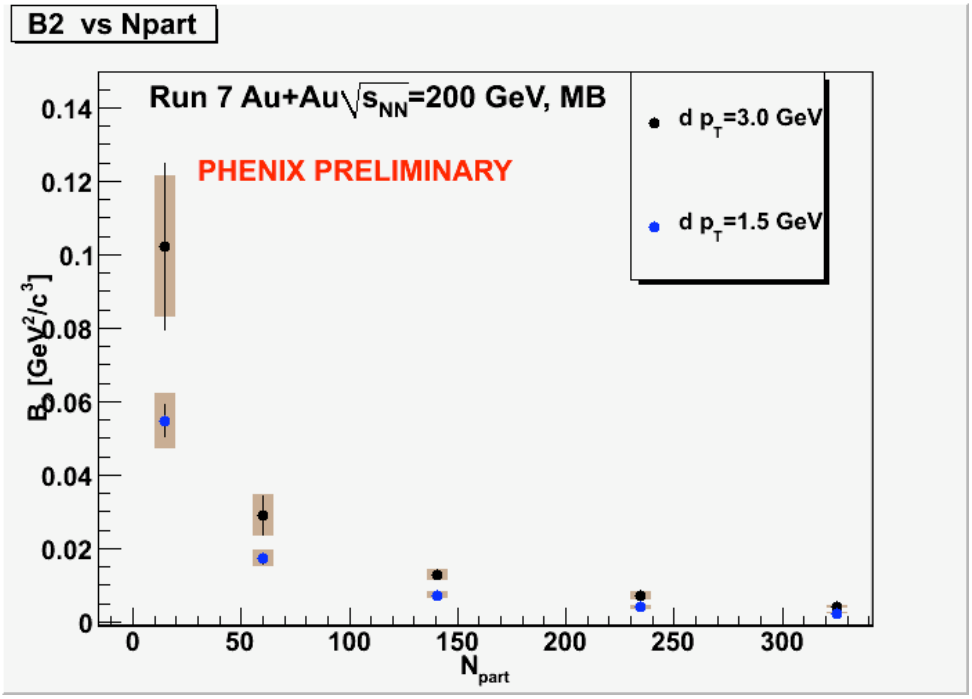

Figure 4.23: Coalescence parameter (B_2) as a function of the number of participants (N_{part}).

of the initial size of the source, the radial flow velocity or the freeze-out temperature.

Figure 4.25 shows the source radius as a function of the cubic root of the number of participants. The numerical results are consistent with those obtained from the HBT correlations of pions [58].

4.6 Nuclear Modification Factors

Nuclear modification factors are used to study parton energy loss in QGP. It has been observed that baryons show a different behavior from that of mesons, where the mesons exhibit a suppression effect at intermediate p_T while baryons do not [30]. Deuterons are formed by the coalescence of two baryons which can provide information about this process both at the partonic and hadronic stage. It is expected that, as a baryon, the neutron should

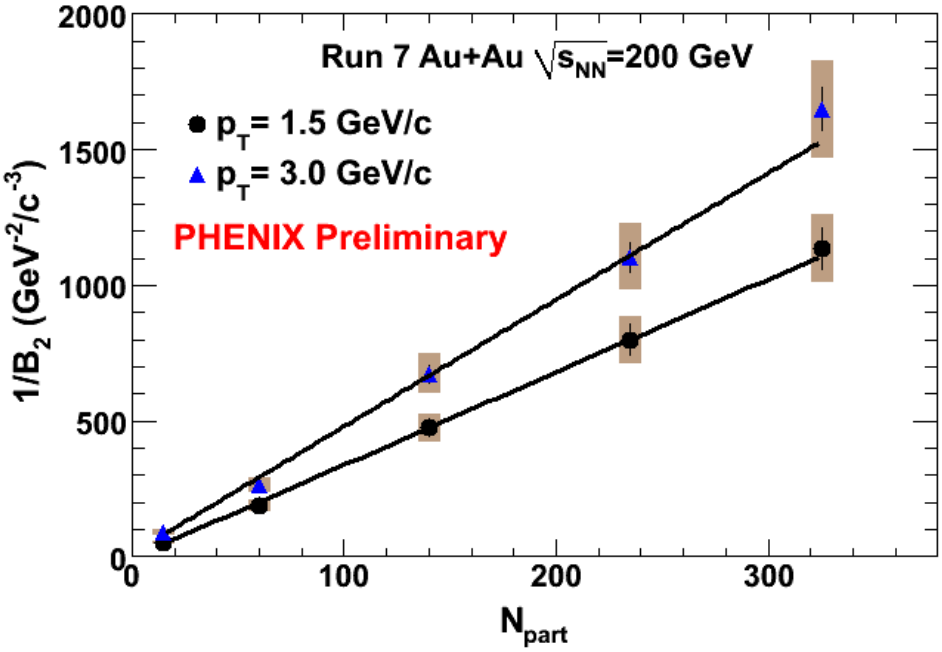

Figure 4.24: Inverse coalescence parameter as a function of the number of participants.

have a similar R_{CP} to that of the proton, but this needs to be verified. The deuteron R_{CP} can be used to check this. Figure 4.6 shows the N_{coll} scaled central to peripheral ratio (R_{CP}) in Au+Au collisions for deuterons and protons. The deuteron p_T has been divided by 2 ($p_T^d = 2p_T^p$) to facilitate the comparison based on the momentum of the primordial nucleon. We define the R_{CP} as follows:

$$R_{CP} = \frac{Yield^{0-20\%} / < N_{coll}^{0-20\%} >}{Yield^{60-92\%} / < N_{coll}^{60-92\%} >}. \tag{4.9}$$

It is quite surprising that the maximum of the R_{CP} reaches a value well in excess of 1. This quantity is affected by two factors: the centrality dependence of the coalescence parameter (see Equation 4.7), and the scaling production yields of protons and neutrons.

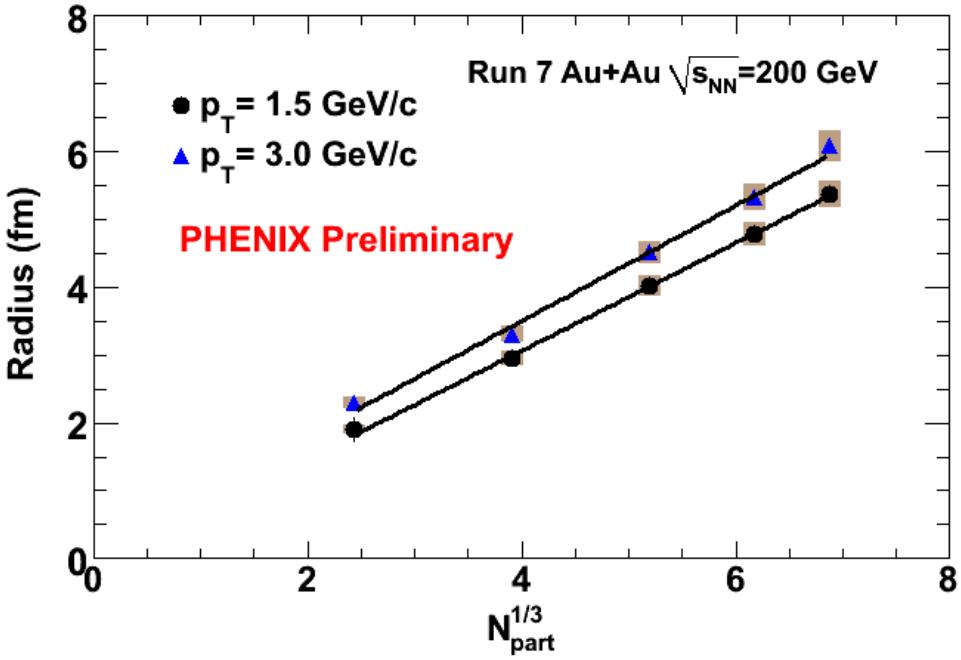

Figure 4.25: Radius as a function of the cube root of the number of participants.

If we rewrite the deuteron R_{CP} in terms of that of the proton, we get

$$R_{CP}^{deuteron} = \frac{B_2^{0-20\%}}{B_2^{60-92\%}} (R_{CP}^{proton})^2 \frac{\langle N_{coll}^{0-20\%} \rangle}{\langle N_{coll}^{60-92\%} \rangle}. \tag{4.10}$$

Noting that B_2 is inversely proportional to N_{part}, this can be rewritten as

$$R_{CP}^{deuteron} = \frac{\langle N_{part}^{60-92\%} \rangle}{\langle N_{part}^{0-20\%} \rangle} (R_{CP}^{proton})^2 \frac{\langle N_{coll}^{0-20\%} \rangle}{\langle N_{part}^{60-92\%} \rangle}. \tag{4.11}$$

Finally, recognizing that for peripheral collisions N_{coll} and N_{part} are roughly equal, while for central collisions N_{coll} is greater than N_{part} by roughly a factor of 3, we get

$$R_{CP}^{deuteron} \approx 3(R_{CP}^{proton})^2. \tag{4.12}$$

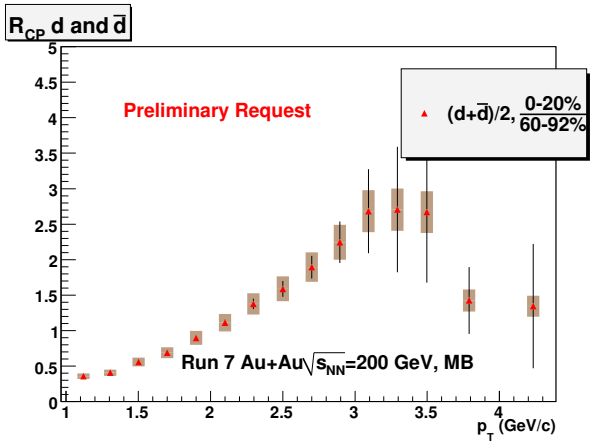

Figure 4.26: Nuclear modification factor for deuterons in $Au + Au$ collisions. The shaded bands represent the systematic error with normalization.

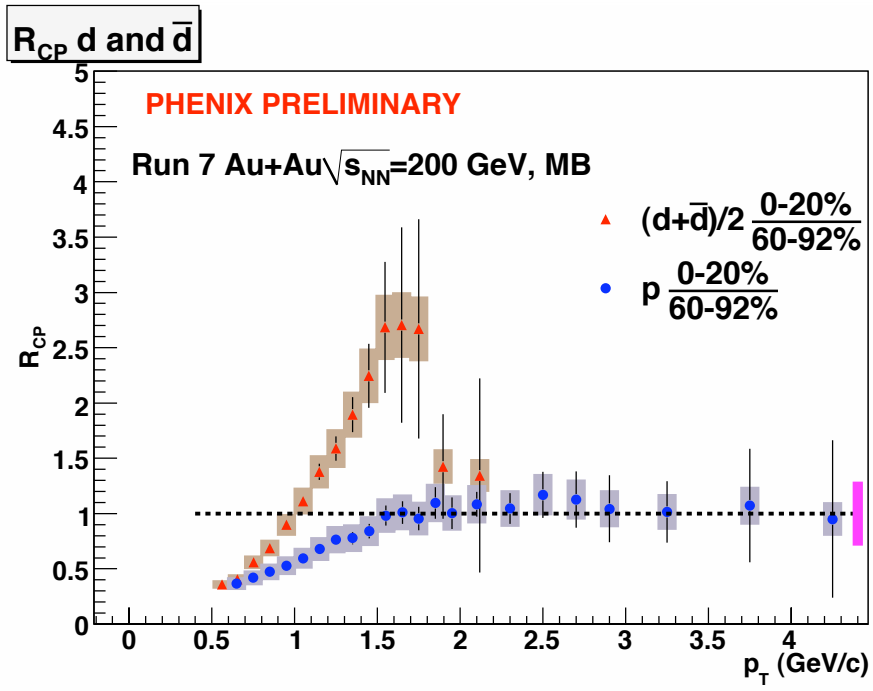

Figure 4.27: Nuclear modification factor for deuterons and protons in $Au + Au$ collisions. The shaded bands represent the systematic error with normalization. The bar around R_{CP} =1 is the error associated with the determination of the number of collisions. The deuteron p_T have been divided by 2.

CHAPTER V

CONCLUSIONS

Nuclear clusters have been a useful tool to establish collective effects throughout the history of heavy ion collisions. We have studied the final state effects of the produced matter from ultrarelativistic $Au + Au$ collisions at $\sqrt{s_{NN}} = 200$ GeV by analyzing the production of the simplest nuclei: deuterons and anti-deuterons. The transverse momentum spectra of d and $\bar{d}$ in the range $1.1 < p_T < 5.0$ GeV/c have been measured at mid-rapidity in $Au+Au$ collisions at $\sqrt{s_{NN}}$ =200 GeV. Using the new TOF.W detector, we have expanded previous PHENIX measurements in both the low and high p_T. We found the transverse momentum spectra of d and $\bar{d}$ to be less steeply falling than (anti-) proton spectra.

The big data set from Run 7 allows us to increase the number of centrality classes to five. This expansion of centrality classes allowed to do centrality studies on spectra yields and average p_T . Due to an overall good qualitative agreement between radial flow considerations and the experimental results seen so far, it is interesting to check the quantitative agreement with hydrodynamical models.

Measurement of radial flow velocity and freeze-out temperature using the blast-wave hydrodynamics model for deuterons and anti-deuterons was attempted. Our results indicate that within this model the deuterons do not freeze-out contemporaneously with the produced hadrons. The deuteron spectra require a lower flow velocity than the proton spectra, but a much higher freeze-out temperature. This tells us that the deuterons that survive

to be measured in the detector do not experience the full evolution of the source, but just part of it, most likely the final part. The deuteron spectra can be described by a hydrodynamic calculation curve in the full range measured by us. We conclude this because a better fit is obtained when we do not restrict the m_T range of the fit as we do for other particles. We also observed that different source density profiles give different T_{fo} results but we are unable to distinguish one versus the other, both work well. We should note that the Gaussian source, will produce the same slopes for the p and d spectra if you use the same T and β, this does not work at all no matter what density profile you use.

It is expected that, as a baryon, the neutron should have a similar R_{CP} to that of the proton. The deuteron R_{CP} was used to check this. Quite surprising is the result that the maximum of the R_{CP} reaches a value of well in excess of 1. We concluded that this quantity is affected by two factors: the centrality dependence of the coalescence parameter, and the scaling production yields of protons and neutrons.

The ratio of antiparticles to particles for the five centrality classes was calculated. We observed the $\bar{d}/d$ ratio does not change as we go from one centrality to the other within the experimental errors over the measured p_T range. We find that $\bar{d}/d$ = 0.42 $\pm$ 0.0029 for minimum bias data. This is comparable with the square of the $\bar{p}/p$ = 0.73 $\pm$ 0.01, within the statistical and the systematic errors, as expected if (anti-)deuterons are formed by coalescence of (anti-)nucleons. Using the measured $\bar{d}/d$ and $\bar{p}/p$ we can estimate the $\bar{n}/n$ ratio and chemical potential. In a thermal model, the particle yields follows a Boltzmann distribution with a common temperature. A previous PHENIX study [48] found that $\bar{n}/n$ = 0.64 $\pm$ 0.04. The results presented here are consistent with this finding. Based on this results it appears that the chemical potential for neutrons is larger for that of protons $\mu_n \geq$

μ_p . This is expected since the entrance $Au + Au$ channel has larger net neutron density than net proton density.

We extracted the coalescence parameter B_2 for deuterons. We observed an increase of B_2 as a function of p_T, which agrees with an expanding source model. The B_2 can also be used to calculate the effective source volume. We observed a decrease in B_2 for more central collisions where the volume of the system is larger. The B_2 measured in nucleus-nucleus collisions is independent of $\sqrt{s_{NN}}$ above 12 GeV, consistent with Bose-Einstein correlation measurements of the source radii. B_2 is equal within errors for both deuterons and anti-deuterons. Our measurements indicate that the source freezes out at constant particle density (because volume $\sim N_{part}$ and $dN/dy \sim N_{part}$, hence the ratio is flat with N_{part}).

We have measured the deuteron spectra for $Au + Au$ collisions at $\sqrt{s_{NN}}$ = 200 GeV. These new data points should be compared to a full hydrodynamical calculation to see whether they can be reproduced with the same T and β as for hadrons produced directly in the collisions. This measurement is very sensitive to the emission duration and the proper description of the source density. What one can learn from such a comparison is how long the emission process is. This in turn can tell us whether the system went through a first order phase transition, in which due to the latent heat the system spends a long time at the same temperature (known as the "burning log scenario"), or if the system underwent a cross-over transition in which there are no pronounced discontinuities in thermodynamic quantities.

APPENDIX A

EXTRA FIGURES AND TABLES

A.1 Figures

A.1.1 Signal Extraction for Deuterons Figures

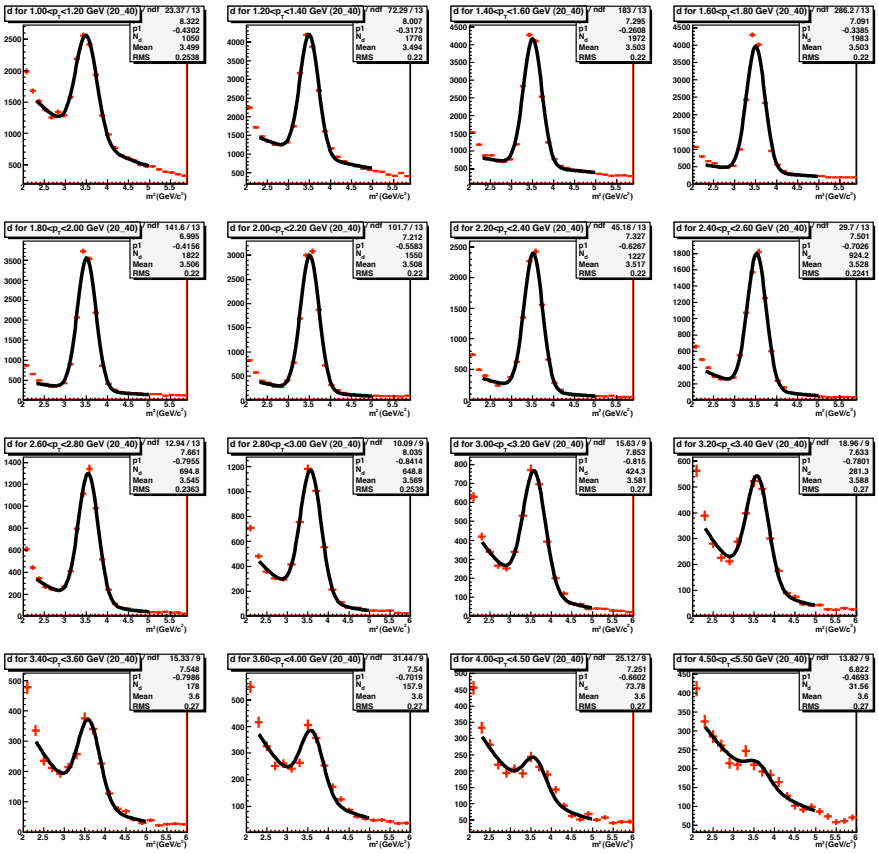

Figure A.1: Raw deuteron yield for 20-40% centrality.

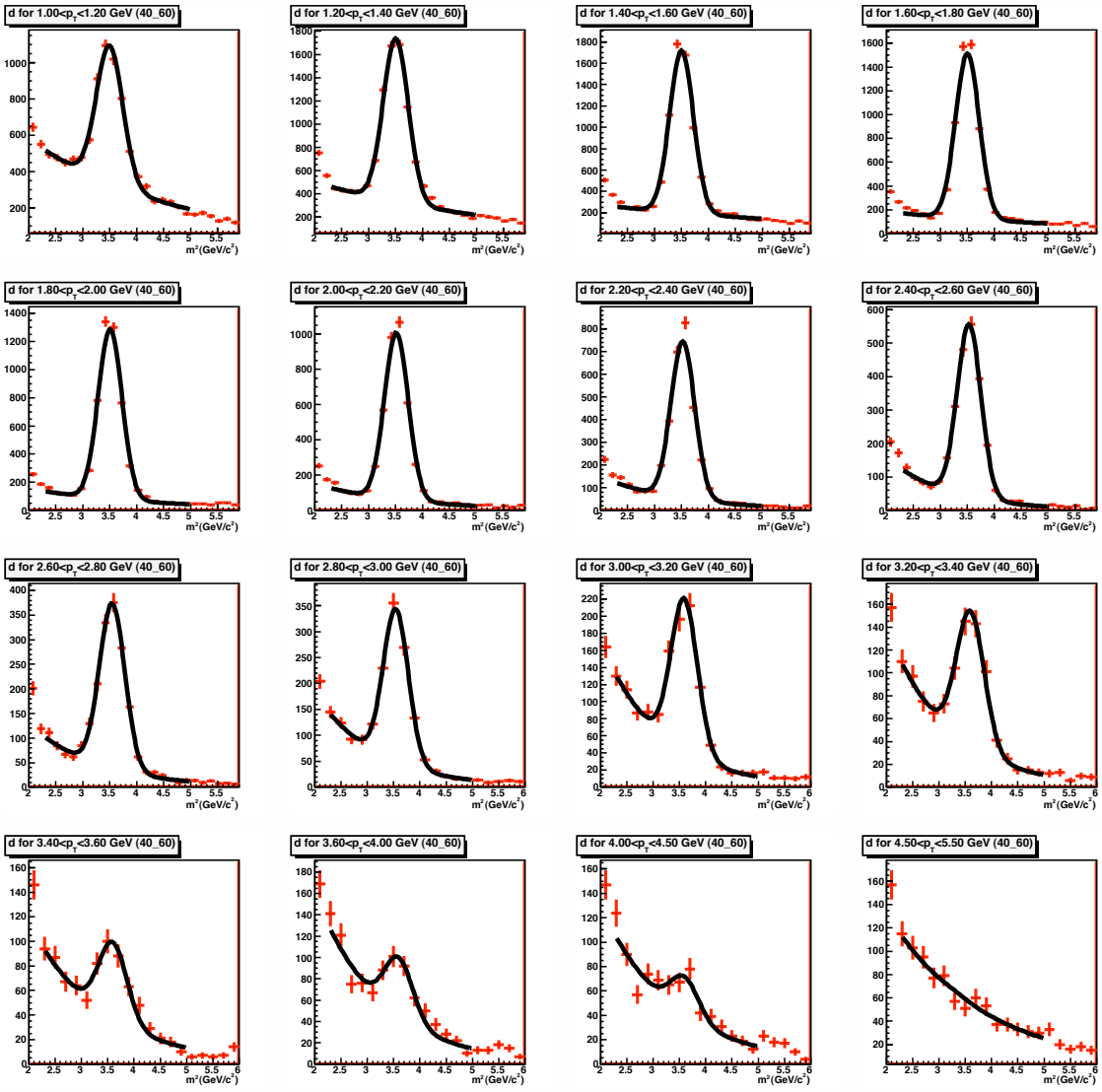

Figure A.2: Raw deuteron yield for 40-60% centrality.

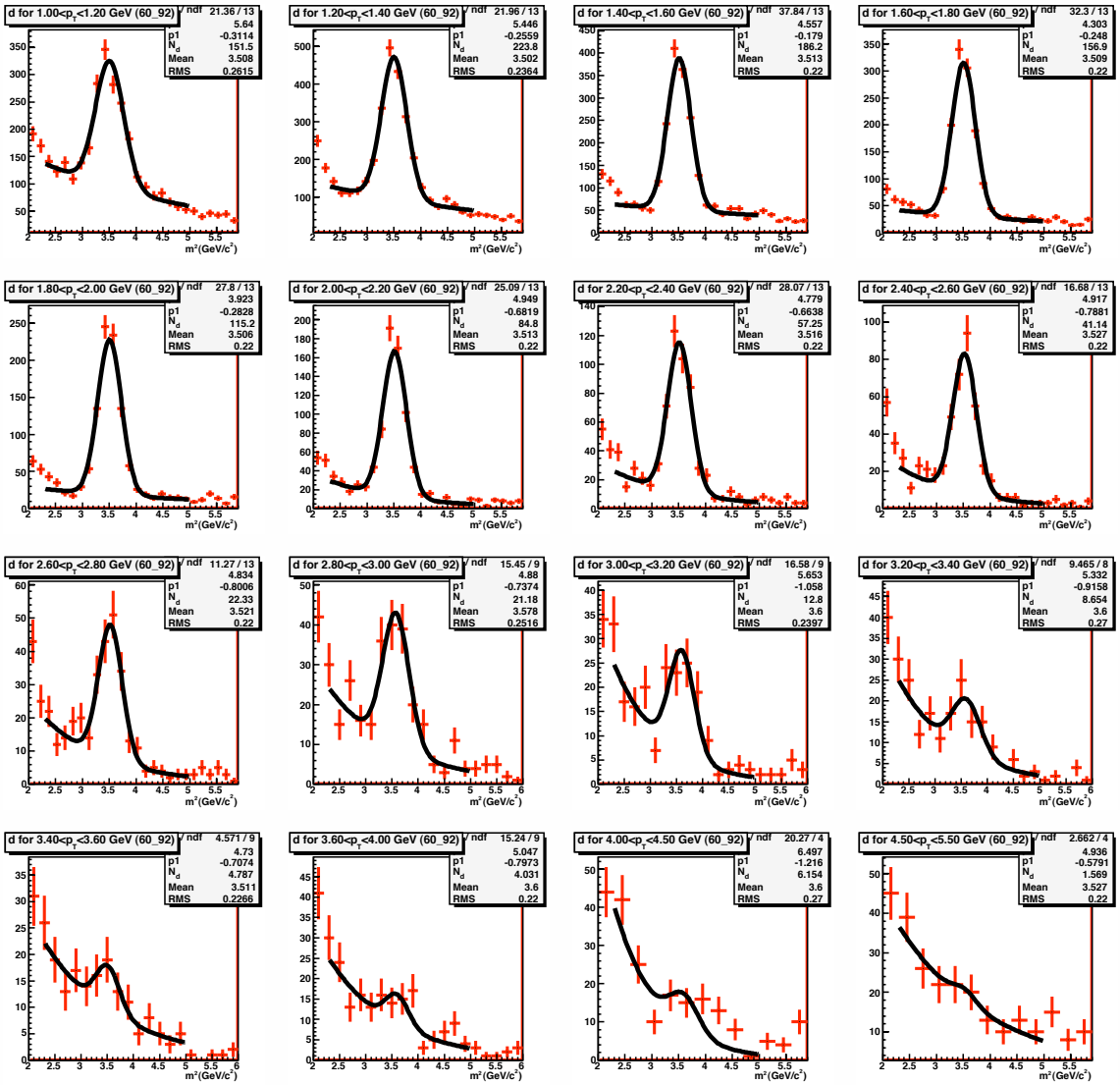

Figure A.3: Raw deuteron yield for 60-92% centrality.

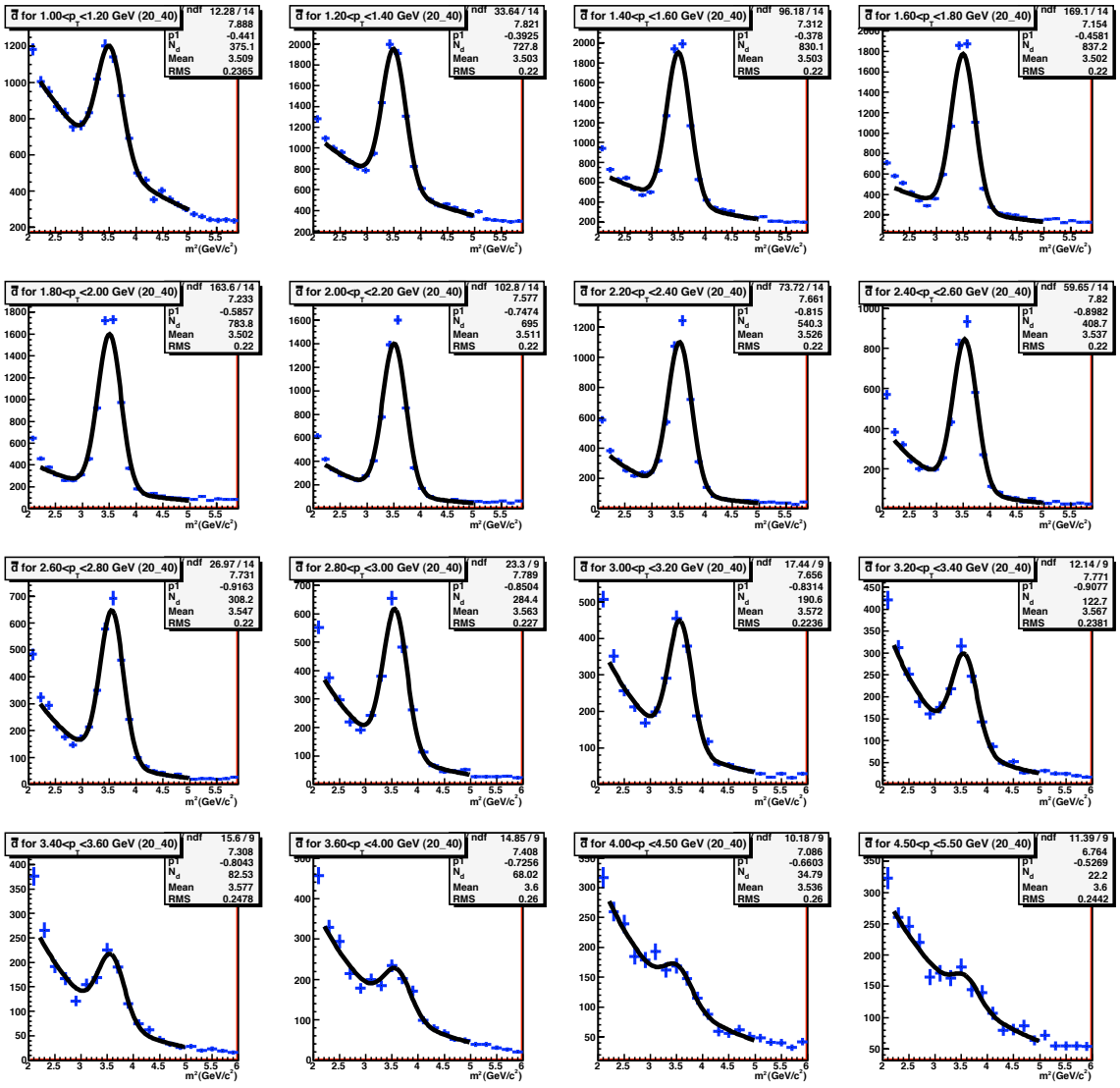

Figure A.4: Raw anti-deuteron yield for 20-40% centrality.

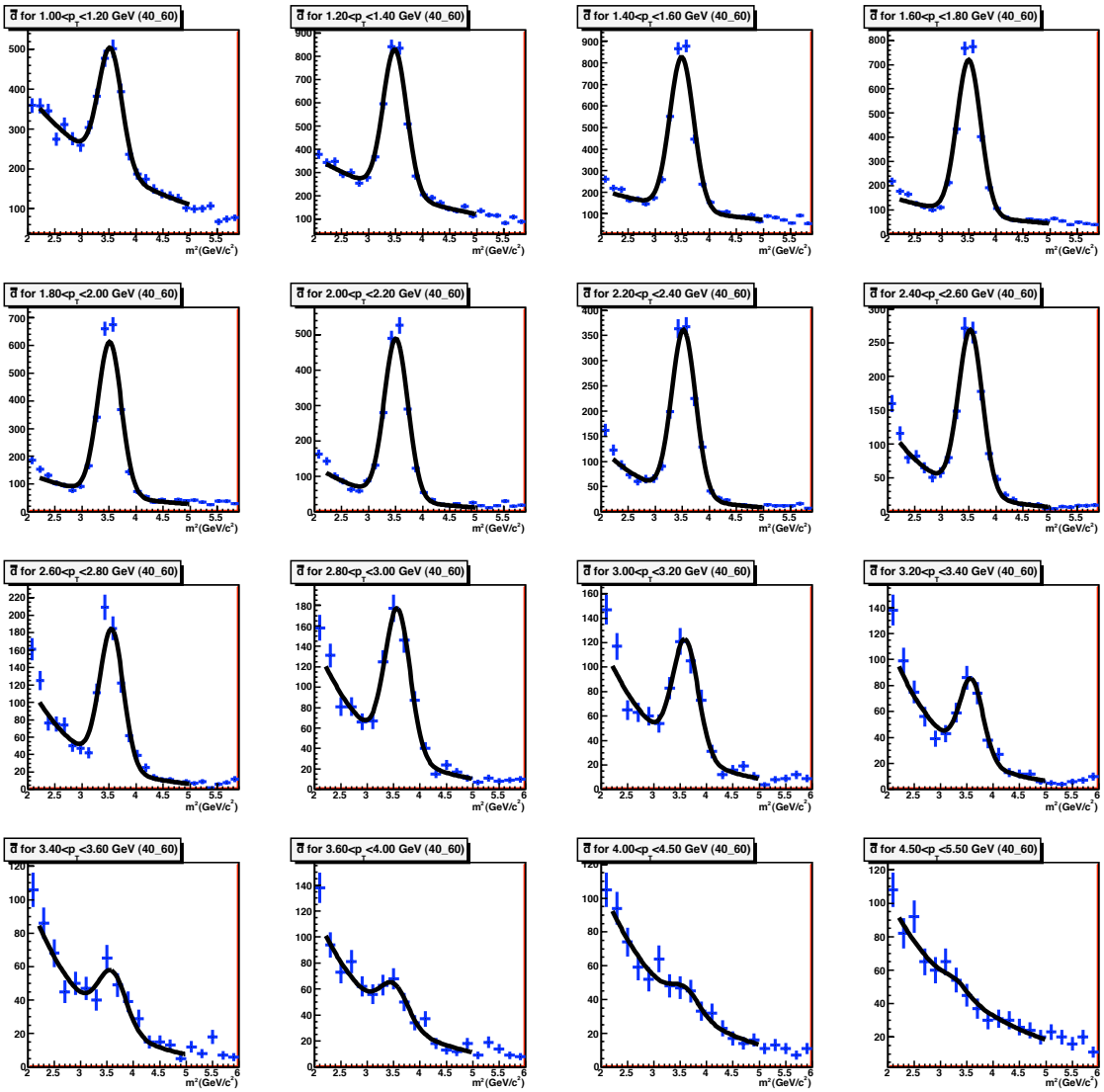

Figure A.5: Raw anti-deuteron yield for 40-60% centrality.

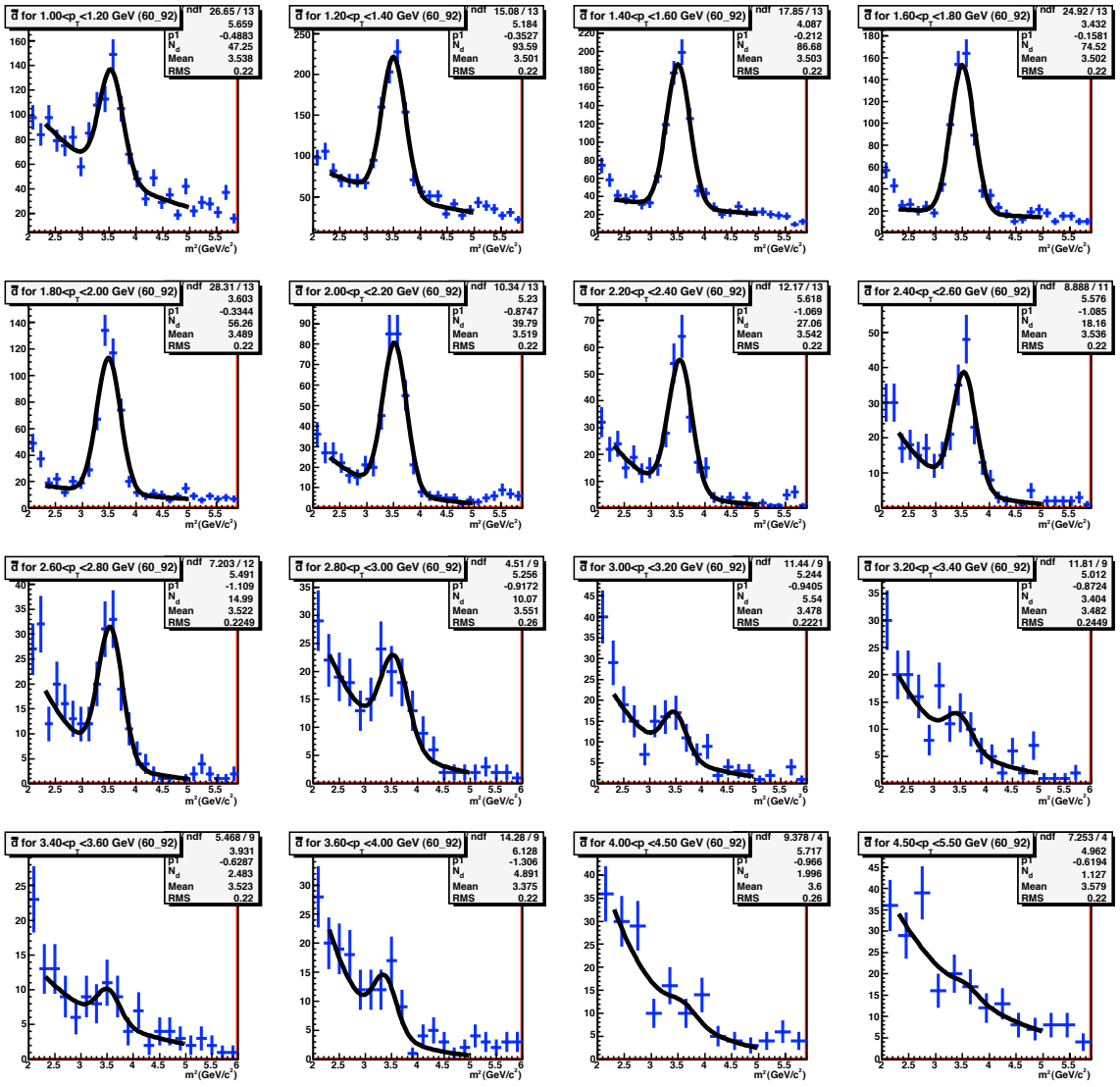

Figure A.6: Raw anti-deuteron yield for 60-92% centrality.

A.1.2 Single Particle Monte Carlo Figures

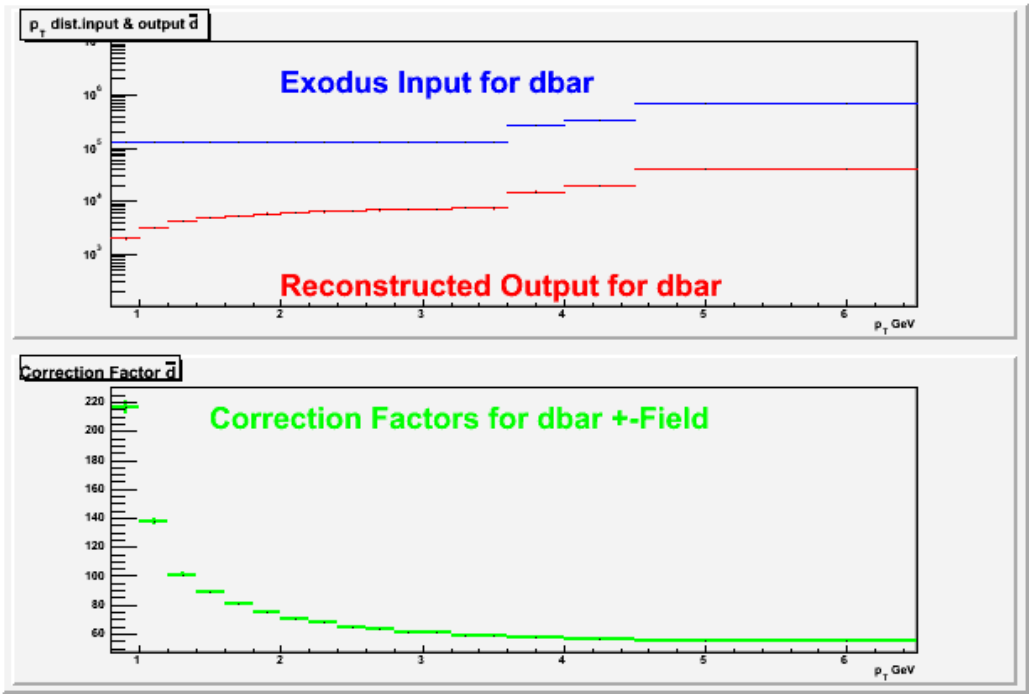

Figure A.7: MC correction factor as a function of p_T for anti-deuterons +- Field.

A.1.3 Tracking Efficiency Figures

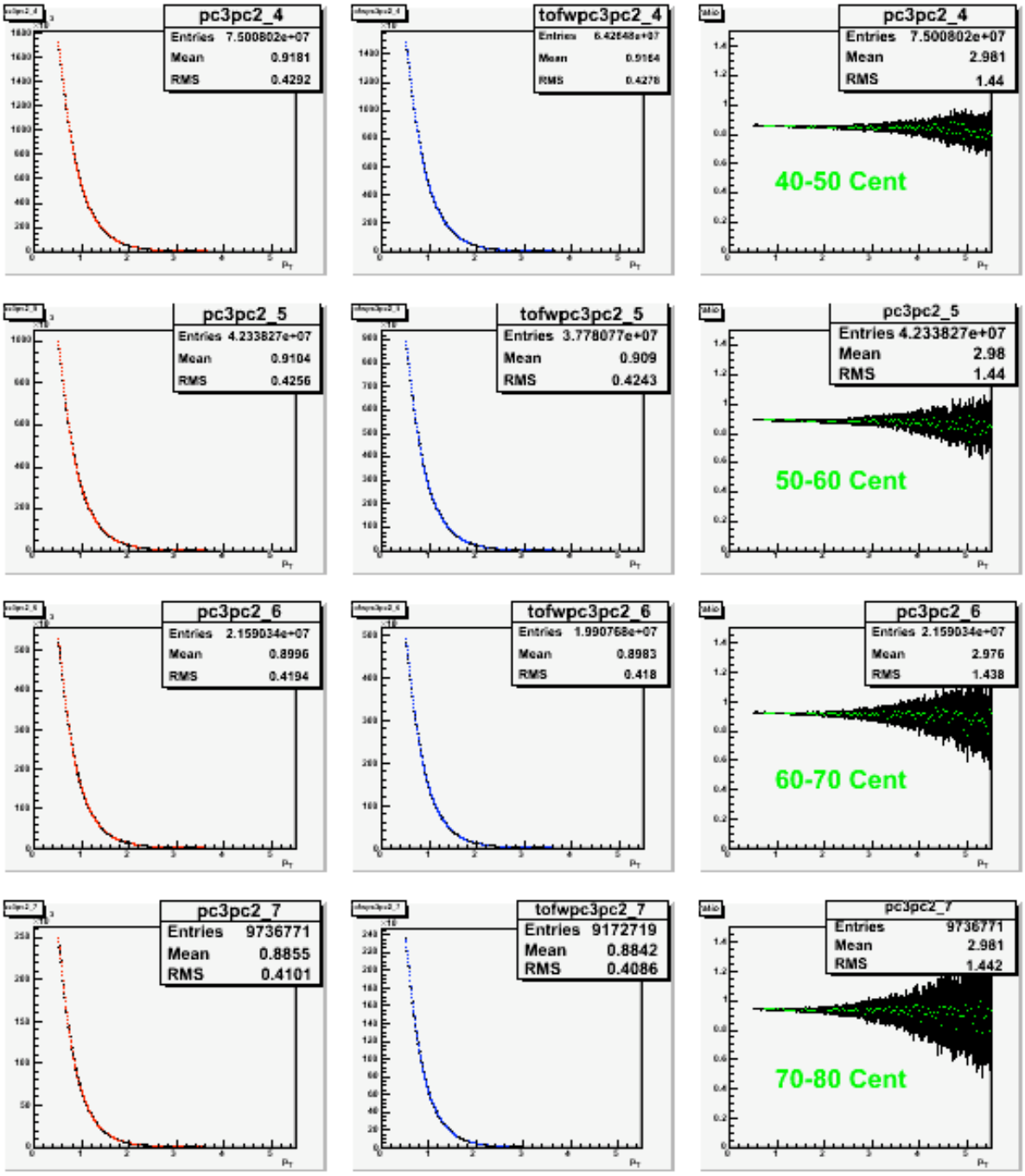

Figure A.8: PC2-PC3 matching histogram (left panel), PC2-PC3-TOF.W matching histograms (middle panel), and the corresponding correction factor (right panel) for 40-50%, 50-60%, 60-70%, and 70-80% centrality bins.

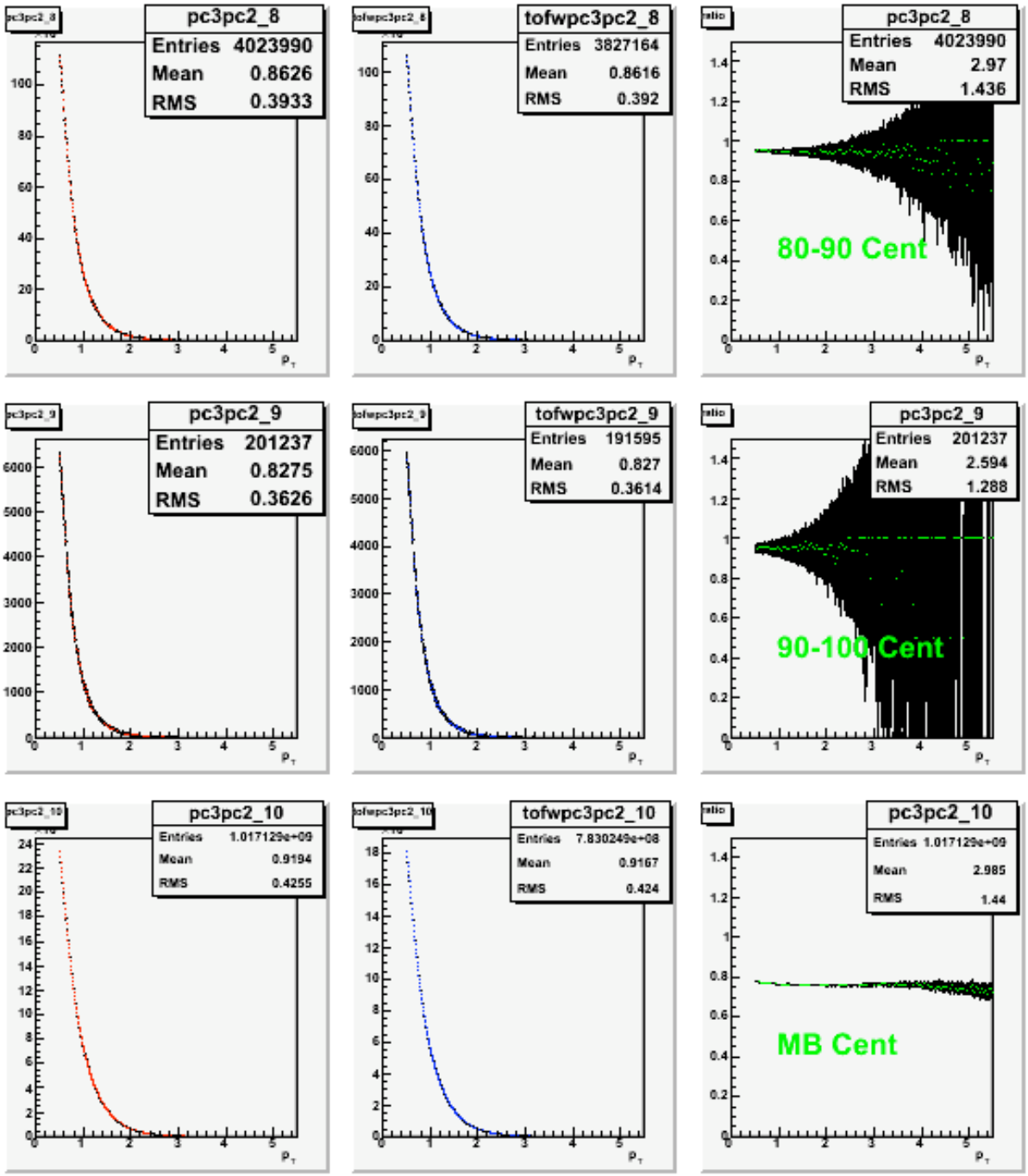

Figure A.9: PC2-PC3 matching histogram (left panel), PC2-PC3-TOF.W matching histograms (middle panel), and the corresponding correction factor (right panel) for 80-90%, 90-100%, and minimum bias centrality bins.

A.1.4 Systematic Error Figures

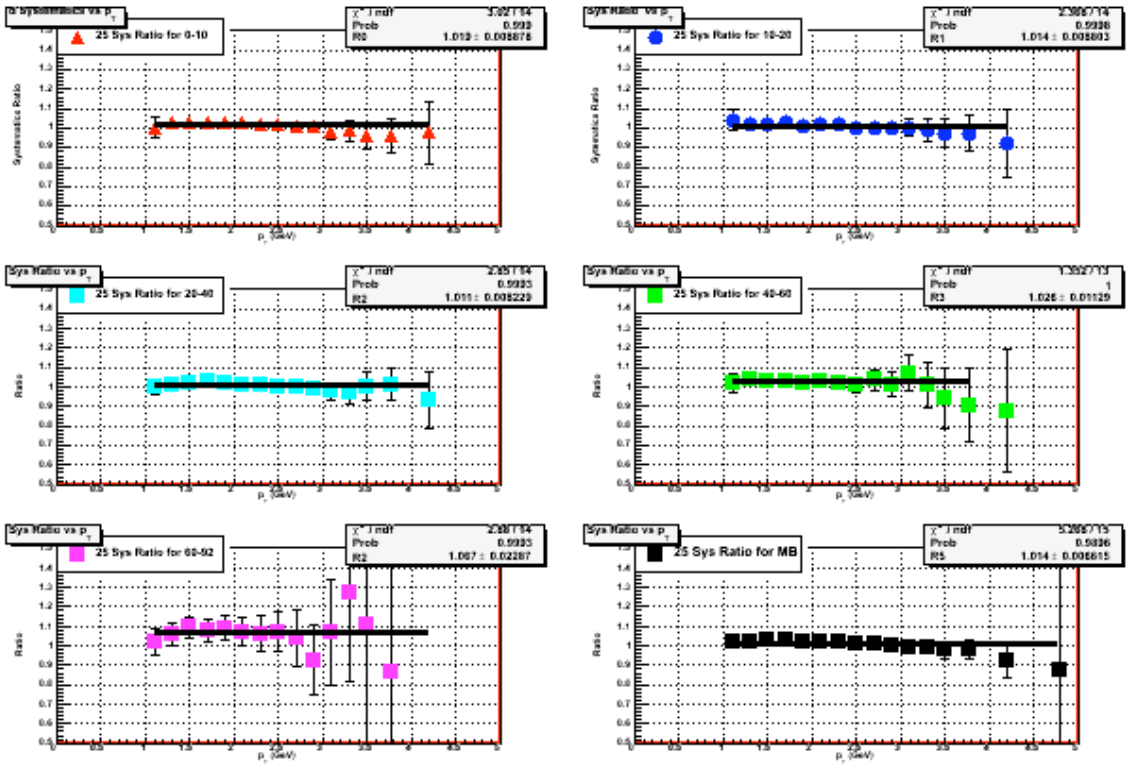

Figure A.10: Systematic error estimate for matching cut. Plotted in the six panels is the ratio of the the two matching cuts used.

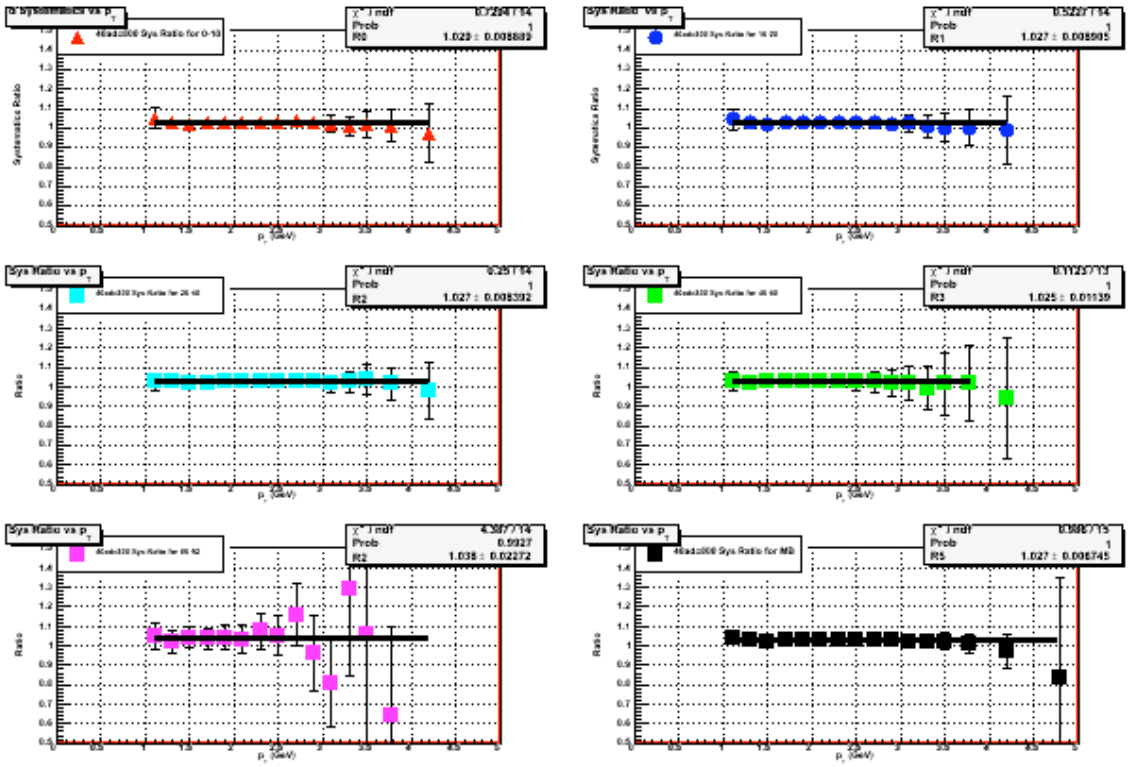

Figure A.11: Systematic error estimate for ADC cut. Plotted in the six panels is the ratio of the the two ADC cuts used.

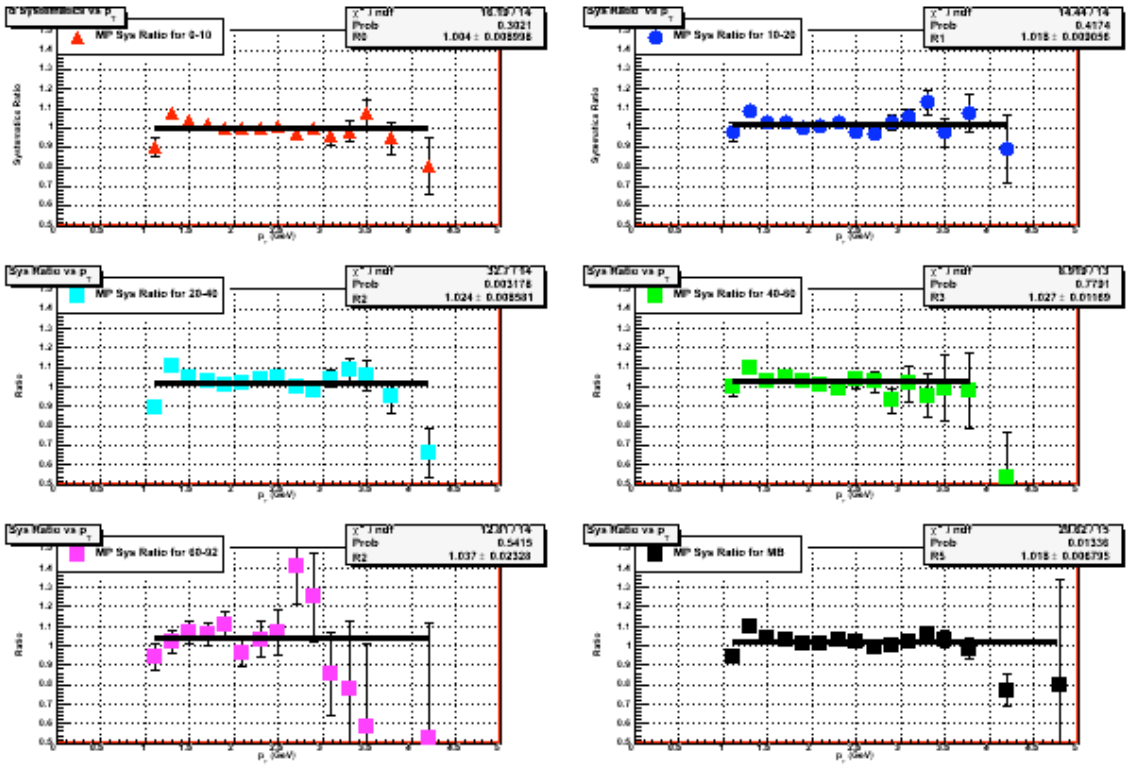

Figure A.12: Systematic error estimate due to magnetic field configuration. Plotted in the six panels is the ratio of the the two magnetic fields used.

A.1.5 dN/dy and $< p_T >$

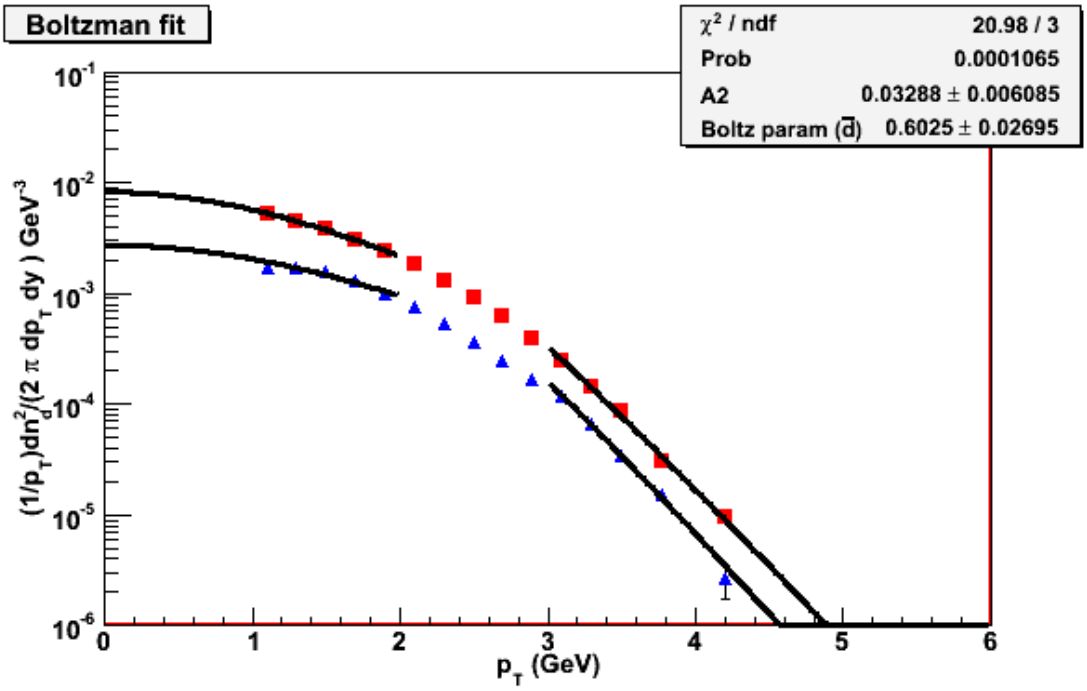

Figure A.13: dN/dy using Boltzmann ratio 10-20% centrality.

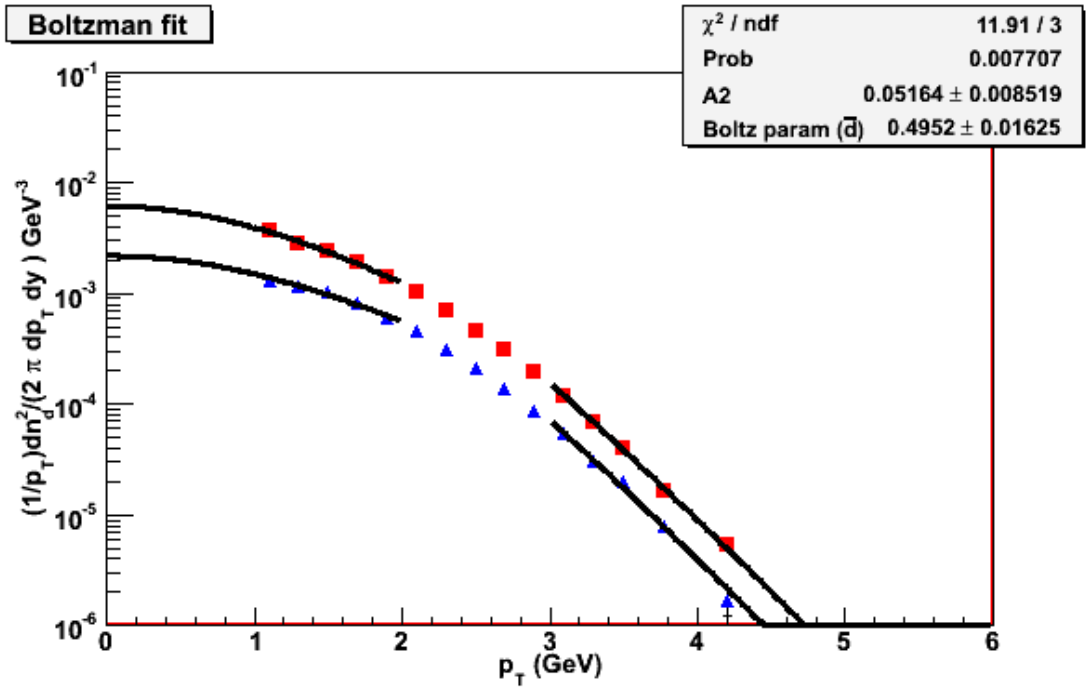

Figure A.14: dN/dy using Boltzmann ratio 20-40% centrality.

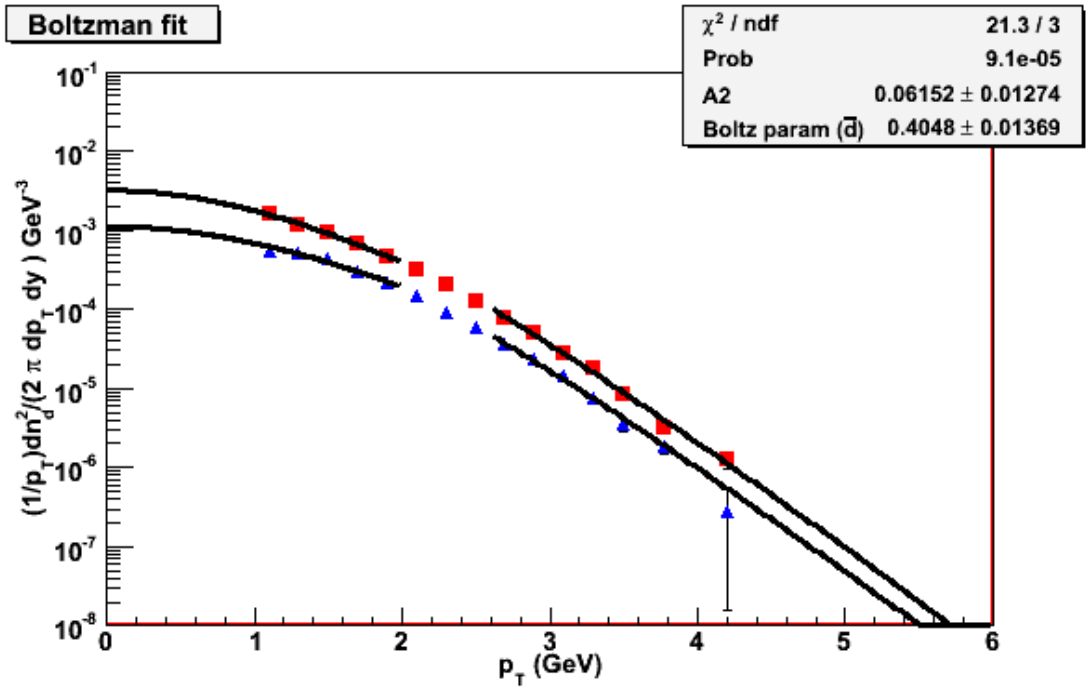

Figure A.15: dN/dy using Boltzmann ratio 40-60% centrality.

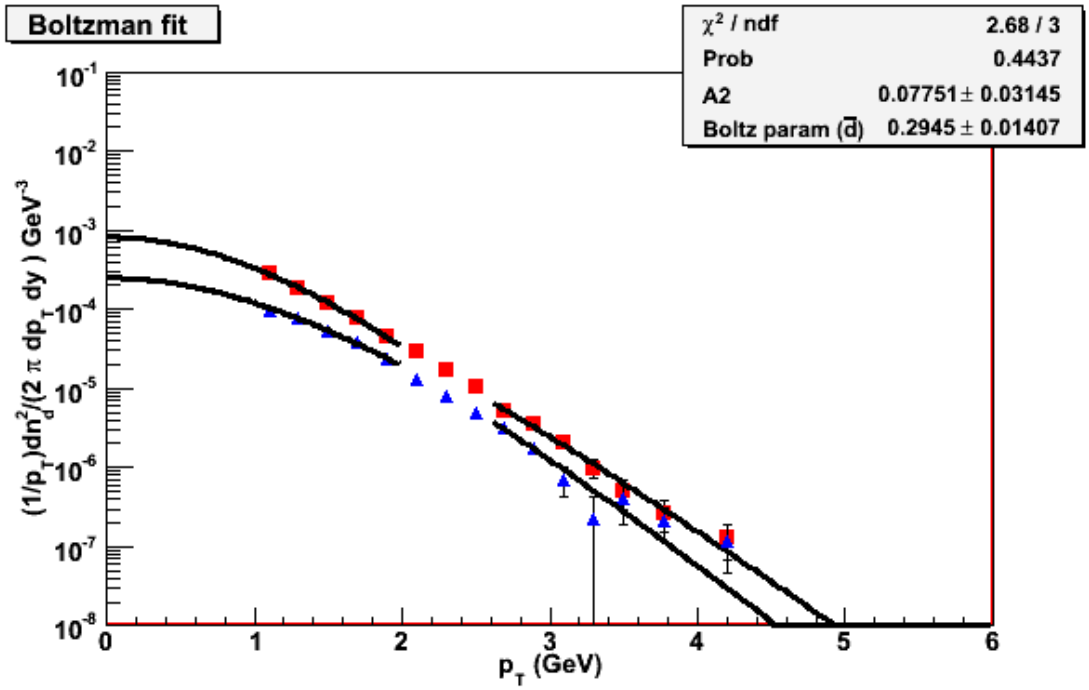

Figure A.16: dN/dy using Boltzmann ratio 60-92% centrality.

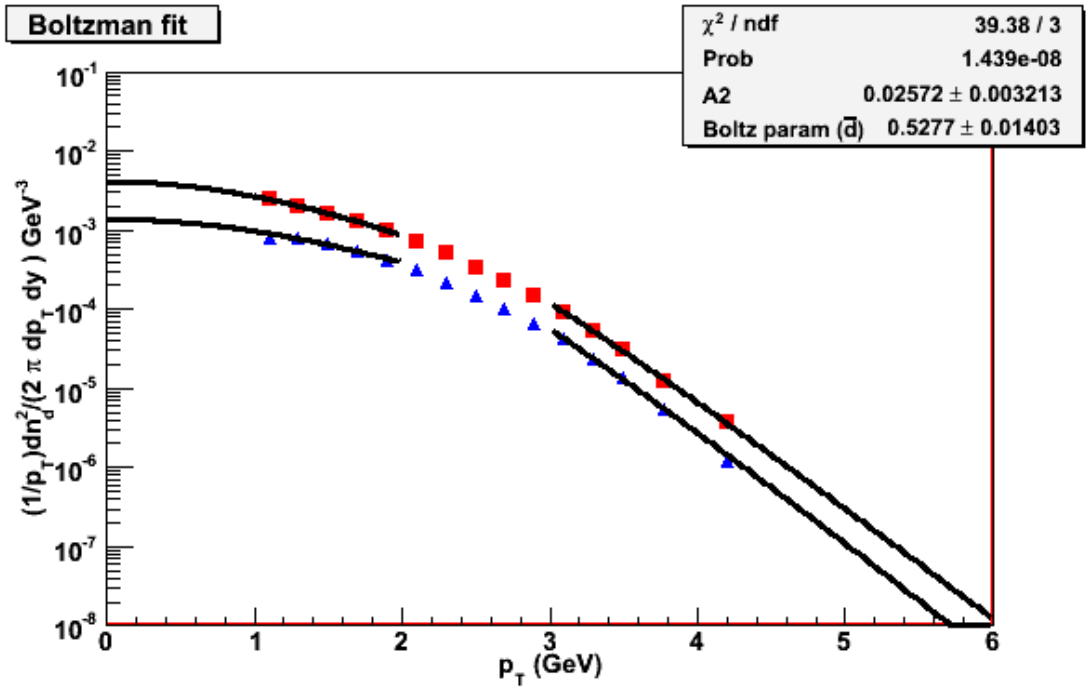

Figure A.17: dN/dy using Boltzmann ratio minimum bias centrality.

A.1.6 Systematic Error for dN/dy and $< p_T >$

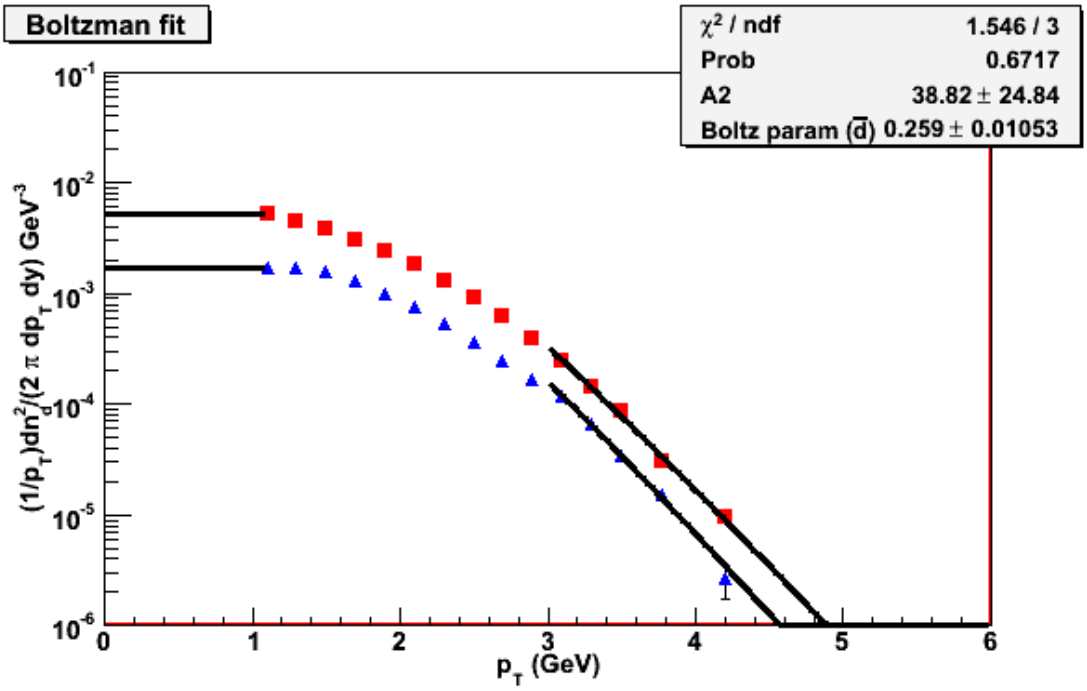

Figure A.18: dN/dy using Boltzmann "flat" ratio 10-20% centrality.

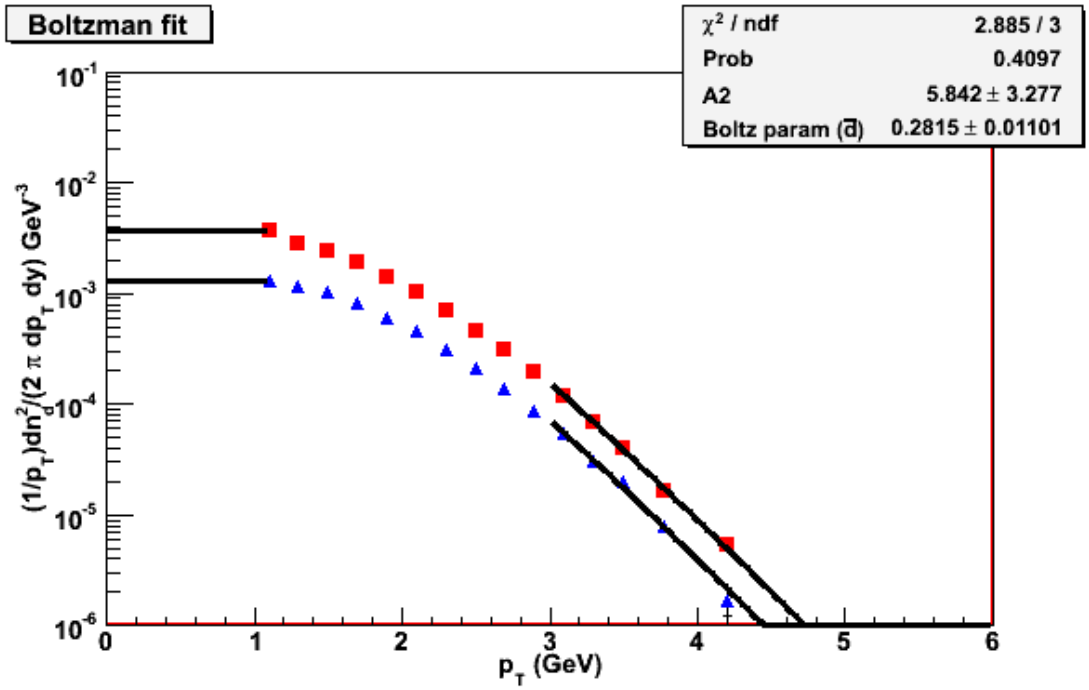

Figure A.19: dN/dy using Boltzmann "flat" ratio 20-40% centrality.

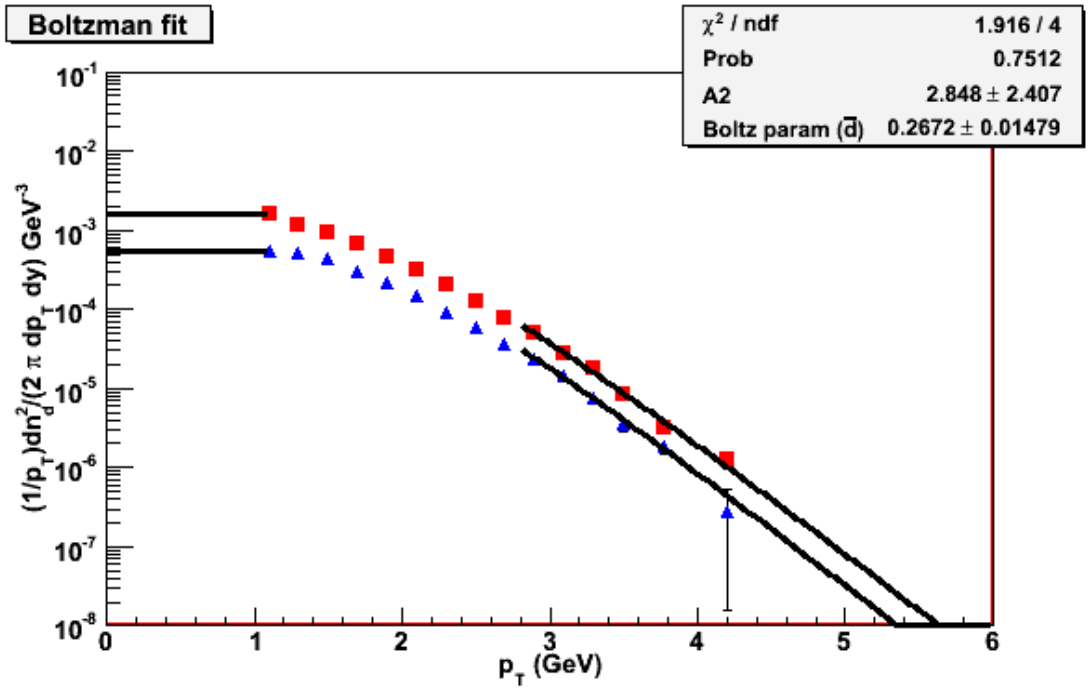

Figure A.20: dN/dy using Boltzmann "flat" ratio 40-60% centrality.

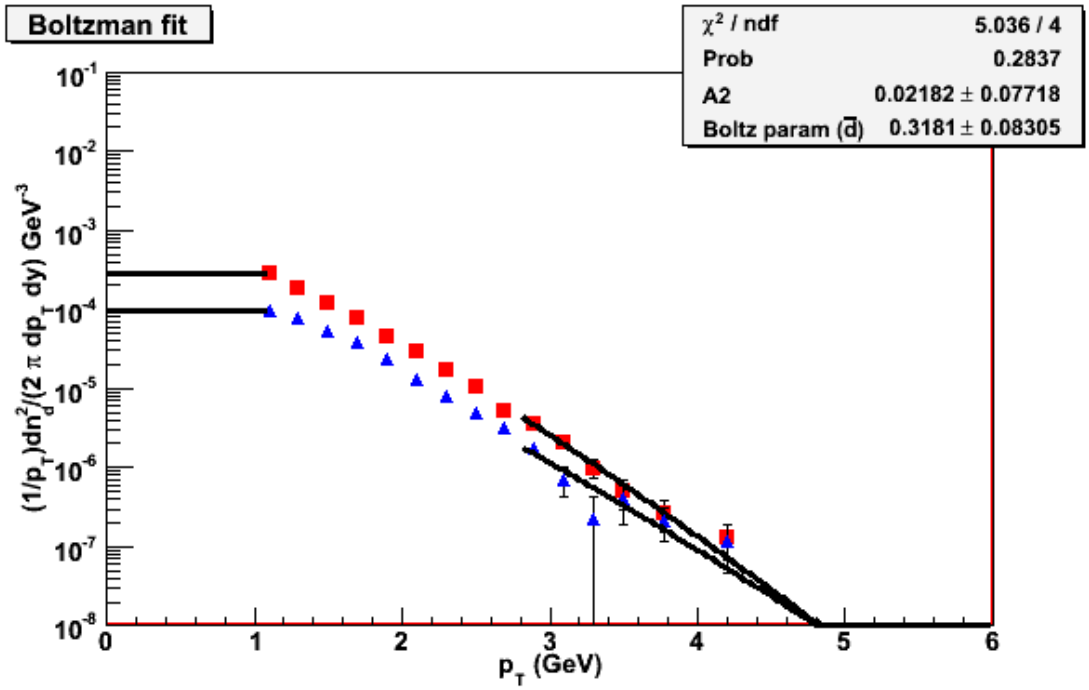

Figure A.21: dN/dy using Boltzmann "flat" ratio 60-92% centrality.

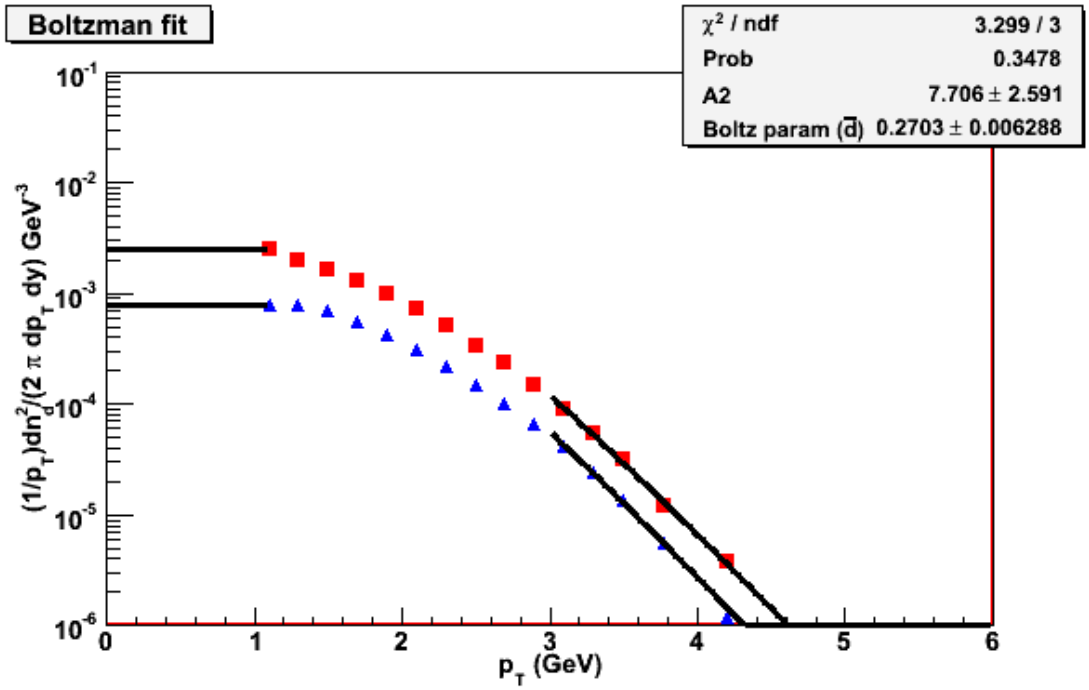

Figure A.22: dN/dy using Boltzmann "flat" ratio minimum bias centrality.

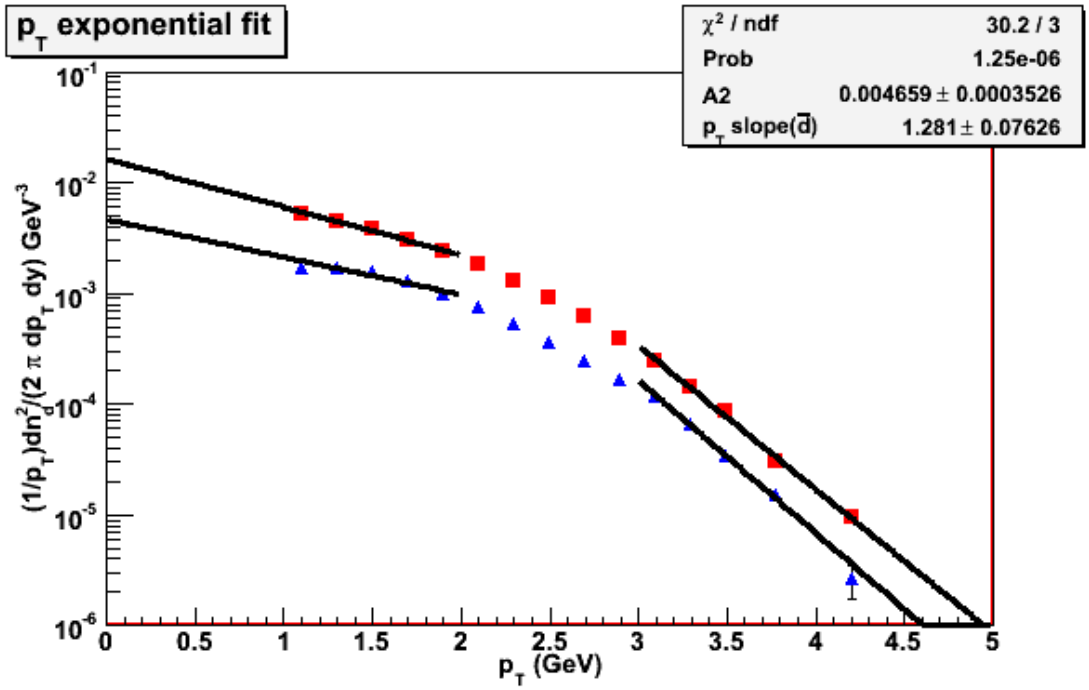

Figure A.23: dN/dy using exponential fit 10-20% centrality.

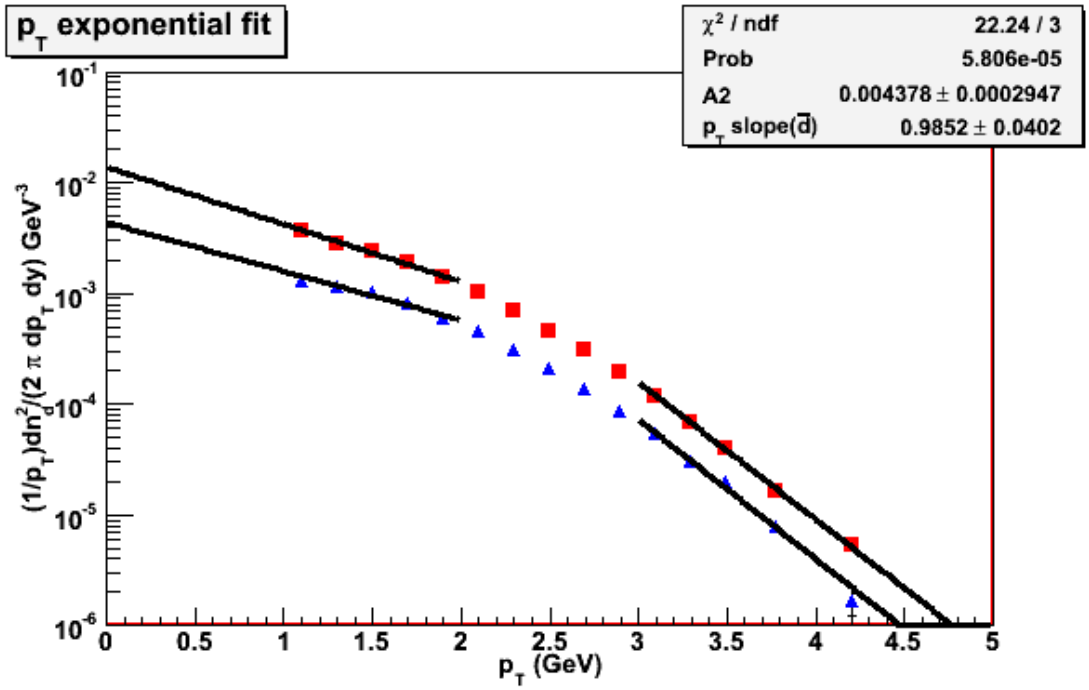

Figure A.24: dN/dy using exponential fit 20-40% centrality.

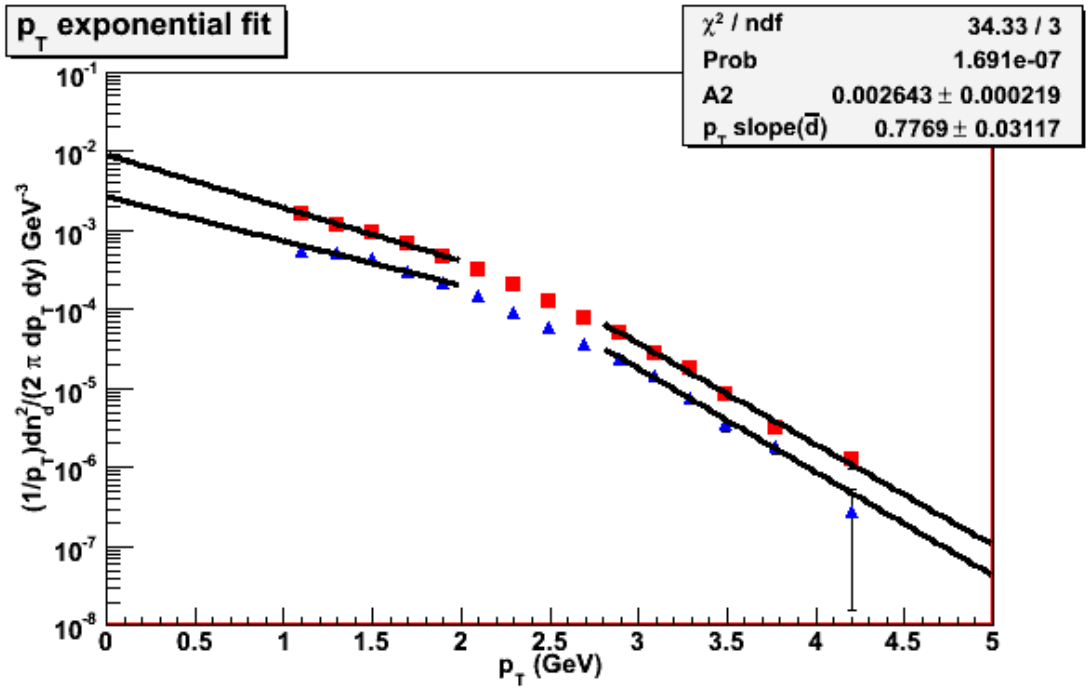

Figure A.25: dN/dy using exponential fit 40-60% centrality.

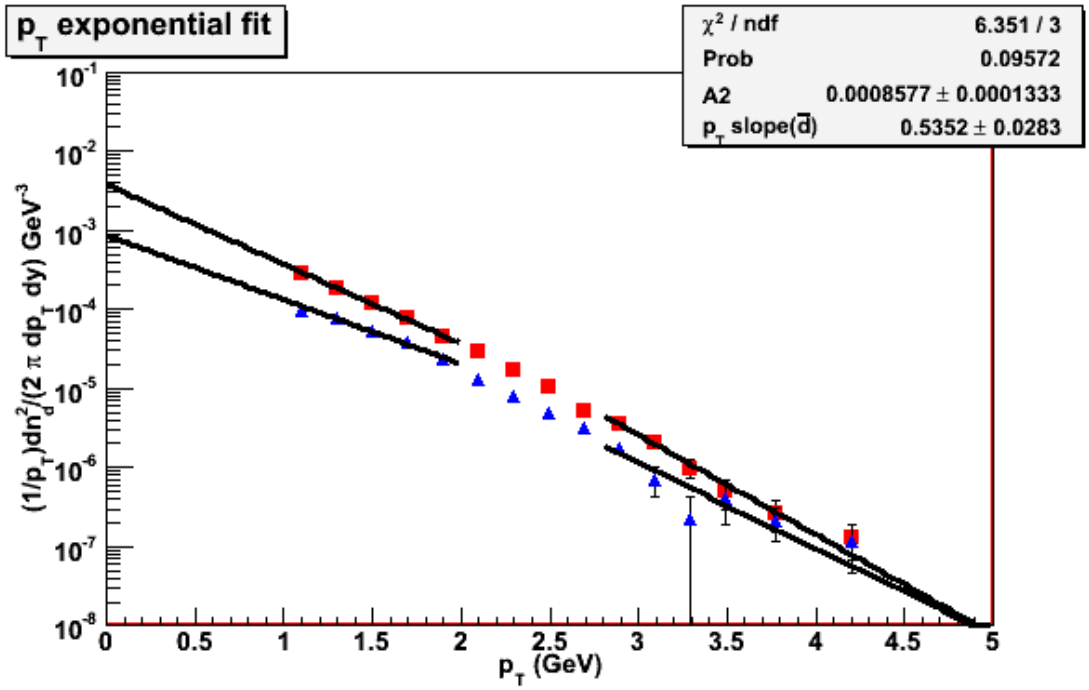

Figure A.26: dN/dy using exponential fit 60-92% centrality.

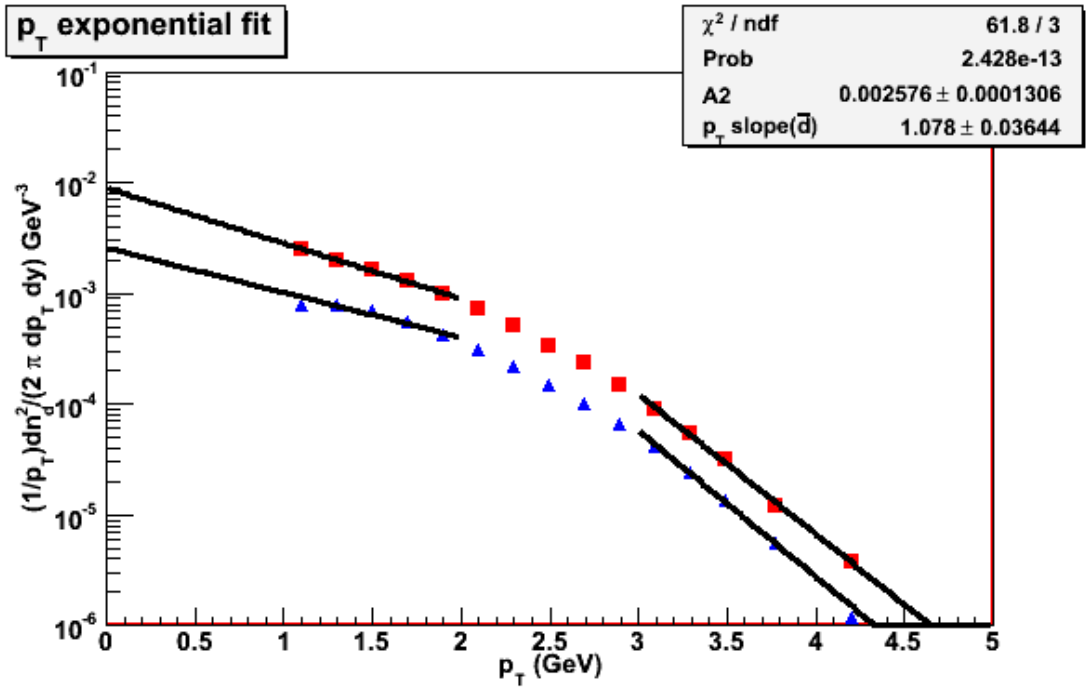

Figure A.27: dN/dy using exponential fit minimum bias centrality.

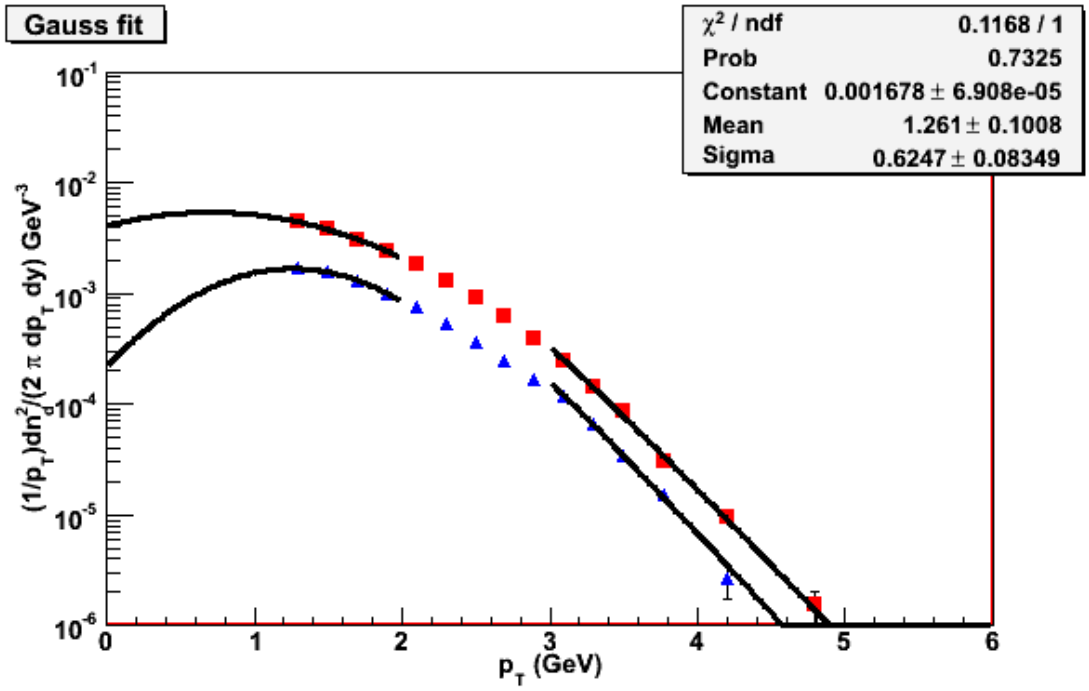

Figure A.28: dN/dy using Gaussian fit 10-20% centrality.

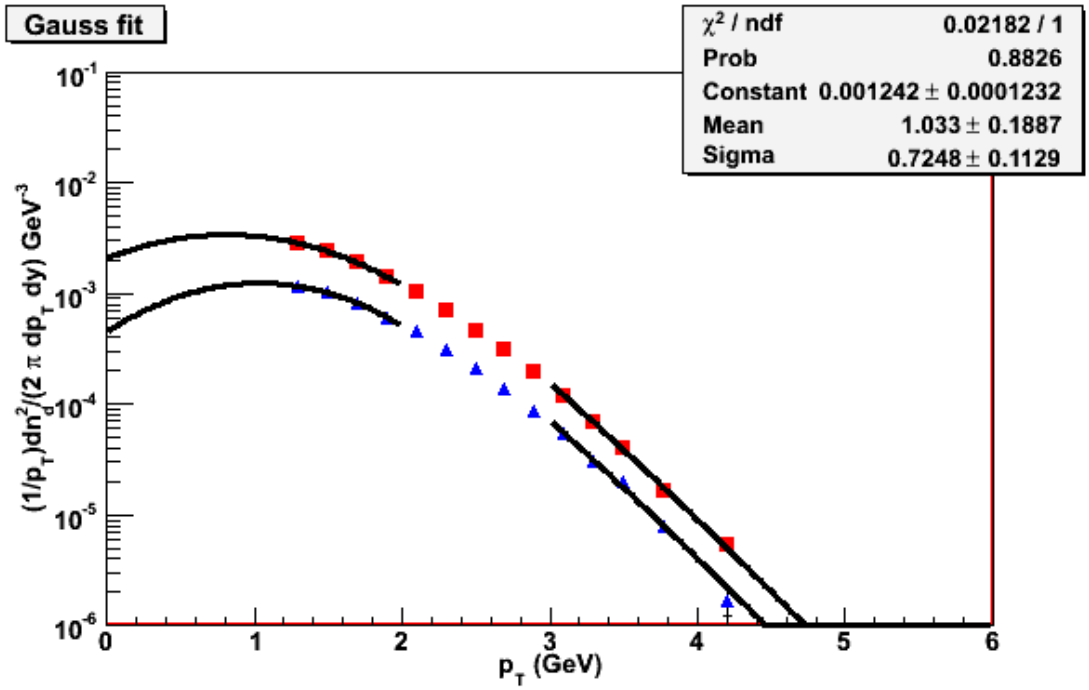

Figure A.29: dN/dy using Gaussian fit 20-40% centrality.

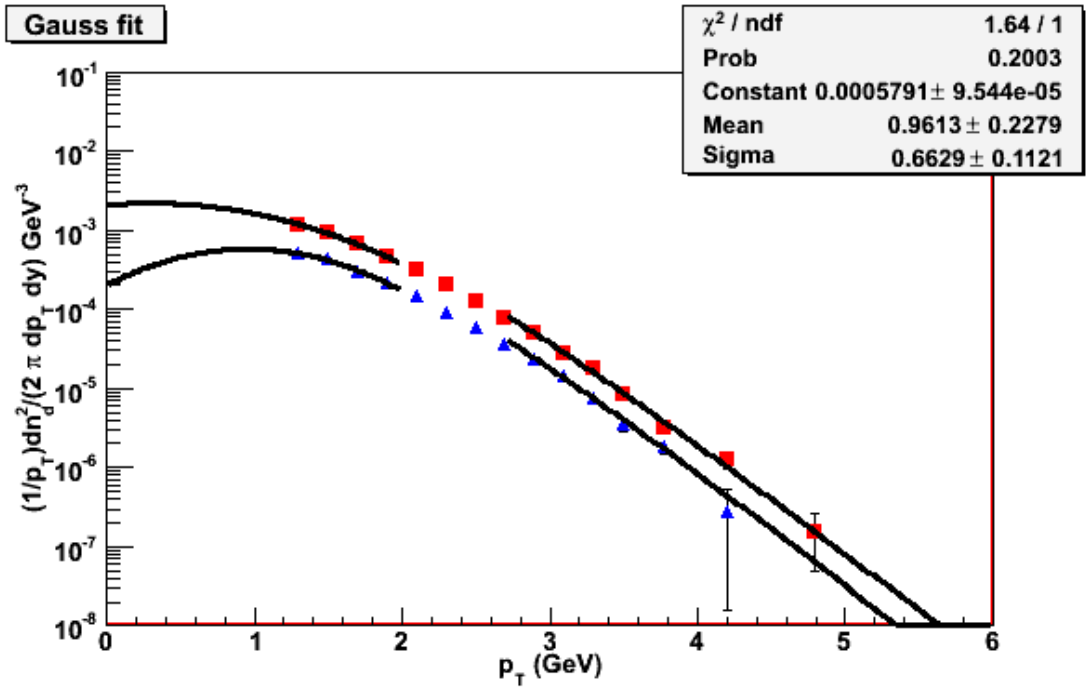

Figure A.30: dN/dy using Gaussian fit 40-60% centrality.

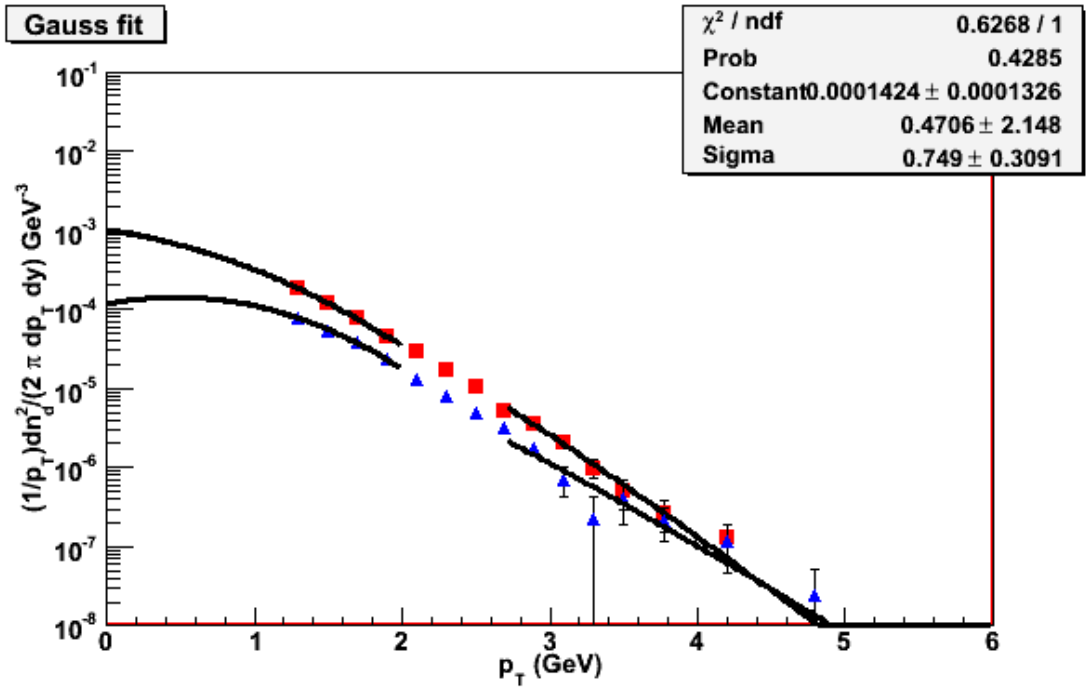

Figure A.31: dN/dy using Gaussian fit 60-92% centrality.

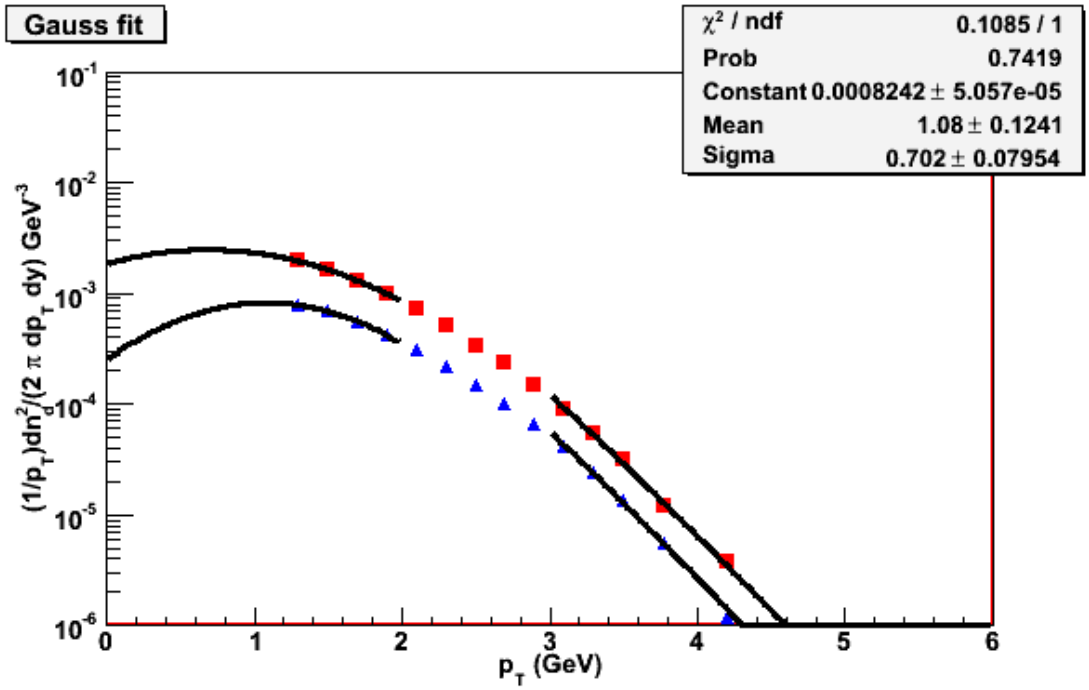

Figure A.32: dN/dy using Gaussian fit minimum bias centrality.

A.1.7 Particle Ratios $\bar{d}/d$

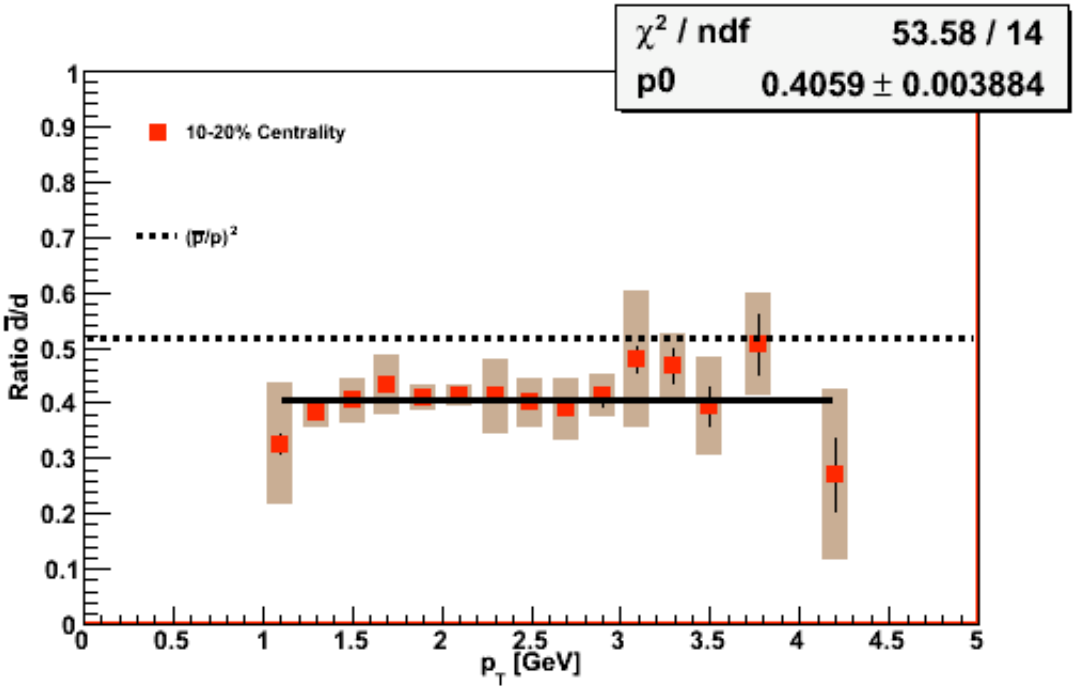

Figure A.33: $\bar{d}/d$ ratio 10-20% centrality.

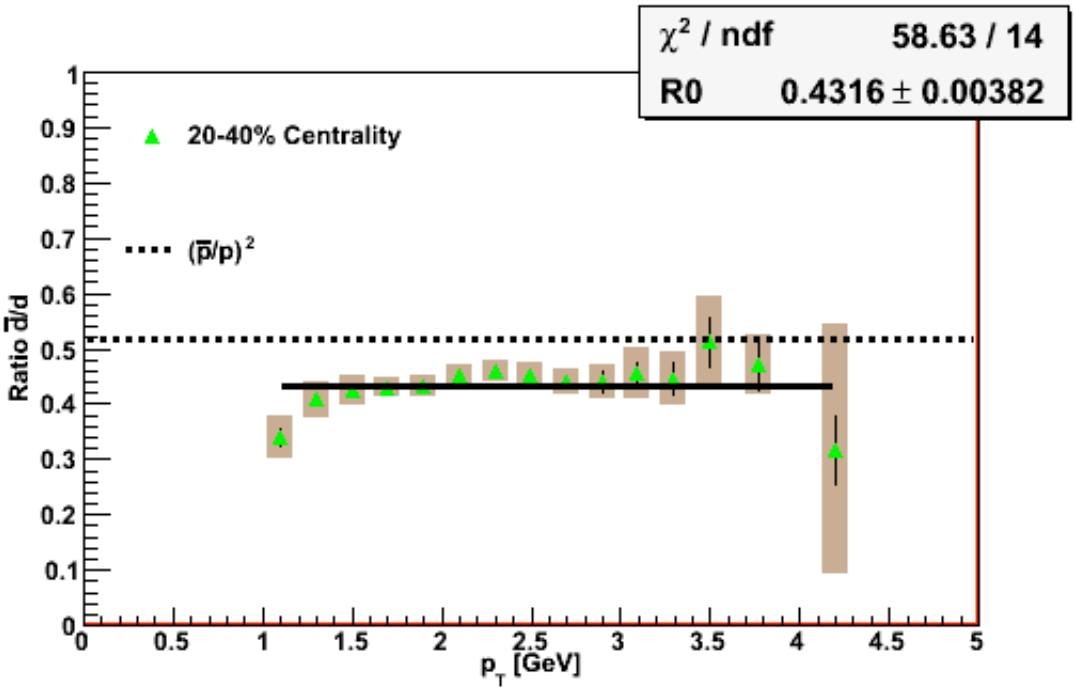

Figure A.34: $\bar{d}/d$ ratio 20-40% centrality.

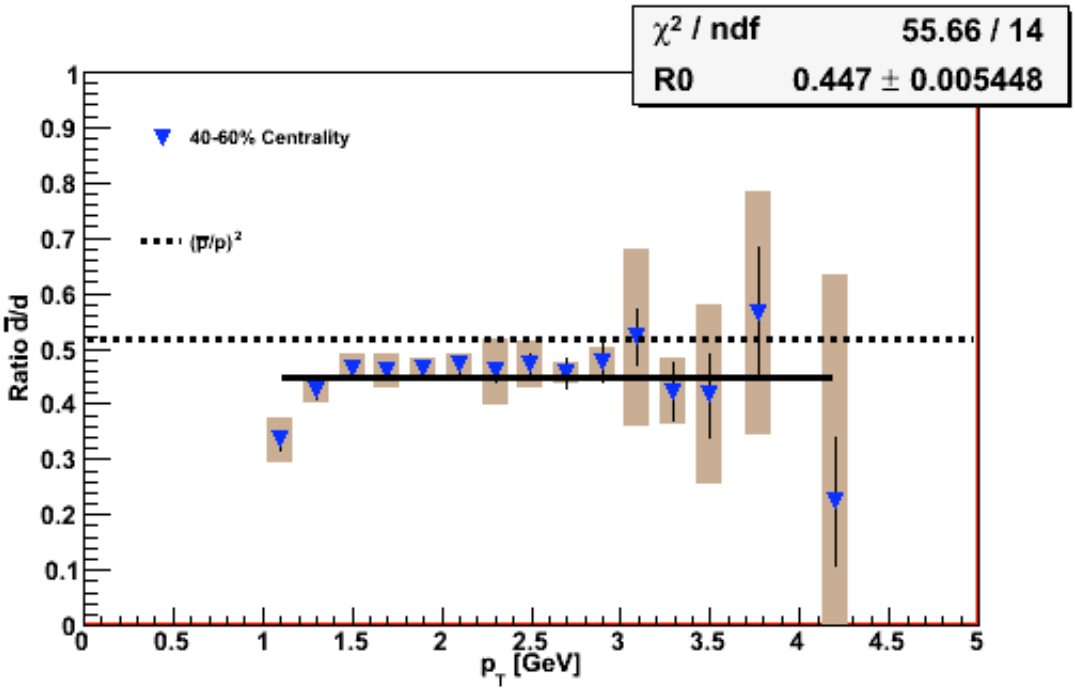

Figure A.35: $\bar{d}/d$ ratio 40-60% centrality.

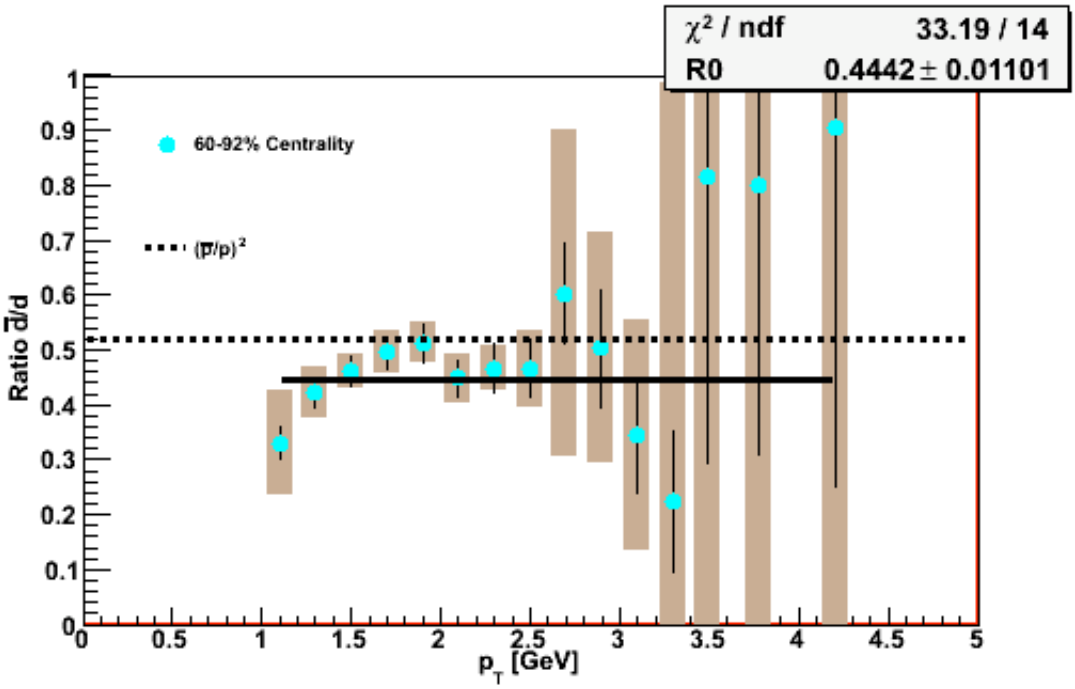

Figure A.36: $\bar{d}/d$ ratio 60-92% centrality.

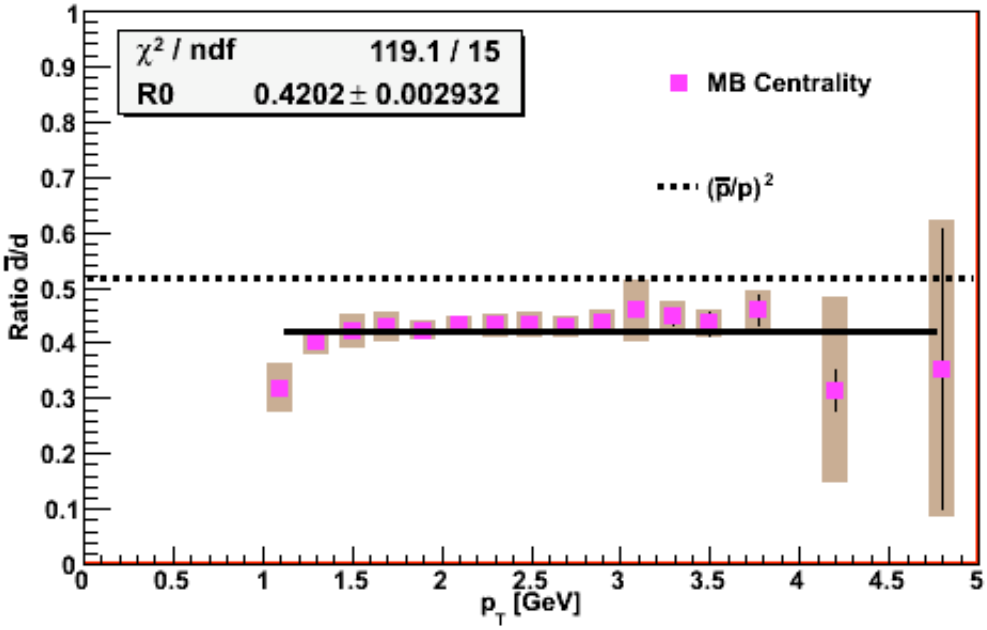

Figure A.37: Minimum bias $\bar{d}/d$ ratio.

A.1.8 Systematic Error on Particle Ratios $\bar{d}/d$

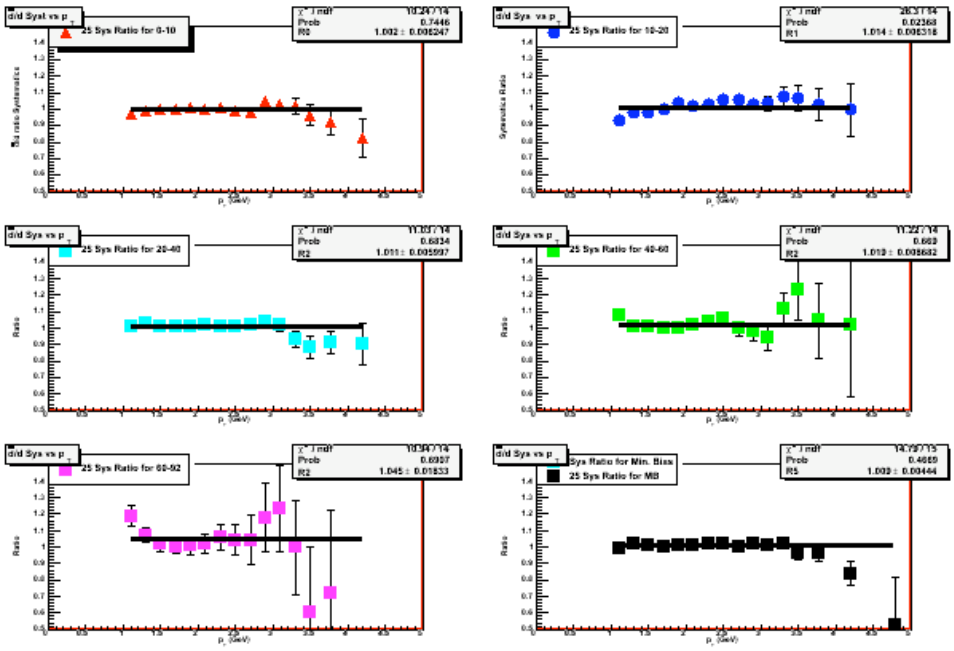

Figure A.38: Systematic error for matching cut.

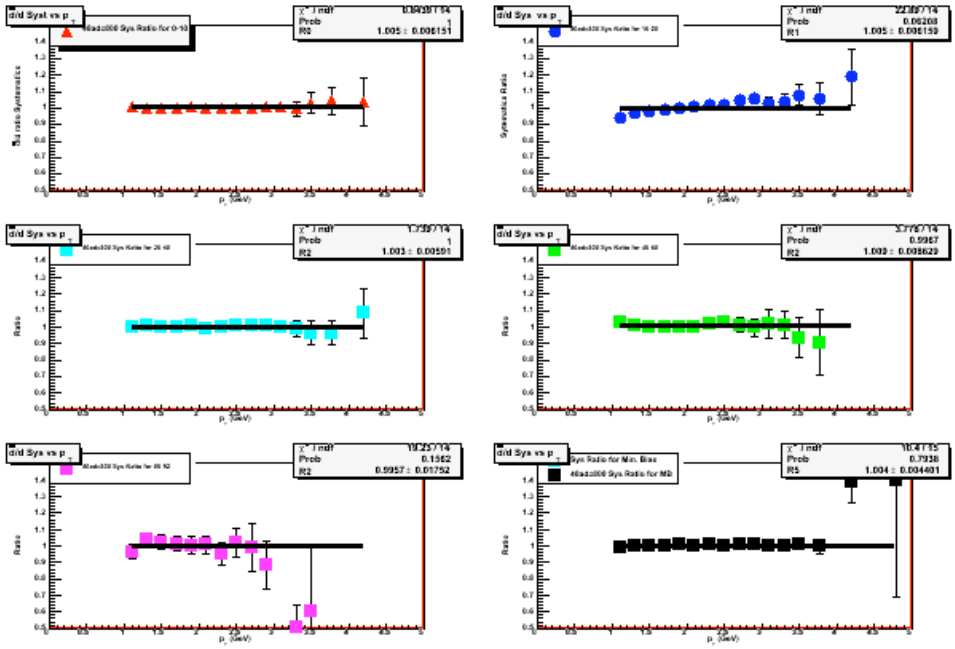

Figure A.39: Systematic error for adc cut.

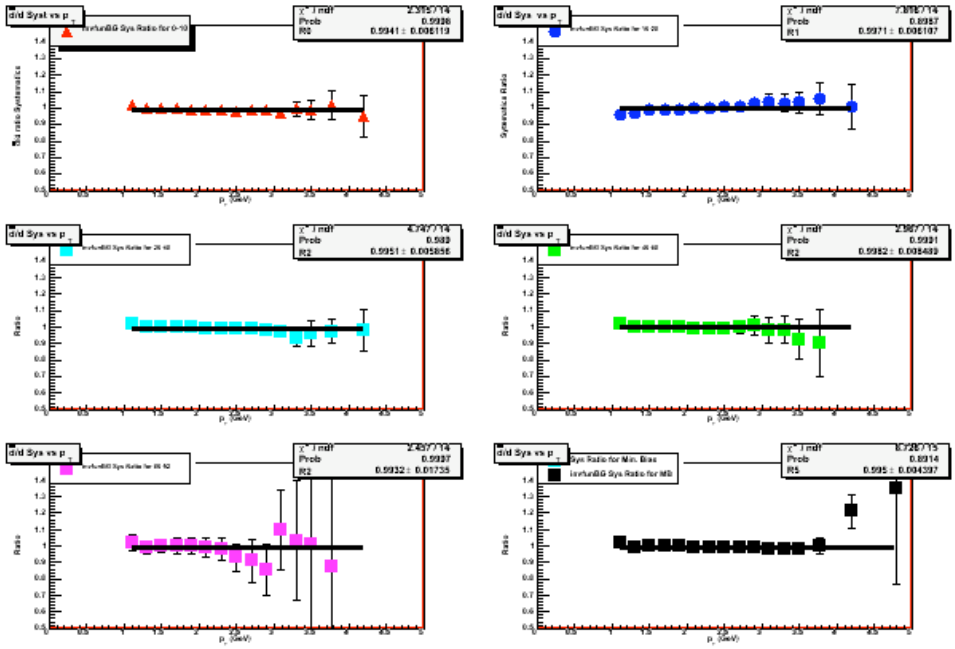

Figure A.40: Systematic error for matching back ground fit.

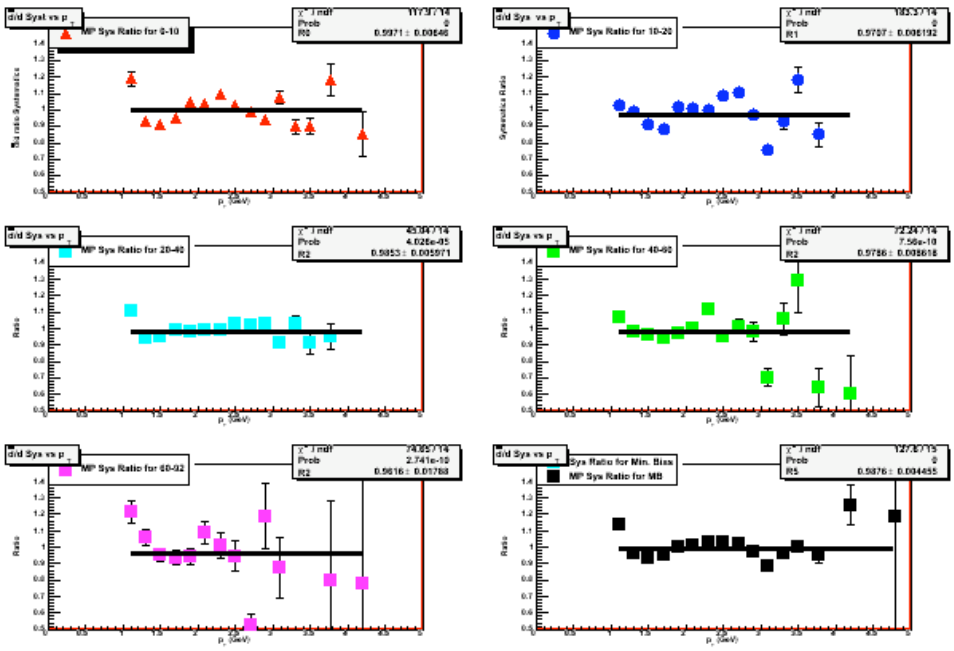

Figure A.41: Systematic error for matching due to magnetic field.

A.2 Tables

A.2.1 Monte Carlo Correction Factors

Table A.1: Single particle Monte Carlo corrections for the -+ Field.

p_T GeV/c	Deuterons	Anti-deuterons
0.9	130.479 $\pm$ 2.30098	217.185 $\pm$ 4.90364
1.10	92.4378 $\pm$ 1.37811	135.648 $\pm$ 2.43257
1.30	80.3859 $\pm$ 1.12093	108.241 $\pm$ 1.7339
1.50	70.4278 $\pm$ 0.923804	88.7468 $\pm$ 1.29544
1.70	65.2815 $\pm$ 0.823155	81.1348 $\pm$ 1.13347
1.90	61.3412 $\pm$ 0.750627	74.8533 $\pm$ 1.00302
2.10	59.2078 $\pm$ 0.713395	71.4228 $\pm$ 0.937891
2.30	56.8129 $\pm$ 0.672355	68.813 $\pm$ 0.888533
2.50	54.6452 $\pm$ 0.634163	65.7246 $\pm$ 0.82977
2.70	53.3164 $\pm$ 0.61331	64.053 $\pm$ 0.799748
2.90	52.0181 $\pm$ 0.590389	62.028 $\pm$ 0.76108
3.10	51.1751 $\pm$ 0.5752	60.6154 $\pm$ 0.73627
3.30	49.5816 $\pm$ 0.547914	60.418 $\pm$ 0.731129
3.50	49.3949 $\pm$ 0.546352	58.9377 $\pm$ 0.70683
3.80	48.9704 $\pm$ 0.381624	56.9966 $\pm$ 0.47471
4.25	47.4294 $\pm$ 0.325678	57.1447 $\pm$ 0.42720
5.00	46.7282 $\pm$ 0.225242	55.0591 $\pm$ 0.28559

A.2.2 Tracking Efficiency

Table A.2: Multiplicity dependence for DC-PC1 and DC-PC1-PC2-PC3.

centrality	**dc-pc1(%)**	**dc-pc1-pc2-pc3 (%)**	Syst. error (%)
Min. bias	97.2	80.7	2
0 – 10%	95.9	72.2	4
10 – 20%	97.4	80.6	4
20 – 30%	98.3	88.1	3
30 – 40%	99.0	90.8	3
40 – 50%	99.1	95.0	3
50 – 60%	99.7	96.6	3
60 – 70%	99.6	97.6	2
70 – 80%	99.8	99.8	2
80 – 92%	99.8	99.7	2

Table A.3: Tracking efficiency for protons.

centrality	**proton**	**proton** (including MRPC Eff(90%))
0 – 10%	0.815399 ± 0.02347	0.734391
10 – 20%	0.889626 ± 0.02978	0.800663
20 – 40%	0.941619 ± 0.02522	0.847457
40 – 60%	0.964802 ± 0.023396	0.868322
60 – 92%	0.987403 ± 0.03651	0.888663
Min. bias	0.877183 ± 0.027788	0.789465

A.2.3 Survival Probability

Table A.4: Hadronic survival probability calculation with PISA for anti-protons.

p_T GeV/c	Ratio(Hadronic ON/Hadronic OFF)
0.50-0.75	66.7472 $\pm$3.0353
0.75-1.00	74.2368 $\pm$1.50336
1.00-1.25	77.5367 $\pm$1.17628
1.25-1.50	79.7162 $\pm$1.00348
1.50-1.75	81.3008 $\pm$0.942811
1.75-2.00	82.5842 $\pm$0.906729
2.00-2.25	83.7533 $\pm$0.885358
2.25-2.50	83.4331 $\pm$1.00566

Table A.5: Hadronic survival probability (Stand-alone) calculation for (Anti-)Deuterons.

p_T GeV/c	Deuterons[$\%$]	Anti-deuterons[$\%$]
1.00-1.50	89.3782	86.7075
1.50-2.00	89.3735	86.8014
2.00-2.50	89.3691	86.9393
2.50-3.00	89.3669	87.079
3.00-3.50	89.3659	87.2052
3.50-4.00	89.3655	87.3203
4.00-4.50	89.3654	87.4202
4.50-5.00	89.3654	87.5087

A.2.4 Systematic Error on Spectra

Table A.6: p_T dependent absolute systematic errors from different sources, added in quadrature for 20-40% and 40-60% at the mean of the p_T bin for all centrality classes.

Centrality	p_T GeV/c	Deuterons	Anti-deuterons
20-40%	1.10086	0.000463002	8.78776e-05
	1.30029	0.0003473	9.28463e-05
	1.49971	0.000155169	5.45629e-05
	1.69914	0.000102114	4.2832e-05
	1.89857	5.88411e-05	2.90815e-05
	2.09799	4.343e-05	2.23727e-05
	2.29742	3.93231e-05	1.8326e-05
	2.49685	2.98785e-05	2.14521e-05
	2.69628	1.26844e-05	8.41308e-06
	2.8957	1.07907e-05	7.22732e-06
	3.09513	7.71706e-06	4.76402e-06
	3.29456	7.43794e-06	5.98466e-06
	3.49399	3.56384e-06	3.16218e-06
	3.77288	1.16134e-06	1.14954e-06
	4.20045	2.04189e-06	4.03771e-07
	4.78034	8.21912e-07	8.04303e-07
40-60%	1.10086	8.451e-05	8.47556e-05
	1.30029	0.000146951	5.64844e-05
	1.49971	5.09195e-05	2.36666e-05
	1.69914	4.8224e-05	1.52073e-05
	1.89857	2.45021e-05	9.56297e-06
	2.09799	1.41748e-05	9.88751e-06
	2.29742	7.69236e-06	1.37536e-05
	2.49685	6.81591e-06	6.32215e-06
	2.69628	5.15789e-06	2.7884e-06
	2.8957	4.9773e-06	2.52488e-06
	3.09513	3.13927e-06	4.90112e-06
	3.29456	1.73589e-06	1.32252e-06
	3.49399	8.35396e-07	1.41166e-06
	3.77288	4.53489e-07	8.61209e-07
	4.20045	6.69447e-07	5.49012e-07
	4.78034	9.44291e-08	4.85127e-07

Table A.7: p_T dependent absolute systematic errors from different sources, added in quadrature for 60-92% and minimum bias at the mean of the p_T bin for all centrality classes.

Centrality	p_T GeV/c	Deuterons	Anti-deuterons
60-92%	1.10086	2.6911e-05	2.75627e-05
	1.30029	1.45916e-05	1.47846e-05
	1.49971	1.65511e-05	8.09746e-06
	1.69914	9.06737e-06	4.17303e-06
	1.89857	7.43503e-06	3.02046e-06
	2.09799	2.71976e-06	1.61415e-06
	2.29742	1.97928e-06	1.20139e-06
	2.49685	1.41556e-06	9.65261e-07
	2.69628	2.53745e-06	1.1791e-06
	2.8957	1.0343e-06	1.17029e-06
	3.09513	7.97598e-07	3.74107e-07
	3.29456	5.20255e-07	6.00062e-07
	3.49399	2.41506e-07	5.92564e-07
	3.77288	2.14055e-07	1.38987e-07
	4.20045	1.51183e-07	1.20334e-07
	4.78034	1.63362e-08	5.90287e-08
MB	1.10086	0.00023113	8.13635e-05
	1.30029	0.000232605	6.74033e-05
	1.49971	0.000105725	3.97334e-05
	1.69914	7.47823e-05	3.19482e-05
	1.89857	4.21729e-05	2.43801e-05
	2.09799	3.08494e-05	1.82371e-05
	2.29742	2.48833e-05	1.83441e-05
	2.49685	1.51622e-05	1.16051e-05
	2.69628	1.0463e-05	5.84184e-06
	2.8957	6.56348e-06	4.77286e-06
	3.09513	4.85475e-06	5.22236e-06
	3.29456	4.10827e-06	1.53465e-06
	3.49399	1.90641e-06	1.34793e-06
	3.77288	6.37887e-07	6.08412e-07
	4.20045	1.16026e-06	6.2945e-07
	4.78034	1.60168e-07	9.97815e-8

A.2.5 Spectra and Yields

Table A.8: Corrected yields for 0-10% and 10-20% at the mean of the p_T bin for all centrality classes.

Centrality	p_T GeV/c	Ed^3N/dp^3 (deuterons)	Ed^3N/dp^3 (anti-deuterons)
0-10%	1.10079	0.00718056 ± 0.000254636	0.00207007 ± 0.000116127
	1.30026	0.00576822 ± 0.000129275	0.00226384 ± 7.60567e-05
	1.49974	0.0050713 ± 9.93907e-05	0.0020694 ± 5.63987e-05
	1.69921	0.00425808 ± 7.74691e-05	0.00171467 ± 4.29067e-05
	1.89868	0.00339587 ± 5.97478e-05	0.00134574 ± 3.25063e-05
	2.09815	0.00258517 ± 4.55855e-05	0.00105035 ± 2.51573e-05
	2.29762	0.00188746 ± 3.50125e-05	0.000753063 ± 1.91021e-05
	2.49709	0.00128234 ± 2.58614e-05	0.000541331 ± 1.47161e-05
	2.69657	0.000918474 ± 2.04898e-05	0.000394391 ± 1.29899e-05
	2.89604	0.000599867 ± 1.4465e-05	0.000257978 ± 1.06705e-05
	3.09551	0.000365335 ± 1.08403e-05	0.000152387 ± 7.47921e-06
	3.29498	0.000222776 ± 8.1561e-06	9.75827e-05 ± 5.83777e-06
	3.49446	0.000135855 ± 6.37275e-06	5.35415e-05 ± 4.7827e-06
	3.77494	5.17069e-05 ± 2.92104e-06	1.89255e-05 ± 2.87333e-06
	4.20413	1.60157e-05 ± 1.70447e-06	6.43764e-06 ± 1.38326e-06
	4.79342	4.32006e-08 ± 3.08404e-07	5.00398e-07 ± 5.69672e-07
10-20%	1.10079	0.00587476 ± 0.000203299	0.00191314 ± 9.37552e-05
	1.30026	0.00487868 ± 0.00010526	0.00186625 ± 5.9192e-05
	1.49974	0.00426358 ± 8.19075e-05	0.00172236 ± 4.45893e-05
	1.69921	0.00338214 ± 6.16462e-05	0.00146498 ± 3.45016e-05
	1.89868	0.00269064 ± 4.71797e-05	0.00110523 ± 2.57941e-05
	2.09815	0.00203265 ± 3.56942e-05	0.000837611 ± 1.99874e-05
	2.29762	0.0014582 ± 2.7276e-05	0.00060032 ± 1.50733e-05
	2.49709	0.0010198 ± 2.02978e-05	0.00040843 ± 1.13352e-05
	2.69657	0.000699834 ± 1.54524e-05	0.000272199 ± 9.61225e-06
	2.89604	0.000441526 ± 1.17818e-05	0.000182058 ± 7.68997e-06
	3.09551	0.000277434 ± 8.2745e-06	0.000132404 ± 6.65275e-06
	3.29498	0.000156449 ± 6.04709e-06	7.29929e-05 ± 4.84098e-06
	3.49446	9.52514e-05 ± 4.79844e-06	3.74676e-05 ± 3.52404e-06
	3.77494	3.35117e-05 ± 2.17909e-06	1.69332e-05 ± 1.77678e-06
	4.20413	1.07617e-05 ± 1.33809e-06	2.90995e-06 ± 9.76228e-07
	4.79342	1.73484e-06 ± 5.60504e-07	7.7396e-07 ± 6.18009e-07

Table A.9: Corrected yields for 20-40% and 40-60% at the mean of the p_T bin for all centrality classes.

Centrality	p_T GeV/c	Ed^3N/dp^3 (Deuterons)	Ed^3N/dp^3 (Anti-deuterons)
20-40%	1.10079	0.00416974 ± 0.000117153	0.00141833 ± 6.51464e-05
	1.30026	0.00316181 ± 6.17133e-05	0.00128843 ± 3.31833e-05
	1.49974	0.00264941 ± 4.73564e-05	0.00112452 ± 2.51252e-05
	1.69921	0.00210286 ± 3.58373e-05	0.000903037 ± 1.87944e-05
	1.89868	0.00156511 ± 2.58892e-05	0.00067689 ± 1.3811e-05
	2.09815	0.00112692 ± 1.8902e-05	0.000507386 ± 1.06687e-05
	2.29762	0.000763854 ± 1.3409e-05	0.000350001 ± 7.97973e-06
	2.49709	0.000508749 ± 9.82166e-06	0.000230441 ± 5.7373e-06
	2.69657	0.000341009 ± 7.32462e-06	0.000150194 ± 4.2932e-06
	2.89604	0.000217946 ± 5.6636e-06	9.60732e-05 ± 3.69125e-06
	3.09551	0.000132982 ± 3.92222e-06	6.03936e-05 ± 3.00341e-06
	3.29498	7.65879e-05 ± 2.87998e-06	3.41175e-05 ± 2.45244e-06
	3.49446	4.38124e-05 ± 2.22142e-06	2.24315e-05 ± 2.09689e-06
	3.77494	1.84084e-05 ± 1.04852e-06	8.64633e-06 ± 8.04386e-07
	4.20413	5.9148e-06 ± 6.02122e-07	1.88247e-06 ± 5.09789e-07
	4.79342	9.98792e-07 ± 2.83717e-07	5.85393e-07 ± 2.27901e-07
40-60%	1.10079	0.00175778 ± 5.77525e-05	0.000588857 ± 3.30764e-05
	1.30026	0.00132056 ± 3.21162e-05	0.000558905 ± 1.76212e-05
	1.49974	0.00102211 ± 2.16627e-05	0.000473881 ± 1.29618e-05
	1.69921	0.000734603 ± 1.53924e-05	0.000338499 ± 9.31787e-06
	1.89868	0.00051563 ± 1.08833e-05	0.00023874 ± 6.77713e-06
	2.09815	0.000346458 ± 7.72215e-06	0.000162906 ± 4.96715e-06
	2.29762	0.000223657 ± 5.47576e-06	0.00010265 ± 3.6044e-06
	2.49709	0.000139788 ± 3.92697e-06	6.58795e-05 ± 2.65009e-06
	2.69657	8.67964e-05 ± 3.12436e-06	3.95693e-05 ± 1.98889e-06
	2.89604	5.47869e-05 ± 2.47176e-06	2.61023e-05 ± 1.87356e-06
	3.09551	3.12162e-05 ± 1.92398e-06	1.62342e-05 ± 1.48432e-06
	3.29498	2.00619e-05 ± 1.55835e-06	8.47075e-06 ± 9.59165e-07
	3.49446	9.48877e-06 ± 1.03876e-06	3.94828e-06 ± 7.6951e-07
	3.77494	3.59832e-06 ± 4.83137e-07	2.02854e-06 ± 4.07465e-07
	4.20413	1.36378e-06 ± 3.0704e-07	3.07905e-07 ± 2.90855e-07
	4.79342	1.71882e-07 ± 1.16106e-07	-2.65859e-07 ± -9.89291e-08

Table A.10: Corrected yields for 60-92% and minimum bias at the mean of the p_T bin for all centrality classes.

Centrality	p_T GeV/c	Ed^3N/dp^3 (Deuterons)	Ed^3N/dp^3 (Anti-deuterons)
60-92%	1.10079	0.000323151 ± 1.69362e-05	0.000106425 ± 9.96842e-06
	1.30026	0.000205261 ± 8.17357e-06	8.65743e-05 ± 4.75587e-06
	1.49974	0.000129929 ± 4.73964e-06	5.9996e-05 ± 3.11463e-06
	1.69921	8.58012e-05 ± 3.24069e-06	4.24344e-05 ± 2.23669e-06
	1.89868	4.95704e-05 ± 2.1355e-06	2.54016e-05 ± 1.51495e-06
	2.09815	3.18946e-05 ± 1.54705e-06	1.42749e-05 ± 1.06637e-06
	2.29762	1.89242e-05 ± 1.19503e-06	8.82025e-06 ± 7.6912e-07
	2.49709	1.16835e-05 ± 8.1831e-07	5.4483e-06 ± 6.51508e-07
	2.69657	5.77184e-06 ± 5.67199e-07	3.47463e-06 ± 4.6253e-07
	2.89604	3.91108e-06 ± 5.47725e-07	1.96492e-06 ± 3.62196e-07
	3.09551	2.27428e-06 ± 3.67546e-07	7.83399e-07 ± 3.17454e-07
	3.29498	1.09415e-06 ± 2.93885e-07	2.45994e-07 ± 2.35707e-07
	3.49446	5.53787e-07 ± 2.3788e-07	4.5219e-07 ± 2.37327e-07
	3.77494	2.96131e-07 ± 1.28035e-07	2.37079e-07 ± 1.05413e-07
	4.20413	1.45019e-07 ± 6.97156e-08	1.31424e-07 ± 7.94803e-08
	4.79342	8.57167e-09 ± 2.47373e-08	2.68811e-08 ± 3.07347e-08
MB	1.10079	0.00281336 ± 6.27903e-05	0.000892088 ± 2.91351e-05
	1.30026	0.00218195 ± 3.72919e-05	0.000874457 ± 1.75403e-05
	1.49974	0.00183516 ± 2.90949e-05	0.000772753 ± 1.36712e-05
	1.69921	0.00145105 ± 2.1954e-05	0.000621596 ± 1.04954e-05
	1.89868	0.00110433 ± 1.60836e-05	0.000466946 ± 7.64652e-06
	2.09815	0.000809465 ± 1.16821e-05	0.000348637 ± 5.73346e-06
	2.29762	0.00056329 ± 8.1746e-06	0.000242848 ± 4.09948e-06
	2.49709	0.000380129 ± 5.71468e-06	0.000164933 ± 2.93454e-06
	2.69657	0.000259359 ± 4.13079e-06	0.000110829 ± 2.29543e-06
	2.89604	0.000165728 ± 2.94359e-06	7.23849e-05 ± 1.77368e-06
	3.09551	0.000101656 ± 1.96542e-06	4.66076e-05 ± 1.51255e-06
	3.29498	5.97951e-05 ± 1.37376e-06	2.67958e-05 ± 9.26261e-07
	3.49446	3.4998e-05 ± 1.02679e-06	1.52495e-05 ± 7.39235e-07
	3.77494	1.33747e-05 ± 4.5527e-07	6.14753e-06 ± 3.59641e-07
	4.20413	4.21918e-06 ± 2.61869e-07	1.32372e-06 ± 2.11469e-07
	4.79342	2.95287e-07 ± 1.14178e-07	1.04283e-07 ± 9.9585e-08

A.2.6 Systematic Error on Particle Ratio

Table A.11: Anti-deuterons/deuterons ratio with error at the mean of each p_T for 0-10% and 10-20% centrality classes.

Centrality	p_T GeV/c	$\bar{d}/d$ Ratio	Stat. Error	Sys. Error
0-10%	1.10086	0.314637	0.0140295	0.0580115
	1.30029	0.378888	0.00986824	0.0301687
	1.49971	0.390973	0.00853696	0.0368751
	1.69914	0.393062	0.00803929	0.0245342
	1.89857	0.405459	0.00792771	0.0251707
	2.09799	0.414931	0.00823368	0.0242047
	2.29742	0.419312	0.00870689	0.0444237
	2.49685	0.428327	0.00974798	0.0221942
	2.69628	0.427051	0.0111949	0.0199395
	2.8957	0.417022	0.0124411	0.0380543
	3.09513	0.432965	0.0163108	0.0410263
	3.29456	0.416304	0.018968	0.0476222
	3.49399	0.374737	0.0220481	0.0457405
	3.77288	0.399297	0.0308401	0.078991
	4.20045	0.375764	0.0585963	0.0966501
10-20%	1.10086	0.330713	0.0136746	0.110375
	1.30029	0.380802	0.00948435	0.02557
	1.49971	0.385418	0.00817511	0.0416297
	1.69914	0.407503	0.00816586	0.0534337
	1.89857	0.415452	0.0080815	0.0235779
	2.09799	0.413303	0.0080905	0.0189052
	2.29742	0.411858	0.00859032	0.0675064
	2.49685	0.416969	0.0094118	0.0452391
	2.69628	0.410132	0.0108445	0.0552121
	2.8957	0.406392	0.0126739	0.0389683
	3.09513	0.416989	0.0153278	0.123047
	3.29456	0.449688	0.0205392	0.0578157
	3.49399	0.429125	0.0269959	0.0879354
	3.77288	0.466347	0.0355545	0.0914293
	4.20045	0.339676	0.0583303	0.156323

Table A.12: Anti-deuterons/deuterons ratio with error at the mean of each p_T for 20-40% and 40-60% centrality classes.

Centrality	p_T GeV/c	$\bar{d}/d$ Ratio	Stat. Error	Sys. Error
20-40%	1.10086	0.357474	0.0117344	0.0401983
	1.30029	0.395143	0.0085847	0.030747
	1.49971	0.413288	0.00795722	0.0278831
	1.69914	0.426572	0.00779865	0.0177467
	1.89857	0.428301	0.00767714	0.0190014
	2.09799	0.448112	0.00820044	0.0208907
	2.29742	0.456193	0.00887601	0.0195483
	2.49685	0.460205	0.00983723	0.0238447
	2.69628	0.444759	0.0109128	0.0218314
	2.8957	0.447758	0.0134935	0.0299745
	3.09513	0.434188	0.0151499	0.0455643
	3.29456	0.451754	0.0204192	0.0473334
	3.49399	0.488886	0.0298735	0.0820249
	3.77288	0.458903	0.0322717	0.0534321
	4.20045	0.406158	0.0711671	0.224834
40-60%	1.10086	0.347184	0.0135772	0.040362
	1.30029	0.418713	0.01099	0.0204709
	1.49971	0.455291	0.0105479	0.0251052
	1.69914	0.447844	0.0102922	0.0308199
	1.89857	0.457189	0.010711	0.0212188
	2.09799	0.471001	0.0118514	0.0210407
	2.29742	0.485623	0.0137087	0.0605692
	2.49685	0.460102	0.0150181	0.0425532
	2.69628	0.458814	0.0186588	0.0201612
	2.8957	0.472723	0.0251302	0.0242521
	3.09513	0.442058	0.031482	0.159776
	3.29456	0.434525	0.039195	0.0597954
	3.49399	0.476848	0.0640104	0.162938
	3.77288	0.462835	0.0755205	0.220557
	4.20045	0.194519	0.0909864	0.406119

Table A.13: Anti-deuterons/deuterons ratio with error at the mean of each p_T for 60-92% and minimum bias centrality classes.

Centrality	p_T GeV/c	$\bar{d}/d$ Ratio	Stat. Error	Sys. Error
60-92%	1.10086	0.363297	0.0224464	0.0957922
	1.30029	0.433993	0.0188948	0.0458208
	1.49971	0.450703	0.018453	0.0306138
	1.69914	0.478035	0.0202467	0.0382632
	1.89857	0.495993	0.0238107	0.0370386
	2.09799	0.466961	0.0269089	0.0452501
	2.29742	0.468326	0.0336419	0.0409683
	2.49685	0.453253	0.0391922	0.0697907
	2.69628	0.436243	0.048354	0.298031
	2.8957	0.555101	0.0765685	0.210106
	3.09513	0.324595	0.0746756	0.209475
	3.29456	0.553152	0.206305	0.759901
	3.49399	1.57884	0.714145	2.16894
	3.77288	0.704191	0.261561	1.04902
	4.20045	0.837135	0.582711	2.40229
MB	1.10086	0.337416	0.00846143	0.04459
	1.30029	0.392525	0.00717827	0.0230866
	1.49971	0.407321	0.00670676	0.0314757
	1.69914	0.416924	0.00654897	0.0278536
	1.89857	0.423804	0.00642859	0.0177648
	2.09799	0.43253	0.0065408	0.0186129
	2.29742	0.436983	0.00673215	0.0225506
	2.49685	0.440339	0.00711488	0.0232995
	2.69628	0.431589	0.00760781	0.020002
	2.8957	0.431086	0.00848552	0.0238658
	3.09513	0.43213	0.00980667	0.0560875
	3.29456	0.439621	0.0117975	0.026817
	3.49399	0.43659	0.0153176	0.0250906
	3.77288	0.448457	0.0188483	0.0349295
	4.20045	0.348474	0.0328526	0.167386

APPENDIX B

FIDUCIAL CUT STUDY

In this Appendix, we include the comparison between the detectors active area or Fiducial Cuts (FC), for both data and simulation.

The first detector we checked was the drift chamber. In Figure B.1 we compared the phi vs. zed for the DC. The right plots show the distribution for phi vs. zed for real before (top left) and after cuts (bottom left). The right plots show the same distribution for the simulated data [a].

Another way of checking FC for DC is to plot the distribution of particles as alpha vs. board. Figure B.2 shows this distribution for both data (left) and MC (right). We also plotted ϕ vs. α for the same DC points. Figure B.3 shows the distribution for real data and figure B.4 shows the distribution for MC.

The next detector in which we performed the FC study was the TOF.W. For this detector, we plotted the $TOF.W_{\phi}$ vs. $TOF.W_{z}$ distribution. Figure B.5 show the distribution for real data (left) and MC (right). We also plotted the tracking residual for dz and dphi for both data (Figures B.6, B.8) and MC (Figures B.7, B.9)

Finally, the last detector we did FC studies on was the PC3. We needed to match dead areas on PC3 because it is part of our matching cut requirements. Figure B.10 shows the distribution for real data(left) and MC (right).

[a] These plots, and all the following figures, correspond to dead areas withing the two sectors of TOF.W

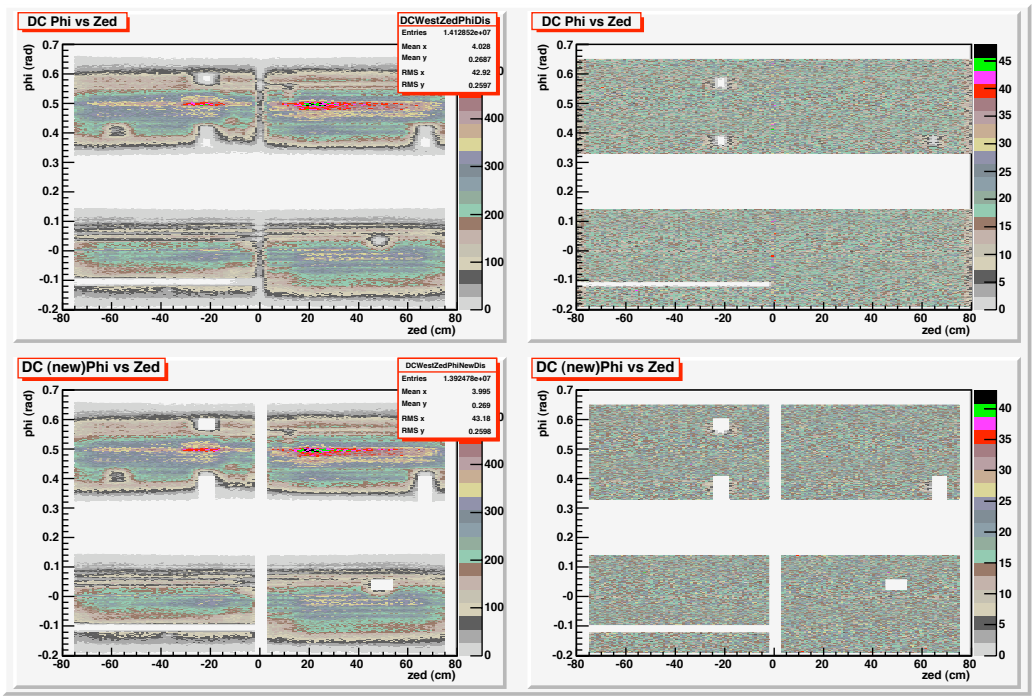

Figure B.1: Drift chamber ϕ vs zed within TOF.W active area.

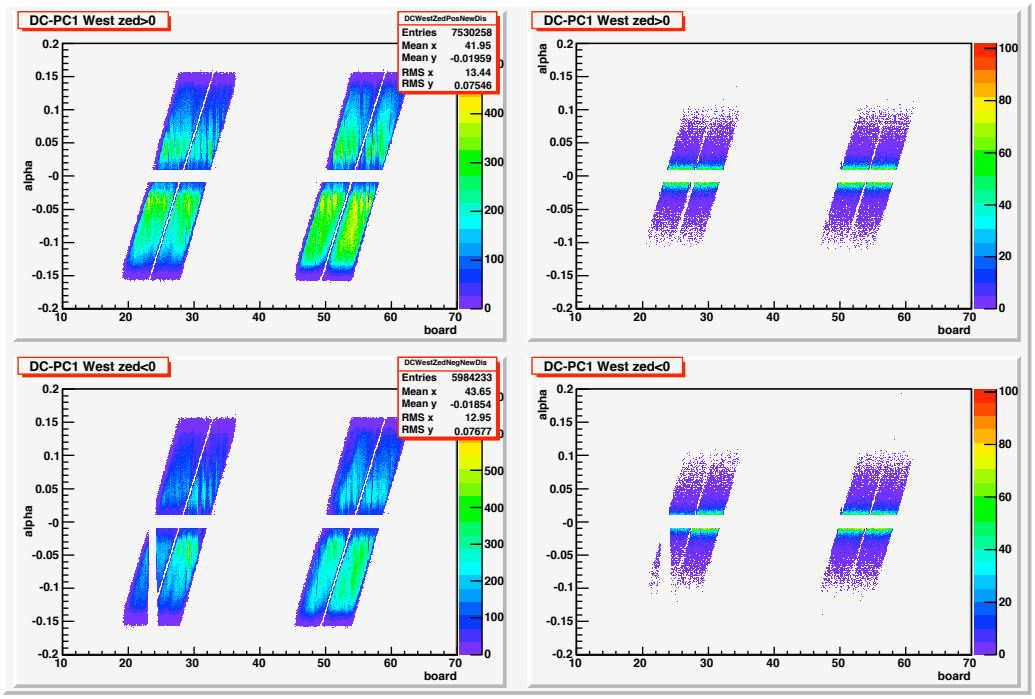

Figure B.2: Drift chamber α vs board within TOF.W acceptance for Run 7 data (left) and simulation (right).

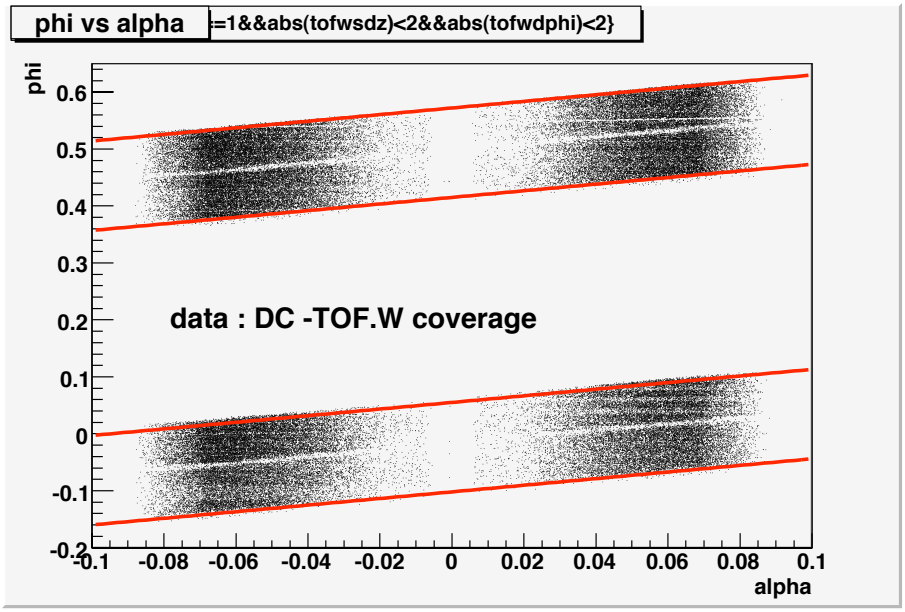

Figure B.3: Drift chamber ϕ vs α within TOF.W acceptance for Run 7 data.

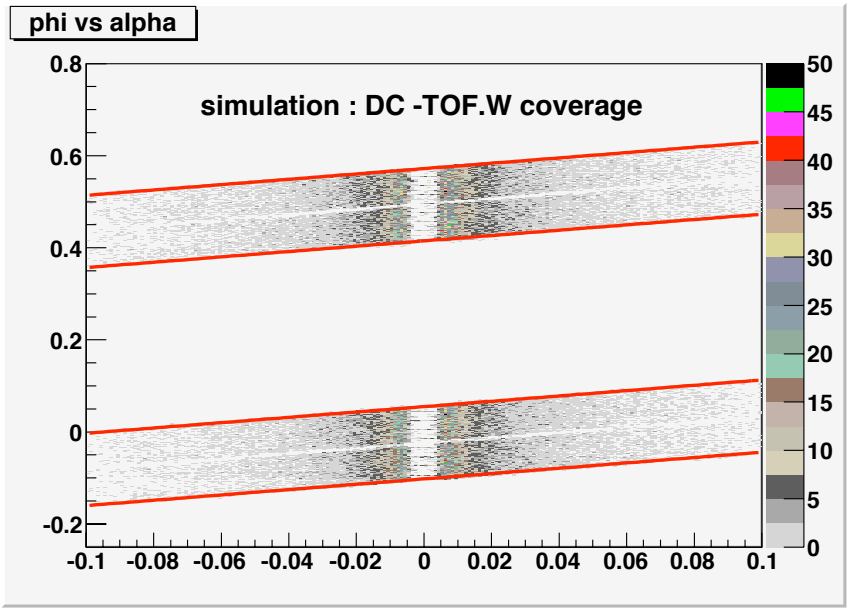

Figure B.4: Drift chamber ϕ vs α within TOF.W acceptance for simulations.

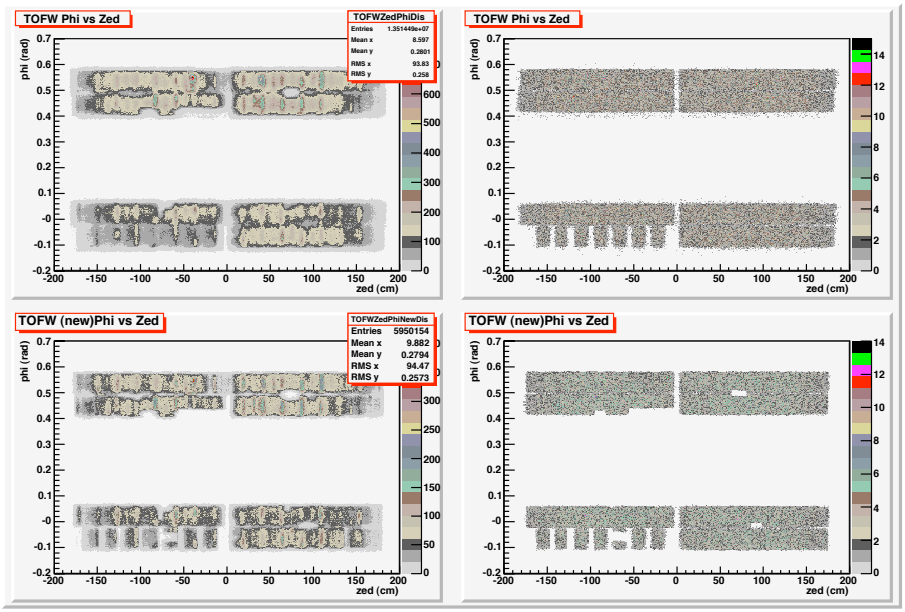

Figure B.5: TOF.W ϕ vs zed within TOF.W acceptance for Run 7 data (left) and simulation(right).

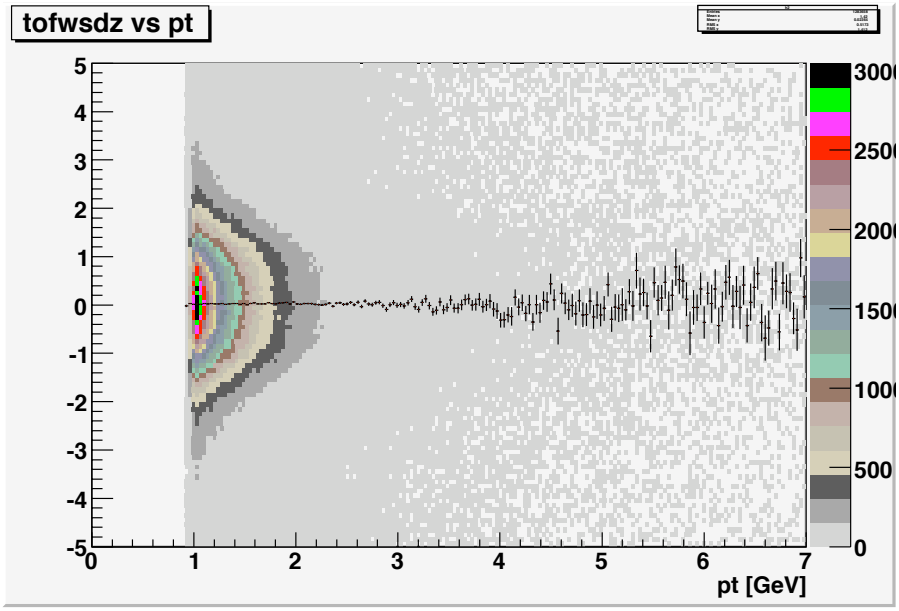

Figure B.6: TOF.W signalized zed tracking residuals for Run 7 data.

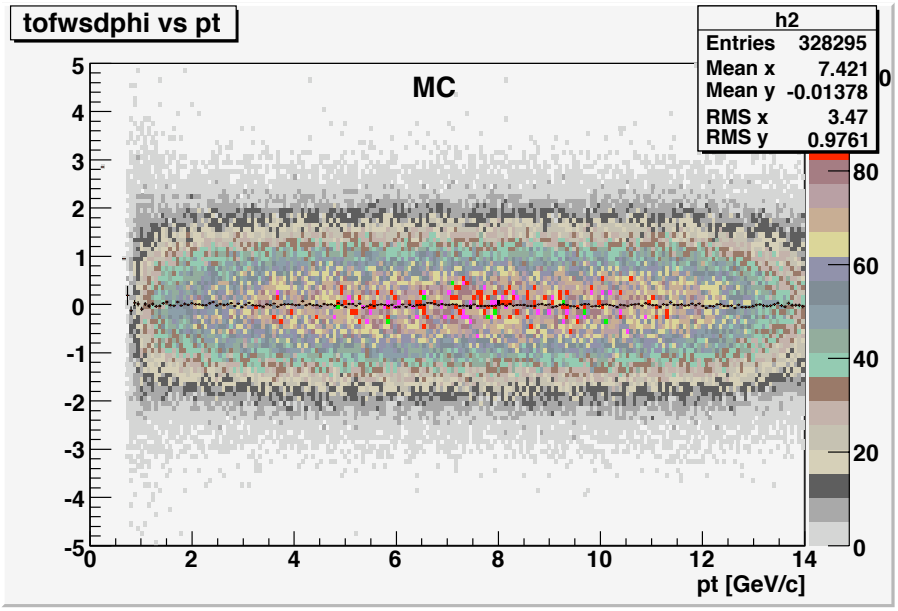

Figure B.7: TOF.W signalized zed tracking residuals for simulations.

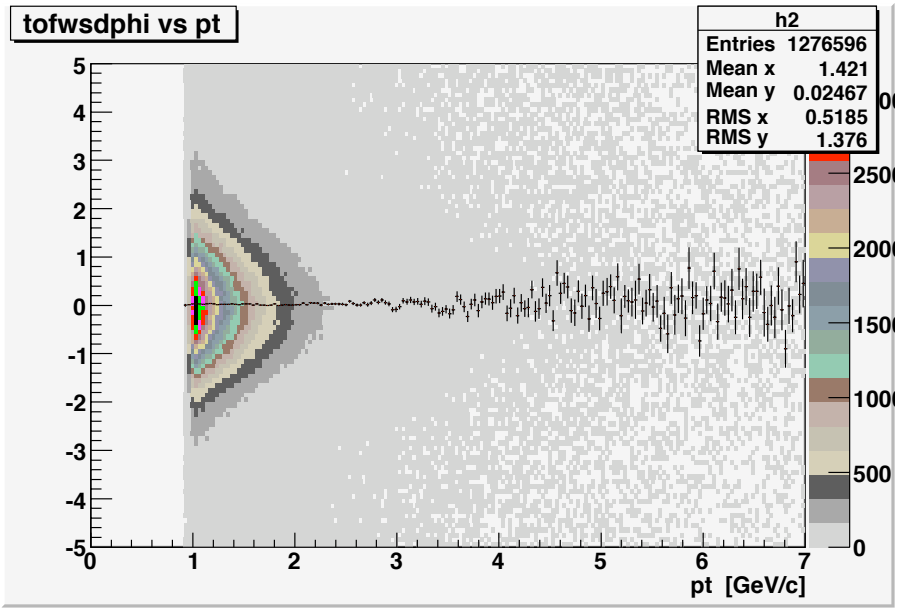

Figure B.8: TOF.W signalized ϕ tracking residuals for Run 7 data.

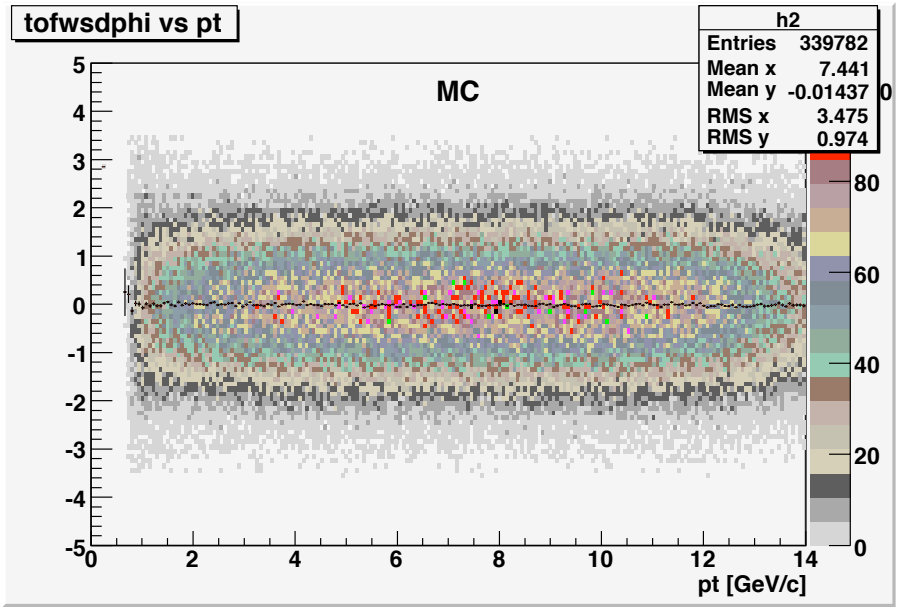

Figure B.9: TOF.W signalized ϕ tracking residuals for simulations.

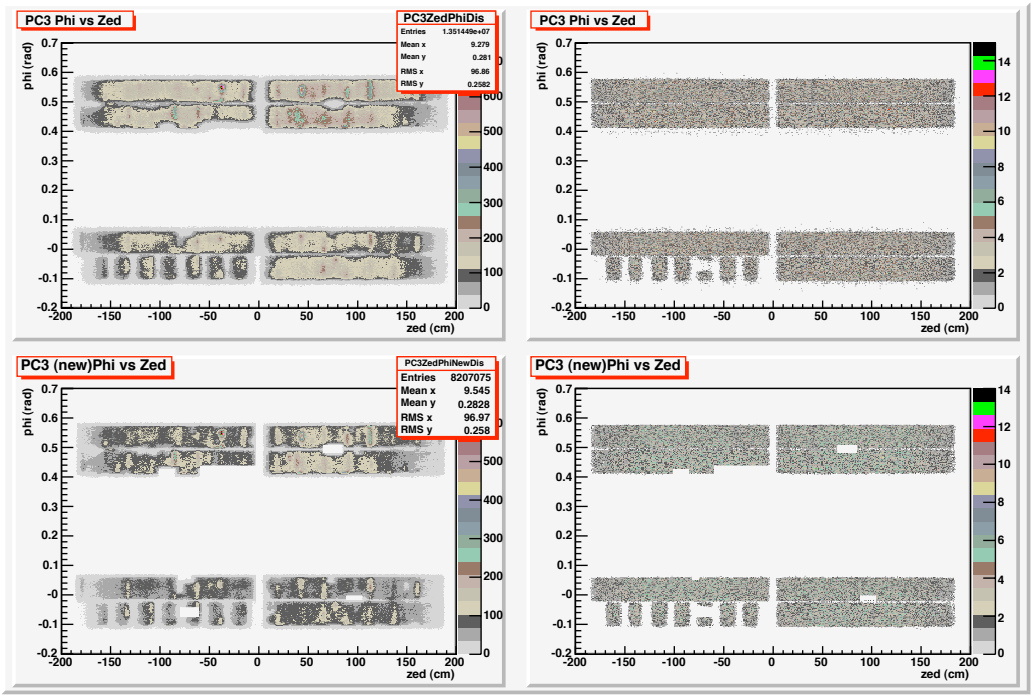

Figure B.10: PC3 ϕ vs. zed within TOF.W acceptance for Run 7 data (right) and simulation(left).

APPENDIX C

SURVIVAL PROBABILITY APPENDIX

C.1 Parameterization of the Cross Section

C.1.1 First Approach

The recipe of A.A.Moiseev and J.F. Ormes in [59], for calculating inelastic anti-helium cross section on nuclei, can be modified to give anti-deuteron cross sections. The authors in this paper used their calculations to estimate the probability to observe anti-helium among cosmic rays. The Helium cross sections are parameterized as:

$$\sigma_{He,A} = (2 \cdot \sigma_{p,A}^{3/2} + 2 \cdot \sigma_{n,A}^{3/2})^{2/3} \cdot K_a(A) \tag{C.1}$$

where $\sigma_{p,A}$, and $\sigma_{n,A}$ are the inelastic cross sections for protons and neutrons on nuclei, respectively, and A is the target atomic mass number.(It is not easy to see the idea behind this parameterization).

In the case of deuterons, we will modified equation C.1 to:

$$\sigma_{d,A} = (\sigma_{p,A}^{3/2} + \sigma_{n,A}^{3/2})^{2/3} \cdot K_d(A) \tag{C.2}$$

Going back to the paper, the following parameterizations of $\sigma_{p,A}$, and $\sigma_{n,A}$ are used by the authors:

$$
\begin{aligned}
(\sigma)_{p,A}(E) &= 45 \cdot A^{0.7} \cdot [1 + 0.016 \sin 5.3 - 2.63 lnA] \\
&\quad \cdot [1 - 0.62 exp(-5E) \sin 1.58]
\end{aligned} \tag{C.3}
$$

and

$$
\sigma_{n,A} = (43.2 \pm 2.3) \cdot A^{0.719 \pm 0.012} \tag{C.4}
$$

In the proton case, E is the kinetic energy of the proton in GeV and the cross sections are given in mb. For the proton case $45A^{0.7}$ can be used above 0.8 GeV.

Based on experimental data, they find:

$$
K_a(A) = 1.2 \cdot [ln(A+2)]^{-0.5} \tag{C.5}
$$

Using available data on deuterons induced interactions, we find a similar expression for $K_d(A)$, namely:

$$
K_d(A) = 1.6 \cdot [ln(A+4)]^{-0.5} \tag{C.6}
$$

In the paper it is assumed that the anti-helium cross sections can be written in the same way as in equation C.1, i.e.

$$
\sigma_{\bar{H}e,A} = (2 \cdot \sigma_{\bar{p},A}^{3/2} + 2 \cdot \sigma_{\bar{n},A}^{3/2})^{2/3} \cdot K_\alpha(A) \tag{C.7}
$$

where it is assumed that the factor $K_\alpha(A)$ is the same as in equation C.1. (This assumption is also questionable, since this factor contains most of the mass dependence.)

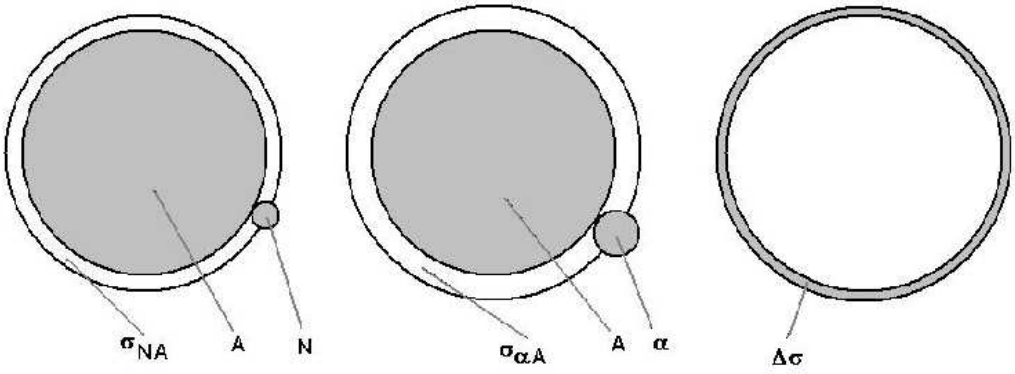

Figure C.1: Geometry motivation for the second approach.

In the deuteron case, we will similarly be able to write the anti-deuteron equation as:

$$\sigma_{\bar{d},A} = (\sigma_{\bar{p},A}^{3/2} + \sigma_{\bar{n},A}^{3/2})^{2/3} \cdot K_d(A) \tag{C.8}$$

The following parameterization of $\sigma_{\bar{p},A}$ and $\sigma_{\bar{n},A}$ are used by the authors:

$$\begin{aligned}(\sigma)_{\bar{p},A}(E) &= A^{2/3} \cdot [48.2 + 19 \cdot (E - 0.02)^{-0.55} - 0.106 \cdot A^{0.927} \cdot E^{-1.2} \\ &\quad + 0.059A^{0.927} + 0.00042A^{1.854} \cdot E^{-1.5}]\end{aligned} \tag{C.9}$$

and

$$\sigma_{\bar{n},A} = A^{2/3} \cdot (51 + 16 \cdot E^{-0.4}) \tag{C.10}$$

C.1.2 A New Approach

The idea behind equation C.1 is however not transparent. There is no real picture behind this parameterization. Furthermore, since the factor $K_\alpha(A)$ contains most of the mass dependence (and even has to compensate for the wrong mass dependence introduced in equation C.1), it is not at all evident that this factor will be the same in the anti-helium (anti-deuteron) case.

A new approach as in the analysis done for [1] was followed. This new approach will start with:

$$\sigma_{He,A} = \sigma_{N,A} + \sigma_{He,A} \tag{C.11}$$

where

$$\sigma_{N,A} = \frac{\sigma_{p,A} + \sigma_{n,A}}{2} \tag{C.12}$$

Now, from figure C.1, we obtain

$$\sigma_{He,A} = [\sqrt{\sigma_{N,A}} + \Delta_{He}(A)]^2 \tag{C.13}$$

from which we find

$$\Delta_{He}(A) = \sqrt{\sigma_{He,A}} - \sqrt{\sigma_{N,A}} \tag{C.14}$$

From experimental data we find $\Delta He = 6.03 \pm 0.23$, independent of A, within the experimental errors.

In the case of deuterons, we obtain similarly

$$\sigma_{d,A} = [\sqrt{\sigma_{N,A}} + \Delta_d(A)]^2 \tag{C.15}$$

and

$$\Delta_d(A) = \sqrt{\sigma_{d,A}} - \sqrt{\sigma_{N,A}} \tag{C.16}$$

Again, we use experimental [60, 61] data to find $\Delta d = 3.51|pm0.25$ independent of A. For $\sigma_{\bar{He},A}$ and $\sigma_{\bar{d},A}$ we use the idea of A.A.Moiseev and J.F.Ormes and write:

$$\sigma_{\bar{He},A} = [\sqrt{\sigma_{N,A}} + \Delta_{He}(A)]^2 \tag{C.17}$$

and

$$\sigma_{\bar{d},A} = [\sqrt{\sigma_{\bar{N},A}} + \Delta_d(A)]^2 \tag{C.18}$$

where

$$\sigma_{\bar{N},A} = \frac{\sigma_{\bar{p},A} + \sigma_{\bar{n},A}}{2} \tag{C.19}$$

In this case, it is much more plausible to use the same terms of Δ_{He} and Δ_d, since these terms only reflect the difference in size between a Helium-nucleus (deuterons) and a proton, and this difference is size should be the same if anti-nuclei and anti-protons are compared. Furthermore they show no mass dependence. Care should be taken when the parameterization are used at the lowest energies. Some cross section calculation for projectile are tabulated in Table C.3

C.2 Media an Material in PISA for Run 7

Table C.1: Tracking media transverse by geantinos in the west arm with corresponding path lengths.

Detector	Name	A	ρ[g/cm^3]	Length [cm]
General	Air	14.61	0.001	132.502
	Silicon	28.09	2.33	0.014
	AIRLOWF	14.61	0.001	18.081
	AIRF	14.61	0.001	34.205
	MPCFrame	18.14	1.7	0.332
	MPCMylarPln	12.88	1.39	0.026
	AluminumFrame	26.98	2.7	0.054
	Be+Field	9.01	1.848	0.103
DC	DC window	12.872	1.39	0.02
	Gas in DC1	21.855	0.001	32.488
	ACT gas In DC1	21.855	0.001	12.144
PC1	CarbonF/Epoxy	18.14	1.7	0.028
	S2Glass/Epoxy	18.14	1.7	0.026
	Hex Cell Core	12.01	0.024	5.139
	Epoxy Glue	18.14	1.7	0.02
	Pad Chamber Gas	21.855	0.001	0.607
	Pad Cathode Board	18.866	1.82	0.026
	Gr. Cathode Board.	18.866	1.82	0.026
	Mother Board	14.827	0.093	1.014
RICH	CO2	14.911	0.002	149.005
	RICH mir .Substr.	11.856	0.29	1.176
PC2	CarbonFib/Epoxy	18.14	1.7	0.055
	S2Glass/Epoxy	18.14	1.7	0.142
	Hex Cell Core	12.01	0.024	4.464
	Pad Cathode Board	19.593	1.93	0.037
	Gr. Cathode Board	18.866	1.82	0.058
	Mother Board	14.872	0.093	0.549
	PC2 Chamber Gas	21.855	0.001	0.872

Table C.2: Tracking media transverse by geantinos in the west arm with corresponding path lengths.

Detector	Name	A	ρ[g/cm^3]	Length [cm]
ACC	Air	14.61	0.001	62.657
	Air ACC	14.61	0.001	28.13
	Aluminum	26.98	2.7	0.3588
	g10	18.631	1.7	0.42
	permaloy	58.089	8.58	0.26
	mylar	12.872	1.39	0.0212
	Goretex	17.321	2.2	0.1056
	aerogel	21.652	0.05	12.8338
TOF.W	AlWall	26.98	2.7	0.334
	Honeycomb	9.065	0.024	0.95
	CopperStrips	65.54	8.96	0.05
	PCB	18.14	1.7	0.15
	Mylar	12.877	1.4	0.025
	CarbonTape	12.01	2.265	0.09
	OuterGlass	23.225	2.4	0.11
	ActMRPCgas	16.893	0.004	0.023

Table C.3: Deuterons induced cross section with nuclei.

Projectile	σ[mb]	Reference
^2d	134	[60]
^4He	204	[61]
^{12}C	401	[60, 61]
^{181}Ta	1940	[61]

APPENDIX D

NUMERICAL AND VOCABULARY SUPPLEMENT

D.1 Relativistic Kinematic and Variables

In this section we introduce some of the kinematic variables used in the thesis. Relativistic Heavy-Ion Collision deals with relativistic particles and systems. It is useful to describe kinematic variables with Lorentz invariant variables or variables which have simple Lorentz transformation properties. To defined these variables, we need to defined our coordinates. We will take the z-axis as the beam line.

- **Center of energy** aka $\sqrt{s}$, this is the Lorentz invariant quantity:

$$s = (p_1 + p_2)_\mu (p_1 + p_2)^\mu \tag{D.1}$$

  For nuclei with energy E_i, and 3-momentum p_i, it reduces to:

$$\sqrt{s} = \sqrt{m_1^2 + 2E_1E_2 - 2p_1.p_2 + m_2^2} \tag{D.2}$$

  For instance, for this thesis work, the center-of-mass energy per nucleon is $\sqrt{s_{NN}}$ = 200 GeV.

- **Transverse momentum** p_T**:** this is simply the projection of a particle's momentum

perpendicular to the collision axis: z (see Figure)

$$p_T = (p \sin\theta) \tag{D.3}$$

where θ is the polar angle along the $z - axis$. A common variable derived from this is transverse energy (or mass) m_T

$$m_T \equiv \sqrt{p_T^2 + m^2} \tag{D.4}$$

- **Rapidity y:** this defines the longitudinal motion scale for a particle of mass m_o moving along the $z - axis$ (see Figure)

$$Y = \frac{1}{2} \log \frac{E + p_z}{E - p_z} \tag{D.5}$$

Since there is cylindrical symmetry around the collision axis, this allows us to describe the 4-momentum of a particle in terms of its transverse momentum p_T, rapidity y and the transverse energy m_T as:

$$p^\mu = (m_T \cosh y, p_T \cos\phi_o, m_T \sinh y \tag{D.6}$$

- **Pseudo-rapidity η:** derived from rapidity (Eq. D.5), this variable is used when the

particle in question is unidentified *i.e.* m_o is not know:

$$\eta = -log(\tan\frac{\theta}{2}) \tag{D.7}$$

where θ is the angle w.r.t. the beam axis. η is often used to describe geometrical acceptance of detectors

- **Invariant Yield:** the invariant differential cross section of a particle is the probability of obtaining d^3N particles in the phase space volume dp^3/E in a given number of events N_{events}:

$$\frac{1}{N_{events}}E\frac{d^3N}{dp^3} = \frac{d^3N}{N_{events}p_T dp_T dy} \tag{D.8}$$

In cylindrical coordinates dp^3 = $dp_x dp_y dp_z$, this reduces to $p_T dp_T d\phi m_t \cosh y dy$. Due to azimuthal symmetry we get a factor of $1/2\pi$, resulting in the form:

$$\frac{1}{N_{events}}E\frac{d^2N}{dp^2} = \frac{d^2N}{2\pi N_{events}p_T dp_T dy} \tag{D.9}$$

using $dN/p_T dp_T = dN/m_T dm_T$, we get our final form:

$$\frac{1}{N_{events}}E\frac{d^2N}{dp^2} = \frac{d^2N}{2\pi N_{events}m_T dm_T dy} \tag{D.10}$$

REFERENCES

[1] S. S. Adler et al. Identified Charged Particle Spectra and Yields in $Au+Au$ Collisions at $\sqrt{s_{NN}} = 200\ GeV$. *Physical Review C (Nuclear Physics)*, 69(3):034909, 2004.

[2] Edward V. Shuryak. Quantum chromodynamics and the theory of superdense matter. *Physics Reports*, 61:71, 1980.

[3] F. Karsch, E. Laermann, A. Peikert, C. Schmidt, and S. Stickan. Flavor and quark mass dependence of QCD thermodynamics. *Nucl. Phys. Proc. Suppl.*, 94:411–414, 2001.

[4] F. Karsch. Lect. Notes Phys. 583 (2002). *Arxiv preprint hep-lat/0106019. Full Text via CrossRef*, page 209, 2002.

[5] Peter Jacobs et al. Phases of QCD: Summary of the Rutgers long range plan town meeting. *arXiv:0705.1930*, 2007.

[6] Krishna Rajagopal. Traversing the QCD phase transition: Quenching out of equilibrium vs. slowing out of equilibrium vs. bubbling out of equilibrium. *Nucl. Phys.*, A680:211–220, 2000.

[7] K. Adcox et al. Formation of dense partonic matter in relativistic nucleus nucleus collisions at RHIC: Experimental evaluation by the PHENIX collaboration. *Nucl. Phys.*, A757:184–283, 2005.

[8] J. D. Bjorken. Highly Relativistic Nucleus-Nucleus Collisions: The Central Rapidity Region. *Phys. Rev.*, D27:140–151, 1983.

[9] Peter F. Kolb and Ralf Rapp. Transverse flow and hadro-chemistry in Au + Au collisions at s(NN)**(1/2) = 200-GeV. *Phys. Rev.*, C67:044903, 2003.

[10] Francesco Becattini. A Thermodynamical Approach to Hadron Production in e+ e-Collisions. *Z. Phys.*, C69:485–492, 1996.

[11] Xin-Nian Wang and Miklos Gyulassy. Gluon shadowing and jet quenching in A+A collisions at $\sqrt{s_{NN}} = 200GeV$. *Phys. Rev. Lett.*, 68(10):1480–1483, Mar 1992.

[12] M. Gyulassy and M. Plümer. Jet quenching in dense matter. *Physics Letters B*, 243(4):432–438, 1990.

[13] R. Baier, Yu. L. Dokshitzer, S. PeignÈ, and D. Schiff. Induced gluon radiation in a QCD medium. *Physics Letters B*, 345(3):277–286, 1995.

[14] Stephen Scott Adler et al. High transverse momentum eta meson production in p + p, d + Au and Au + Au collisions at s(NN)**(1/2) = 200-GeV. *Phys. Rev.*, C75:024909, 2007.

[15] J. Adams et al. Evidence from $d + Au$ Measurements for Final-State Suppression of High-pT Hadrons in $Au + Au$ Collisions at RHIC. *Phys. Rev. Lett.*, 91(7):072304, Aug 2003.

[16] S. S. Adler et al. Absence of Suppression in Particle Production at Large Transverse Momentum in $\sqrt{s_{NN}} = 200\ GeV$ $d + Au$ Collisions. *Phys. Rev. Lett.*, 91(7):072303, Aug 2003.

[17] T. Matsui. J/Ψ Suppression by plasma formation. *Zeitschrift für Physik C Particles and Fields*, 38(1):245–249, 1988.

[18] T. Matsui and H. Satz. J/Ψ suppression by the quark-gluon plasma formation, Phys. *Lett. B*, 178(416), 1986.

[19] Dirk H. Rischke. Hydrodynamics and collective behaviour in relativistic nuclear collisions. *Nucl. Phys.*, A610:88c–101c, 1996.

[20] Jean-Yves Ollitrault. Anisotropy as a Signature of Transverse Collective Flow. *Phys. Rev.*, D46:229–245, 1992.

[21] Arthur M. Poskanzer and S. A. Voloshin. Methods for Analyzing Anisotropic Flow in Relativistic Nuclear Collisions. *Phys. Rev.*, C58:1671–1678, 1998.

[22] A. Adare et al. Scaling properties of azimuthal anisotropy in Au + Au and Cu + Cu collisions at s(NN)**(1/2) = 200-GeV. *Phys. Rev. Lett.*, 98:162301, 2007.

[23] R. Hanbury-Brown and R. Q. Twiss. *Phil. Mag.*, 45:633, 1954.

[24] H. Sorge, J. L. Nagle, and B. S. Kumar. Scaling of deuteron production in ultrarelativistic nucleus-nucleus collisions. *Physics Letters B*, 355(1-2):27–31, 1995.

[25] L. Csernai and J.I. Kapusta. Entropy and Pluster Production in Nuclear Collisions. *Physics Reports*, 131(4):223–318, 1986.

[26] A. Z. Mekjian. Explosive Nucleosynthesis, Equilibrium Thermodynamics, and Relativistic Heavy-Ion Collisions. *Phys. Rev. C*, 17(3):1051–1070, Mar 1978.

[27] Ruediger Scheibl and Ulrich Heinz. Coalescence and Flow in Ultra-relativistic Heavy Ion Collisions. *Physical Review C*, 59:1585, 1999.

[28] S. T. Butler and C. A. Pearson. Deuterons from High-Energy Proton Bombardment of Matter. *Phys. Rev.*, 129(2):836–842, Jan 1963.

[29] K. Adcox et al. Single Identified Hadron Spectra from $\sqrt{s_{NN}} = 130\ GeV$ Au + Au Collisions. *Physical Review C (Nuclear Physics)*, 69(2):024904, 2004.

[30] S. S. Adler et al. Production of Phi Mesons at Midrapidity in $\sqrt{s_{NN}} = 200\ GeV$ Au + Au Collisions at Relativistic Energies. *Physical Review C (Nuclear Physics)*, 72(1):014903, 2005.

[31] M. Harrison, T. Ludlam, and S. Ozaki. RHIC Project Overview. *Nuclear Instruments and Methods in Physics Research Section A: Accelerators, Spectrometers, Detectors and Associated Equipment*, 499(2-3):235–244, 2003.

[32] H. Hahn et al. The RHIC Design Overview. *Nuclear Instruments and Methods in Physics Research Section A: Accelerators, Spectrometers, Detectors and Associated Equipment*, 499(2-3):245–263, 2003.

[33] K. Adcox et al. PHENIX Detector Overview. *Nuclear Instruments and Methods in Physics Research Section A: Accelerators, Spectrometers, Detectors and Associated Equipment*, 499(2-3):469–479, 2003.

[34] K. Adcox et al. PHENIX Central Arm Tracking Detectors. *Nuclear Instruments and Methods in Physics Research Section A: Accelerators, Spectrometers, Detectors and Associated Equipment*, 499(2-3):489–507, 2003.

[35] L. Aphecetche et al. PHENIX Calorimeter. *Nuclear Instruments and Methods in Physics Research Section A: Accelerators, Spectrometers, Detectors and Associated Equipment*, 499(2-3):521–536, 2003.

[36] M. Aizawa et al. PHENIX Central Arm Particle ID Detectors. *Nuclear Instruments and Methods in Physics Research Section A: Accelerators, Spectrometers, Detectors and Associated Equipment*, 499(2-3):508–520, 2003.

[37] M. Allen et al. PHENIX Inner Detectors. *Nuclear Instruments and Methods in Physics Research Section A: Accelerators, Spectrometers, Detectors and Associated Equipment*, 499(2-3):549–559, 2003.

[38] S. H. Aronson et al. PHENIX Magnet System. *Nuclear Instruments and Methods in Physics Research Section A: Accelerators, Spectrometers, Detectors and Associated Equipment*, 499(2-3):480–488, 2003.

[39] H. Akikawa et al. PHENIX Muon Arms. *Nuclear Instruments and Methods in Physics Research Section A: Accelerators, Spectrometers, Detectors and Associated Equipment*, 499(2-3):537–548, 2003.

[40] S. S. Adler et al. PHENIX on-line and off-line Computing. *Nuclear Instruments and Methods in Physics Research Section A: Accelerators, Spectrometers, Detectors and Associated Equipment*, 499(2-3):593–602, 2003.

[41] S. S. Adler et al. PHENIX on-line Systems. *Nuclear Instruments and Methods in Physics Research Section A: Accelerators, Spectrometers, Detectors and Associated Equipment*, 499(2-3):560–592, 2003.

[42] C. Adler et al. The RHIC Zero-Degree Calorimeters. *Nuclear Instruments and Methods in Physics Research Section A: Accelerators, Spectrometers, Detectors and Associated Equipment*, 499(2-3):433–436, 2003.

[43] X.N. Wang and M. Gyulassy. Multi-Particle Production at High Energy Heavy-Ion Collisions. *Phys Rev D*, 44:3501–3505, 1991.

[44] R. J. Glauber and G. Matthiae. High-Energy Scattering of Protons by Nuclei. *Nuclear Physics B*, 21(2):135–157, 1970.

[45] J. T. Mitchell et al. Event Reconstruction in the PHENIX Central Arm Spectrometers. *Nuclear Instruments and Methods in Physics Research Section A: Accelerators, Spectrometers, Detectors and Associated Equipment*, 482(1-2):491–512, 2002.

[46] Geant 3.21, cern program library.

[47] K. Adcox et al. Centrality Dependence of $\pi +/-$, $k +/-$, p, and p Production from $\sqrt{s_{NN}} = 130\ GeV$ Au + Au Collisions at RHIC. *Phys. Rev. Lett.*, 88(24):242301, May 2002.

[48] S. S. Adler et al. Deuteron and Antideuteron Production in $Au + Au$ Collisions at $\sqrt{s_{NN}} = 200\ GeV$. *Physical Review Letters*, 94(12):122302, 2005.

[49] C. Adler et al. d 3He Production in $\sqrt{s_{NN}} = 130\ GeV\ Au + Au$ Collisions. *Phys. Rev. Lett.*, 87(26):262301, Dec 2001.

[50] Ekkard Schnedermann, Josef Sollfrank, and Ulrich Heinz. Thermal Phenomenology of Hadrons from 200A GeV S+S Collisions. *Phys. Rev. C*, 48(5):2462–2475, Nov 1993.

[51] S. Wang et al. Light Fragment Production and Power Law Behavior in $Au + Au$ Collisions. *Phys. Rev. Lett.*, 74(14):2646–2649, Apr 1995.

[52] S. Albergo et al. Light Nuclei Production in Heavy-Ion Collisions at Relativistic Energies. *Phys. Rev. C*, 65(3):034907, Mar 2002.

[53] I. G. Bearden et al. Antideuteron Production in $158\ A\ GeV/c\ Pb + Pb$ Collisions. *Phys. Rev. Lett.*, 85(13):2681–2684, Sep 2000.

[54] I. G. Bearden et al. Antideuteron production in $158 agev/c\ pb + pb$ collisions. *Phys. Rev. Lett.*, 85(13):2681–2684, Sep 2000.

[55] T. Anticic et al. Energy and Centrality Dependence of Deuteron and Proton Production in $Pb + Pb$ Collisions at Relativistic Energies. *Physical Review C (Nuclear Physics)*, 69(2):024902, 2004.

[56] K. Adcox et al. Transverse-Mass Dependence of Two-Pion Correlations in $Au + Au$ Collisions at $\sqrt{s_{NN}} = 130\ GeV$. *Phys. Rev. Lett.*, 88(19):192302, Apr 2002.

[57] C. Adler et al. Pion Interferometry of $\sqrt{s_{NN}} = 130\ GeV\ Au + Au$ Collisions at RHIC. *Phys. Rev. Lett.*, 87(8):082301, Aug 2001.

[58] S. S. Adler et al. Bose-Einstein Correlations of Charged Pion Pairs in $Au + Au$ Collisions at $\sqrt{s_{NN}} = 200\ GeV$. *Phys. Rev. Lett.*, 93(15):152302, Oct 2004.

[59] AA Moiseev and JF Ormes. Inelastic Cross Section for Anti-Helium on Nuclei: an Empirical Formula for use in the Experiments to Search for Cosmic Antimatter. *Astroparticle Physics*, 6(3-4):379–386, 1997.

[60] J. Jaros et al. Nucleus-Nucleus Total Cross Sections for Light Nuclei at 1.55 and 2.89 GeV/c per Nucleon. *Phys. Rev. C*, 18(5):2273–2292, Nov 1978.

[61] E.O. Abdurakhmanov et al. Interaction Cross Sections and Negative Pion Multiplicities in Nucleus-Nucleus Collisions at 4.2 GeV/c per Nucleon. *Z. Phys C*, 5(1):1, 1980.